BAM
Bundesanstalt für
Materialforschung
und -prüfung

Dissertation

Solomija Lebid

Störungen in der Charakteristik von Faser-Bragg-Gitter-Sensoren durch lokale thermische und mechanische Einflüsse

BAM-Dissertationsreihe • Band 2

Dipl.-Ing. Solomija Lebid

Störungen in der Charakteristik von Faser-Bragg-Gitter-Sensoren durch lokale thermische und mechanische Einflüsse

BAM-Dissertationsreihe · Band 2
Berlin 2004

Impressum

Störungen in der Charakteristik von Faser-Bragg-Gitter Sensoren durch lokale thermische und mechanische Einflüsse

2004

Herausgegeber:
Bundesanstalt für Materialforschung und -prüfung (BAM)
Unter den Eichen 87
12205 Berlin
Telefon: +49 30 8104-0
Telefax: +49 30 8112029
E-mail: info@bam.de
Internet: www.bam.de

Herstellung und Verlag:
Wirtschaftsverlag NW
Verlag für neue Wissenschaft GmbH
27568 Bremerhaven
Telefon: +49 471 94544-0
Telefax: +49 471 94544-77/-88

Layout: BAM-Referat G.1

ISSN 1613-4249
ISBN 3-86509-136-9

Technische Universität Dresden

Störungen in der Charakteristik von Faser-Bragg-Gitter-Sensoren durch lokale thermische und mechanische Einflüsse

Solomija Lebid

von der Fakultät Elektrotechnik und Informationstechnik
der Technischen Universität Dresden
zur Erlangung des akademischen Grades eines

Doktoringenieurs

(Dr.-Ing.)

genehmigte Dissertation

Vorsitzender:	Prof. Dr.-Ing. habil. G. Gerlach	Tag der Einreichung:	16.12.2002
Gutachter:	Prof. Dr.-Ing. Ch. Schäffer	Tag der Verteidigung:	18.06.2003
	Prof. Dr. J. Bobitski		
	Prof. Dr.-Ing. W. Daum		

Dresden University of Technology

Perturbations in behaviour of fibre Bragg grating sensors introduced by local thermal and mechanical influences

Solomija Lebid

a dissertation submitted to
the Department of Electrical Engineering and Information Technology
of Dresden University of Technology
in partial fulfilment of the requirements for the Degree of

Doctor of Engineering

accepted Dissertation

Head of Committee:	Prof. Dr.-Ing. habil. G. Gerlach
Supervisor:	Prof. Dr.-Ing. Ch. Schäffer
	Prof. Dr. J. Bobitski
	Prof. Dr.-Ing. W. Daum

Acknowledgements

This thesis is the result of several years work at National University "L'vivska Polytechnika" (L'viv/Ukraine), the Federal Institute for Materials Research and Testing, (Berlin/Germany) and Dresden University of Technology (Dresden/Germany) and it would not been possible without the help and support of many people.

Firstly, I would like to express my gratitude to my advisors: Prof. Christian Schäffer, Prof. Jaroslav Bobitski and Prof. Werner Daum for their inspiration, support, advice, encouragement, equally generous and wise guidance, and for the many things I learned from them during the past years.

I would like to express my gratitude to all colleagues at Dresden University of Technology, who supported final steps of my work. My special gratitude to my Supervisor, Prof. Christian Schäffer for his unstinting commitment to helping see this project through to its final completion.

Many thanks to Mr. Jens Peupelmann from Ingenieurbüro Jens Peupelmann (Dresden/Germany) for collaboration, discussions and all the practical things that I learned during experimental work. His insights into the measurement technique experience enriched every joint research.

I am very grateful for my years at the Laser Technique and Optoelectronic Systems Chair and I would like to thank to all my colleagues there for their friendship and their support. In particular I would like to express thanks to Dr. Volodymyr Fitio for motivation for my theoretical work and fruitful discussions. I have learned much from him, such as the way of thinking and the way of proceeding research theoretically.

My special thanks to all colleagues in the Federal Institute for Materials Research and Testing. To Prof. Hans-Ulrich Mittmann my gratitude for supporting my ideas and investigations, for believing in me and in what I do. Special thanks to Dr. Wolfgang Habel whose work inspired me to investigate some special practical aspects in sensor behaviour, for inviting me to the great world of large-structures monitoring with fibre optic sensors, for his help to reshape my research direction and find a way through numerous research possibilities, for his productive comments on a draft of the thesis. Many thanks to my research group, Mr. Detlef Hofmann, Mr. Frank Basedau and Mr. Toivo Gutmann, for fruitful discussions, assistance, collaboration, their time and patience in measurement set-ups creation, subtle sense of humour, and for making things simpler in everyday life. Many thanks to Mr. Jürgen Knapp, Dr. Christian Ullner and Dr. Andreas Subaric-Leitis for fruitful discussions, advice and knowledge of metrology, to Mr. Jörg Oblasser, Mr. Manfred Hätzel, Mr. Klaus Schumacher, Dr. Gerhard Kalinka, Mr. Lothar Buchta, Ms. Martina Bistritz, and Mr. Harald Götsch for their collaboration and patience during numerous tests I prepared, to

Mr. Wilfried Schulze-Eggeringhaus, Mrs. Bärbel Eggeringhaus, Mrs. Anke Barthelmeß for everyday smiles and support in information search I needed.

My special thanks to Dr. Jan Wójcik from Lublin University of Maria Sklodowska-Curie (Lublin/Poland) and Dr. Georg Kuka from Fiberware GmbH (Mittweida/Germany) for spiritual support and discussions on special types of optical fibres.

My special thanks to Mr. Richard Holmes, whose editing suggestions and precise sense of language contributed to the final copy of the thesis.

I must express my deepest gratitude to my family. I am deeply indebted to my husband, Maksym, for his emotional support and patience during development of my doctorate work for the past years.

And finally to all who offered assistance in the writing of the thesis: it is not your fault that I did not always listen to the advice you gave me.

Abstract

Novel fibre optic sensor (FOS) systems maintaining fibre Bragg gratings (FBG) are finding wide application for health monitoring of large-scale structures such as dams, bridges, towers, as well as aircrafts, robots, automotive vehicles, and in composite technology. The principal advantage of such type of sensors is that the measured information is wavelength encoded (an absolute quantity). The main advantages include small size, immunity against electromagnetic field, good resolution, high sensitivity, and possibility to work in adverse environment. Especially small dimensions of the sensor allow its application for investigation of composite materials. The use of sensors enables to get information in areas, where other sensors would affect the structure or the material. On the other hand, it is important to keep signal stability of the sensor to the measured value of interest and obtain reliable data. Intimate embedment produces, however, additional perturbations affecting optical fibre sensor such as general mechanical stress, microbending, bending, and point-wise transverse load, which result in such undesirable sensor signal changes as attenuation, birefringence, spectrum broadening, sideband increasing, or small wavelength shift. No reliable knowledge about those effects and their consequences to the measured signal could be found in literature. This lack of knowledge led to the motivation of this work.

The thesis discusses behaviour of uniform short-period fibre Bragg grating signal under before mentioned perturbing influences. The main accent is made onto theoretical and experimental study of additional mechanical perturbations: point-wise transverse indentation, and microbending, arising at sensor operation depending on the grating integration type and measurement purpose. Response of this type of gratings (unapplied and integrated in/on the object to be mesaured) to the axial strain and composite-integrated gratings to the temperature is also investigated. Problems arising from the sensor fixing on/in the object to be measured are considered.

List of authors publications with regard to present work

1. Ya. V. Bobitski, V. M. Fitio, S. Yu. Zakalyk, Model of light propagation in fibre optic Bragg grating, Proceedings of 4th Scientific Conference, L'viv/Ukraine, vol. 2, 19-21, 1997.
2. Y. Bobitski, W. Fitio, S. Lebid, T. Wanchytski, Reflection spectrum calculation in optical fiber periodical structures (PS), Proceedings of 3rd International Conference MECHATRONIKA'97, Warszawa/Poland, vol. 2, 775-781, 1997.
3. Y. Bobitski, W. Fitio, S. Lebid, T.V. Fityo, Propagation of optical waves in quasiperiodical medium, Proceedings of International Conference Modern Problems of Telecommunications, Computer Science and Engineers Training (TCSET'98), L'viv/Ukraine, 163-165, 1998.
4. Y. Bobitski, W. Fitio, S. Lebid, T. Wanchytski, Creation of refractive index change in the optical fibre core, Proceedings of International Conference Modern Problems of Telecommunications, Computer Science and Engineers Training (TCSET'98), L'viv/Ukraine, 177-178, 1998.
5. S. Yu. Lebid, Y. W. Bobitski, W. M. Fitio, T. W. Fityo, Spectrum of Bragg grating reflection coefficient (RC) in optical fiber, Symposium Photonics West, OPTOELECTRONICS'98, San Jose/USA.
6. S. Yu. Lebid, Y. W. Bobitski, W. M. Fitio, T. W. Fityo, Spectrum of Bragg grating reflection coefficient (RC) in optical fiber, Proceedings of SPIE, vol. 3291, 165-173, 1998.
7. S. Lebid, Ya. Bobitski, T. Więcek, W. Fitio, Fiber-optic temperature sensor, Proceedings of International Conference on Optoelectronic metrology (OM'98), Lancut/Poland, 127-130, 1998.
8. S. Yu. Lebid, Y. W. Bobitski, W. M. Fitio, T. W. Fityo, Optical wave propagation in quasiperiodic medium, Journal of the State University "L'vivska Polytechnica", vol. 343, 41-50, 1998.
9. S. Yu. Lebid, Y. W. Bobitski, W. M. Fitio, Fibre-optic temperature sensor, Patent on invention of Ukraine, No. 25555, 30.10.1998.
10. S. Lebid, W. Fitio, Ya. Bobitski, T. Więcek, Fiber-optic temperature sensor, Proceedings of SPIE, vol. 4018, 96-99, 1999.

11. S. Lebid, W. Fitio, Ya. Bobitski, Analysis of light propagation in fiber cladding gratings, Proceedings of SPIE, vol. 3801, 147-155, 1999.

12. Y. V. Bobitski, V. M. Fitio, S. Y. Lebid, T. V. Fityo, Reflection spectrum of quasiperiodical dielectric structure, Journal of Applied Spectroscopy, vol. 67, 5, 650-653, 2000.

13. Ya. V. Bobitski, V. M. Fitio, S. Yu. Lebid, Coupling between propagated modes in optical fibers with periodical structures, Journal of Semiconductor Physics, Quantum Electronics & Optoelectronics, vol. 4, 3, 2001.

14. S. Lebid, D. Hofmann, F. Basedau, W. Daum, Comparison of strain sensitivity of bare and structure integrated fiber Bragg gratings, Proceedings of International Conference Photonics Prague 2002, 101, 2002.

15. S. Lebid, T. Gutmann, W. Habel, J. Peupelmann, Ch. Schäffer, Influence of Perturbing Effects on Composite-embedded Fibre Bragg Grating Signals, Proceedings of 15th International Scientific Conference Mittweida (IWKM), 41-46, 2002.

16. W. Habel, S. Lebid, T. Gutmann, Characterisation of high-performance composites by using structure-integrated FBG sensors, TEST 2003, Nuernberg (May 12-14, 2003), in press.

17. S. Lebid, W. Habel, W. Daum, How reliable measure composite-embedded FBG sensors under the influence of transverse and point-wise deformation?, 16th International Conference on Optical Fiber Sensors (OFS-16), Nara, Japan, in press.

List of Symbols

α	Coefficient of thermal expansion of material (CTE)
α_m	Coefficient of thermal expansion (CTE) of the host material
α_n	Thermo-optic coefficient of the fibre
β	Propagation constant
$\delta\beta$	Correction of the scalar propagation constant β in the elliptical medium
$\delta\beta_x$, $\delta\beta_y$	Two parts of the scalar propagation constant correction $\delta\beta$ in the elliptical medium for x - and y - polarisation axes
$\delta\Lambda$	Difference of the FBG period
δn	Correction to the refractive index
$\delta n_{eff}(z')$	Bending-induced changes in the refractive index of the perturbed FBG
δr	Radial width of perturbed region
Δ	Fibre profile height parameter or relative index difference
$\Delta\beta$	Change of the propagation constant
$\Delta\beta_x, \Delta\beta_y$	x- and y- polarisations of the propagation constant change
$\Delta\varepsilon_x, \Delta\varepsilon_y$	Changes in a dielectric tensor in the result of applied transverse load
$\Delta\lambda$	Bandwidth of the FBG spectrum
$\Delta\lambda_{avg}$	Average wavelength change
$\Delta\lambda_{bending}$	Wavelength change resulting from bending
$\Delta\lambda_B$	Bragg wavelength change

$\Delta\lambda_{diff}$	Differential wavelength change resulting from birefringence
$\Delta\lambda_x$	Change of the Bragg wavelength along an x- polarisation axis
$\Delta\lambda_y$	Change of the Bragg wavelength along an y- polarisation axis
Δd	Deflection of the cantilever beam
Δl	Elongation of the grating
Δn	Refractive index variation along a grating
Δn_m	Refractive index change of the measurand
ΔT	Temperature change
ε	Strain
ε	Dielectric tensor or permittivity
ε_a	Permittivity constant
ε_x , ε_y , ε_z	Strain components
$\varepsilon_{z'}$	Axial strain along the axis z' of the bent fibre
ε_1	Amplitude of the variable component of the permittivity
ζ	Distance from the axis of the fibre
κ , κ_x , κ_y	Coupling coefficient and its components
$\kappa_{m,n}$, κ_2 , κ_3 , κ_4 , κ_5	Apodization functions for the coupling coefficient
λ	Propagating wavelength
λ_B	Bragg wavelength
λ_{KrF}	Wavelength of the KrF excimer laser
$\lambda_{prop.}$	Propagating wavelength
Λ	Period of the FBG

Λ_0	Period of the unperturbed FBG
Λ'	Period of the bent FBG
μ	Permeability tensor
ν	Poisson ratio
ν_m	Poisson ratio for the host material
ρ	Radius of an optical fibre core
$\rho(\Delta\beta,-L)$	Amplitude reflection coefficient
$\rho(z)$	Dependence of the amplitude reflection coefficient on the axis z
ρ_x , ρ_y	Fibre radius changes along the x - and y - axes for the elliptical cross-section
θ	Inclination angle of the grating plane
σ , σ_x , σ_y , σ_z	Stress components
$\varphi(z')$	Part accounting perturbations in a grating geometry
ψ	Scalar wave function
a , b	Ellipsoid dimensions
A	Amplitude of the phase mask
A_1	Incident wave amplitude
A_2	Reflected wave amplitude
A_{1x}, A_{1y}	Forward wave amplitudes for x- and y- polarisation axes
A_{2x}, A_{2y}	Backward wave amplitudes for x- and y- polarisation axes

B	General birefringence of the fibre
B_G	Geometrical correction of birefringence
B_p	Normalised birefringence of the optical fibre
B_S	Stress correction of birefringence
C	Lame's constant
C_k	Fourier transform coefficients
C_m	Lame's constant for the host material
$\frac{d\rho(z)}{dz}$	z -axis differentiation of the amplitude reflection coefficient
$\frac{dn}{dT}$	Thermo-optic coefficient of the fibre
$\frac{dn_{eff}}{dT}$	Thermo-optic coefficient of the grating
D	Diameter of the fibre core
e	Eccentricity
E	Young's modulus
$\vec{E}$, E_x, E_y, E_z, E_m	Electrical field and its components
G	Shear modulus
G_m	Shear modulus for the host material
h	Distance of the bend area from the neutral axis
$\vec{H}$, H_x, H_y, H_z	Magnetic field and its components
I	Induced photocurrent

k , k_0	Wave number
k	Splitting ratio (pp. 3-13, 3-14) of the fibre coupler
k	Index of the Fourier coefficients (Attachment E)
$K_\varepsilon, K_z, K_h,$ K_T, K_S	The coefficients that can be defined experimentally and which characterises grating sensitivity to an axial strain, transverse strain and temperature
L	Length of the grating
m	Fringe visibility of the index change or contrast of the pattern
$M(-L)$	Function used for the verification of gratings apodization model
n_{cl}	Refractive index of the fibre cladding
n_{co}	Refractive index of the fibre core
n_{eff} , n_0 , n_{silica} , n_x , n_y , n_1 , n_2 , n_3	Refractive index of the grating and its components
n_m	Refractive index of the measurand
N	Number of grating planes
p_e	Effective strain-optic constant
p_{11}, p_{12}	Pokel's coefficients of the strain-optic tensor
P	Normalised propagation constant
P_0	Initial power of the propagating light
P_1	Power that reaches detector 5 (see Figure 3.9)
P_i	General normalised propagation constant
P_T	Power that reaches detector 6 (see Figure 3.9)
$P_x^{\,0}$, $P_y^{\,0}$	Normalised propagation constants for an elliptical fibre core (x- and y-axes)

P_x^G , P_y^G	Geometrical corrections for the normalised propagation constants (for x- and y- axes)
P_x^S , P_y^S	Stress corrections for the normalised propagation constants (for x- and y- axes)
r_0	Spot size in the circular fibre
R	Reflectivity of the grating
R_b	Bending radius
s	
s_e	Elliptical interface
S	Sensitivity of the sensor element
S_f	Proportionality factor or responsitivity of the photodetector
T	Temperature
V	Fibre parameter
x_0, y_0	Spot size in the elliptical fibre

List of Abbreviations

AOTF	Acousto-optic tunable filter
BBS	Broadband source
CCD	Charge-coupled device
CDM	Coherence-division-multiplexing
CFP	Carbon-fibres reinforced polymer
CTE	Coefficient of thermal expansion of material
EMI	Electromagnetic interference
FBG	Fibre Bragg grating
FDM	Frequency-division-multiplexing
FFP	Fabry-Pérot filter
FOS	Fibre optic sensor
FRC	Fibre-reinforced composite
FSR	Free spectral range
MOI	Micron Optics Inc.
MZI	Unbalanced optical fibre Mach-Zehnder interferometer
ORMOCER®	"Organically modified ceramics" trademark of a fibre coating
OSA	Optical spectrum analyser
PVC	Polyvinylchloride
PZ	Piezoelectric element
R&G	Trademark of the two component glue
SDL	Swept diode laser
SDM	Spatial-division-multiplexing
SEM photos	Scanning electron microscope photos

SLI	Swept laser interrogator
SR	Sensor rod
TDM	Time-division-multiplexing
TL	Tunable laser
UV	Ultra violet
WDM	Wavelength-division-multiplexing
X60	Trademark of epoxy glue

1 Introduction

2 Background

2.1 Fabrication of FBGs 2-1

2.1.1 Interferometric fabrication technique 2-1

2.1.2 Phase-mask technique 2-2

2.1.3 Point-by-point technique 2-5

2.2 FBG as the fibre optic sensing element 2-6

2.2.1 Operation 2-6

2.2.2 Properties and characteristics 2-7

2.3 Application examples of the FBG sensors 2-11

2.4 Signal recording methods 2-14

2.5 Technological problems 2-17

3 Theoretical investigations of FBG signal changes due to perturbing influences

3.1 Analysis of unperturbed and uniform FBG spectrum 3-1

3.1.1 Calculation of the FBG reflection spectrum 3-3

3.1.2 Wave propagation in quasi-periodical medium 3-5

3.2 Light propagation in FBG exposed to the external influences 3-11

3.2.1 Temperature influence 3-11

3.2.2 Analysis of a birefringence effect 3-14

3.2.3 Effects of light propagating through the bent FBG 3-20

4 Investigations of thermal and mechanical influences

4.1 Strain sensitivity 4-1

4.1.1 Uniaxial strain of the bare grating 4-2

4.1.2 Uniaxial strain of a FBG fixed in a sensor rod 4-8

4.1.3 Embedded gratings 4-11

4.2 Temperature sensitivity 4-22

4.2.1 FBGs response to applied temperature changes 4-22
4.2.2 Embedded FBGs 4-24
4.3 Bending of FBGs 4-29
4.3.1 Uniform bending of free gratings 4-29
4.3.2 Bending behaviour of gratings attached to a bent cantilever beam 4-30
4.3.3 Bending behaviour of gratings embedded in a bent cantilever beam 4-33
4.3.4 Bending behaviour of gratings centrally embedded in a three-point bent beam 4-37
4.4 Transverse mechanical influences 4-40
4.4.1 Transverse stress applied to free FBG 4-40
4.4.2 Point-wise transverse load onto FBG 4-42

5 Summarised results
5.1 Overview of obtained theoretical results 5-1
5.2 Overview of experimental results 5-2
5.2.1 Free FBGs 5-2
5.2.2 FBG sensor rod 5-4
5.2.3 Attached FBGs 5-5
5.2.4 Embedded FBGs 5-5
5.3 Conclusions 5-7

6 Conclusions and Recommendations

7 Outlook for further investigations
7.1 Estimation methods of gratings parameters 7-1
7.2 Periodical structures on the fibre cladding for specific sensor applications 7-2

Attachment A

Light propagation in an optical fibre the step-index profile

Attachment B

Coupled mode theory for the unperturbed and uniform FBG

Attachment C

Approximation of the rectangular cross-section for the elliptical cross-section of optical fibres

Attachment D

FBGs used for research

Attachment E

Fibre cladding periodical structures

Bibliography

1 Introduction

The sensor market requires reliable and precise measurement techniques for some special purposes, such as materials research and large-scale object monitoring, where fibre Bragg gratings (FBGs) have a chance to replace existing methods of monitoring and in some cases can be the only solution to deliver reliable information regarding a measurand [Fuh98], [Voh98], [Lau99], [McK00], [Wie00], [Woo00], [Bug00], [Lat01], [Leu01], [Ten01], [Aoy01], [OLE02], [Nel00], [Gra00], [Lop02].

FBGs are tunable wavelength-selective filters, sensitive to strain and temperature, which allows their application as sensors in the field of metrology [Dak88], [Gra95], [Udd96]. The key advantage is that the measured information is wavelength encoded (an absolute quantity). This makes a sensor self referencing, independent of fluctuating light levels, so that the system is immune to source power and connector losses that plague many other types of fibre optic sensors. The ability to act, as an "absolute" strain gauge is not available with standard foil strain gauges and opens up many applications for materials, mechanical and civil engineering [Jin97], [Lau01a], [Moe01] [Bosi02].

It also offers advantages such as remote operation, high sensitivity, imperviousness to electromagnetic interference (EMI), nuclear radiation, explosive or chemically aggressive media, and low or high temperature conditions [Mas97], [Schu98], [Oth99].

One more advantage of fibre Bragg gratings is their small diameter. This enables their integration into materials and structures, where small dimensions are necessary, such as endoscopes for monitoring brain and arteries of the human body, pH-, pressure-, or temperature- measurement, local damage inspection, or internal strain monitoring in composite materials with high localisation, strain resolution, and response [Dak88], [Gra95], [Rao97], [Wan99], [Oth99], [Kas99], [Gau99], [Gra00], [Oka00], [Ham00], [Leu01], [Pet02], [Oka02]. Their very low insertion losses and narrow band wavelength reflection offer convenient serial multiplexing along a single monomode optical fibre for which any fibre optic network can be implemented (star, series, parallel, ring) and modified over the long term, thereby increasing flexibility. FBG sensors make possible localised, distributed, or quasi-distributed monitoring of different materials and structures such as bridges, dams, towers, as well as ships, aircrafts, spacecrafts, turbines in power plants, rotor blades in wind energy, vehicles and highways [Maa97], [Ala97], [Tru99b], [Boss99], [Mou01], [Ferr02].

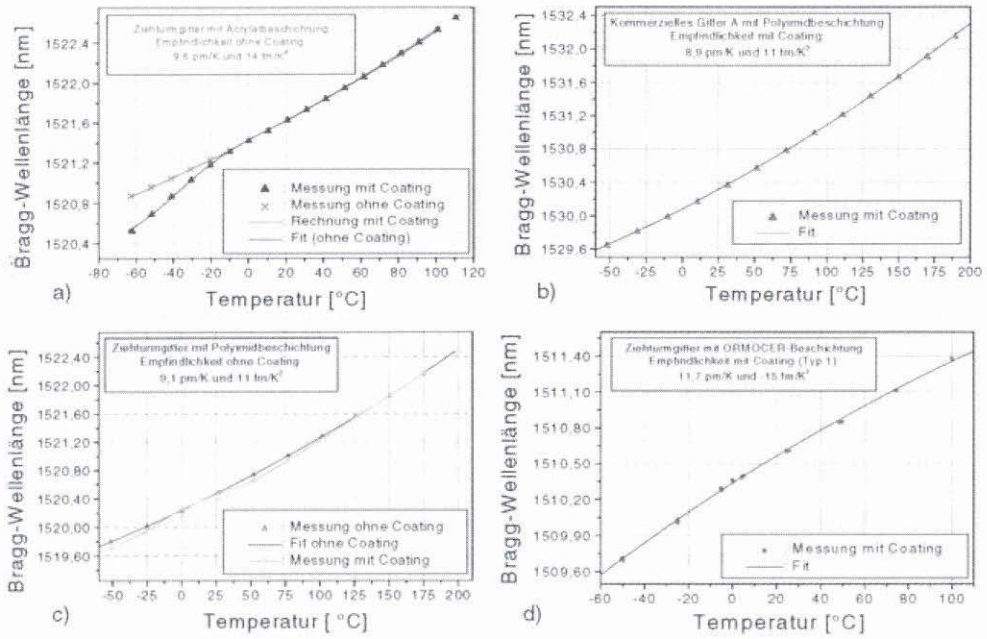

Figure 1.1: Thermal sensitivity of different Bragg gratings: a) draw-tower acrylate-recoated gratings (thermal sensitivity without coating 9.6 pm/K); b) commercial polyimide-recoated grating (thermal sensitivity without coating 8.9 pm/K); c) draw-tower polyimide-recoated grating (thermal sensitivity without coating 9.1 pm/K); d) draw-tower ORMOCER®-recoated grating (thermal sensitivity without coating 11.7 pm/K) (After: [Tru01]).

On the other hand, some problems connected with grating integration technology and signal reading still exist. Usually, the grating is prestressed with a coating material, which could be a reason of subsequent failure of the grating. Even in the case of draw-tower gratings, a coating influence also has to be taken into consideration (see *Figure 1.1a*). Therefore, acrylate-recoated (AC) gratings are usually not recommended for applications where long-term stability and reliability are required (see *Figure 1.2*). In non-inert environments, cracks propagate due to the combined influence of stress and chemicals, especially water. Polyimide-recoated (PI) gratings showed nearly linear thermal response within the temperature range from -50°C to 200°C (see *Figures 1.1b-c*). In a solution with pH = 13.9 and under mechanical loading over 3.5 months with an applied load of 5 N this coating type showed critical failure (see *Figure 1.3*). ORMOCER® coating showed also nearly linear response to the thermal loading from -60 °C to 100 °C (see *Figure 1.1d*). After 58 days in a solution with pH = 13.7 and increased static loading until 23.5 N it was cracked and then damaged (see *Figure 1.4*).

Bragg gratings are intrinsic devices and therefore susceptible to high strain-temperature sensitivity and birefringence. They also have unique response to strain and temperature gradients along their length, which can be undesirable in some applications because they introduce distortions into the grating signal recorded. Therefore, the position of the grating inside the structure or material is critical for reliable operation.

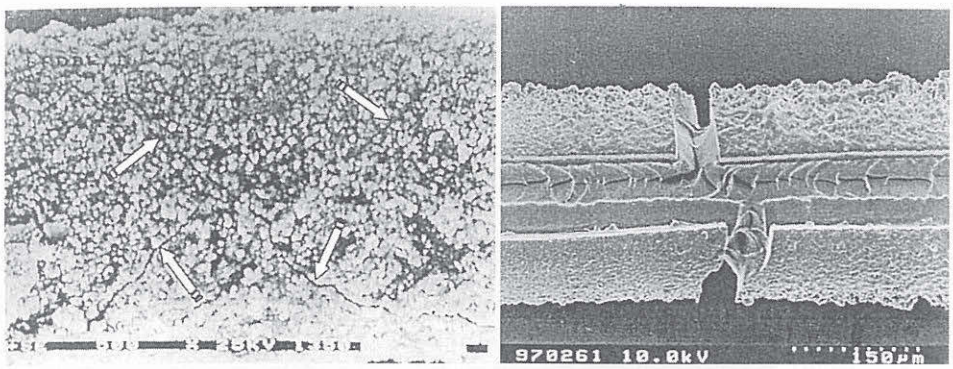

Figure 1.2: AC-coatings: a) mortar-embedded and after 28 days revealed (arrows show mini-cracks); b) 35 months concrete-embedded fibre (pH = 11) (After: [Hab00]).

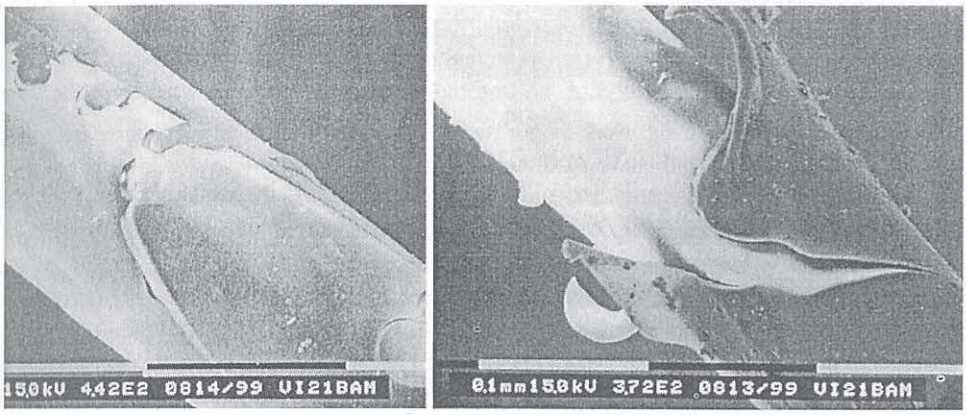

Figure 1.3: PI coating after combined concrete integration (ph = 13.9) and mechanical loading (5 N) until damage (after 3.5 months) (After: [Hab00]).

Material-integrated sensors require very precise and well-prepared embedment technology to avoid considerable undesirable material influences which perturb the grating, such as general stress after embedment, microbending and point-wise load. As a result of such perturbations, signals of installed FBG sensors can suffer from attenuation, birefringence, spectrum broadening, sideband increasing, or wavelength shift. This affects the signal of the sensor. Therefore, reliability and durability are of equal importance for the industrial application of such type of sensors and have to be considered during the design, manufacture and operation of sensors.

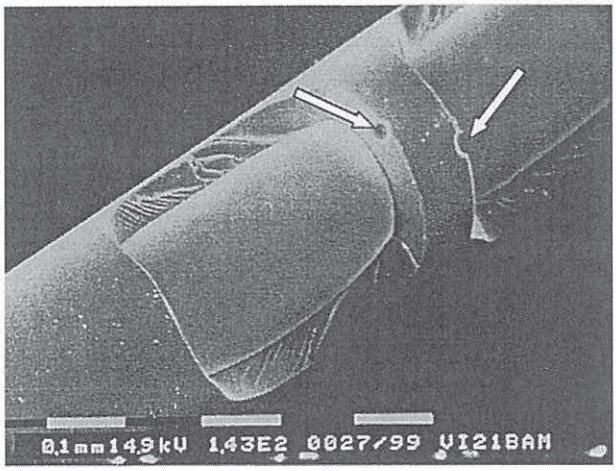

Figure 1.4: ORMOCER®-coating after 58 days in a solution (pH = 13.7). Critical failure occurred at static load of 23.5 N (After: [Hab00]).

The initial aim of the present work is to study, systematise and analyse theoretically and experimentally undesirable and unavoidable perturbations such as transverse stress, microbending, and point-wise transverse indentation affecting FBG sensor signals and to analyse FBG responses to the uniaxial strain and temperature for different types of sensors. Following this introduction, Chapter 2 presents a literature review of the fabrication technologies, with an overview of the properties of FBGs, existing sensor design, and sensing methods. After this background information, theoretical methods of signal evaluation of uniform FBG and some theoretical approaches in evaluation of spectrum of perturbed FBGs are considered in Chapter 3. Experimental data regarding investigations of uniform or sensor integrated FBG response to the uniaxial strain and temperature as well as influence of undesirable perturbations such as general transverse stress, point-wise transverse indentation, and bending are described in Chapter 4. Analysis of theoretical and experimental results follows in Chapter 5. Chapter 6 includes conclusions regarding the investigated effects and appropriate applications. Finally, recommendations regarding points for further investigation are made in Chapter 7.

2 Background

Fibre Bragg gratings are currently an object of numerous investigations because of their wide applications in telecommunications and sensor technology. A uniform FBG is an internal fibre optical filter that is tuned to a specific wavelength [Dak88], [Gra95], [Hab01], [Will01], [Nel01], [Oth99], [Kas99], [Hil78], [Miz93], [Mas97], [Bob97a]. The filter consists of grating planes with a refractive index variation in the range of 10^{-2}- 10^{-6} contrary to the rest of the fibre core. This element is characterised by the spectral data such as central reflected wavelength λ_B (Bragg wavelength), bandwidth, isolation, and transmittance [Ros00], [Gen98]. This chapter provides an overview of key details regarding behaviour, fabrication and operation of such elements.

2.1 Fabrication of FBGs

Fabrication of the simple Bragg gratings could be divided onto three parts: the first is the usual holographic technology, the second is recording of in-core fibre gratings using photolithography with phase mask, and the third is point-by-point inscription [Hil78], [Hil84], [El-89], [Gle89], [Hil91], [Lebb92], [Jun93], [Miz93], [Hil94], [And94], [Erd94], [Byr96], [Bil96], [Atk97], [Epw97], [Lew97], [Ngu97], [Byr98], [Yab99], [Bre99], [Joh00], [Mil00], [Stu00], [Hag00], [Tru01], [Schi01]. The first trial in writing of Bragg gratings into the fibre core, 1978, could be classified as internal grating inscription. Such definition comes from the fact that method introduce permanent changes into refractive index of the fibre core by producing of standing wave from coherent radiation at 514 nm reflected from the fibre ends. Such a permanent interference picture was called an "internally" written grating [Hil78], [El-89], [Bil96], [Atk97].

2.1.1 Interferometric fabrication technique

In the early 1980s, first trials to create a periodical structure on the optical fibre core were conducted for telecommunication applications, such as a dispersion element (to couple one or more defined wavelengths out of the fibre at defined angle or to couple one or more defined wavelengths from planar into fibre waveguide) and an optical fibre filter [Mah78], [Sva86], [Sva89], [More89], [Syt94], [Hil97]. Standard and one-beam holographic schemes were applied for such purposes (see *Figure 2.1*). This technique allowed fabrication of strong periodical structures in the fibre core. The possibility to write periodical structures inside the fibre core brought them wide application. Morey *et al.* reported the first successful external writing with interference patterns from two beams irradiated from two UV light sources [More89].

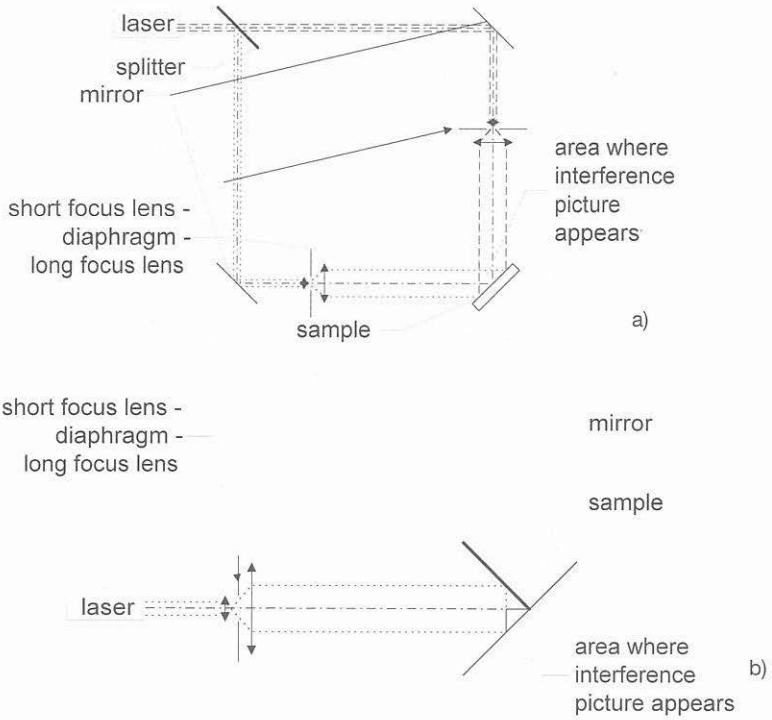

Figure 2.1: Two holographic schemes: a) common holographic scheme b) one-beam holographic scheme.

Two beams create an interference pattern in the photosensitive fibre core, which introduces changes into refractive index of the fibre core. Changing the angle between the two beams can change the period of the resulting structure. On the other hand, holographic schemes have very strong aberrations determined by difference of recording and reproduction beams. A solution to this problem was proposed by using objective in one arm of the holographic scheme or by using intermediate holograms (see *Figure 2.1*).

The one-beam holographic scheme found wide application because it uses fewer optical elements and has the advantage in manipulation of the recorded structure period. Problems existing in such technology are connected with strict requirements on the mechanical stability of the optical scheme and strict control of spatial and time coherence of two recording beams.

2.1.2 Phase-mask technique

The next step in fibre gratings fabrication technology development was the application of the phase mask for fibre Bragg gratings fabrication as reported in the early 1990s by the two largest laboratories in the branch: Communications Research Centre, Canada, and AT&T Bell Laboratories, NJ, USA [Hil78], [Hil84], [Mel89], [Hil91], [Hil96], [Miz93], [Jun93], [Erd94], [Bil96], [Yab99].

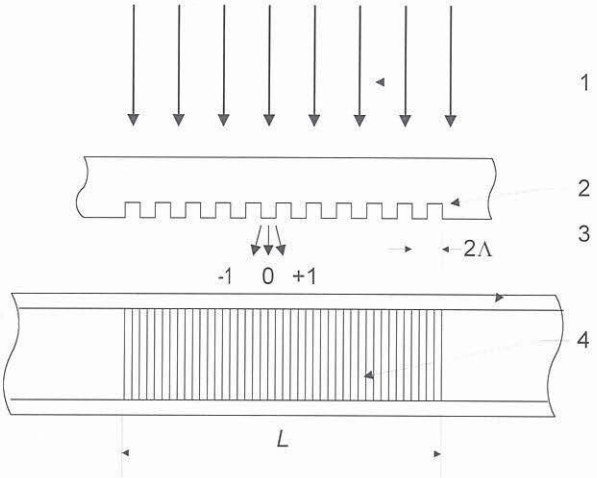

Figure 2.2: Fabrication of the uniform FBG: 1 – laser irradiation, 2 – phase mask, 3 – single mode fibre, 4 – FBG.

Method of gratings imprinting into the fibre core after Hill involves contact imprinting through the phase mask (see *Figure 2.2*). The optical fibre has to be in a contact with or very close to the phase mask under irradiation of the excimer laser. KrF or ArF excimer lasers irradiating at 248 nm or 193 nm respectively, which work at pulse repetition rates of 50 - 75 pulses/s at intensity ranging for 100 - 1000 mJ/cm^2 could be used [Hil97]. The period of the grating was two times less than the period of the phase mask. The grating was inscribed by interference pattern, which appears in the result of + 1 and – 1 orders of diffraction of beams passed through the phase mask. The strength of recorded gratings is not defined by the capacity of irradiation of the writing beam, but by resolution of the interference pattern. Therefore, the main importance is made to the quality of the phase mask. Amplitude of the phase mask is defined by the equation

$$\frac{4\pi(n_{silica}-1)A}{\lambda_{KrF}} = \pi + 2\pi n, \tag{2.1}$$

where λ_{KrF} is the wavelength of the KrF excimer laser, which photo-induce the refractive index changes Δn in optical medium with the refractive index n_{silica} and A is an amplitude of the phase mask, and $n = 0, 1, 2,..$ [Hil94]. Such amplitude is designed to diffract approximately zero irradiation in 0-order of diffraction through the phase mask. Actually, diffraction in 0-order of diffraction equals 1 % and in + 1- and – 1- orders of diffraction is more than 40 %. With the phase mask technique the spatial and time coherence which were required in previous schemes is not longer necessary. A lot of improvements or changes have since been made to this original technology to achieve higher quality devices or devices of other geometry, such as tilted, chirped, long or overwritten gratings. It is possible to write structures with different periods by definition of the distance between phase mask and fibre, using a projection system enlarging or diminishing interference pattern [Miz93], or to increase fibre photosensitivity introducing heat sources or

additional lasers [Byr96]. *Figure 2.3* presents FBG fabrication technology with phase mask, which uses the projection scheme after [Miz93].

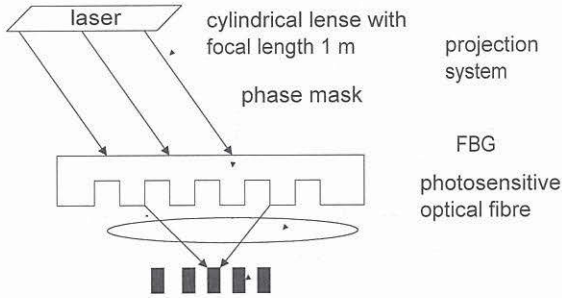

Figure 2.3: Photolithography with a phase mask using projection system.

An example of the grating transmission spectrum is shown in *Figure 2.4*. Reflection achieved with such technology reaches 90 %. It could reach around 100 %, which is important for telecommunication application. Such a fabrication method allows control of the refractive index change by amplitude modulation of the incident beam. Byron *et al.* reported achieving amplitude modulation by introducing a heating source into the fabrication scheme [Byr96]. This also increases photosensitivity of optical fibres. Introducing a CO_2 laser focused irradiation into the fibre will create a differential heating source in the fibre, where grating will be inscribed. Temperature is defined by intensity of propagating beam through the fibre and duration of the irradiation.

A standard telecommunication fibre is not the best solution for writing of some types of FBG. A low difference between core-cladding refractive indices leads to the radiation mode loss at wavelengths shorter than FBG wavelength. Additional increasing of the fibre photosensitivity is required to achieve better refractive index change in the fibre core [Bil96], [Lew97], [Ngu97].

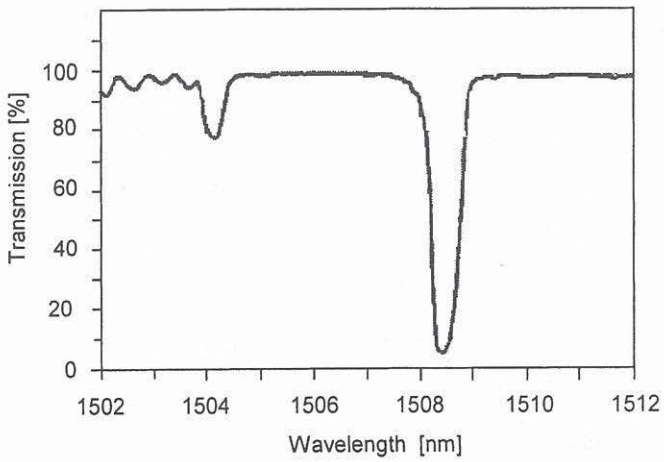

Figure 2.4: Transmission spectrum of AT&T Bell Labs FBG (After: [Miz93]).

One of the ways to increase fibre photosensitivity is "hydrogen loading": molecular hydrogen is "loaded" into the fibre in a high-pressure, low-temperature diffusion process [Miz93]. This method allows achievement of 10^{-2} changes in the refractive index of the fibre core [And94], [Bil96]. Another possibility for photosensitivity increasing could be optical fibre doping with boron or Sn co-doping with germanium. UV-induced index changes in such fibres reach approximately 10^{-3}. Finally, high-pressure cold hydrogen soaking demonstrated refractive index changes 10^{-2} [Kro91].

2.1.3 Point-by-point technique

The present fabrication technique consists in creating a refractive index change in one part of the fibre core after another along the fibre axis. Fabrication scheme consists of single-pulse UV excimer laser, a mask with a slit, focusing lens, and precise motorised translational stage equipment. Mask and lens are mounted on the translational equipment and the mask is situated with a slit perpendicular to the fibre. UV light from excimer laser passes through a mask slit, focuses on the side of the optical fibre through focusing lens and induces refractive index changes inside the narrow part of the fibre core. After inscription of one pitch of the future grating, positioning equipment translates the mask and lens into the step Λ along the fibre axis. The period Λ corresponds to the pitch of the resulting grating.

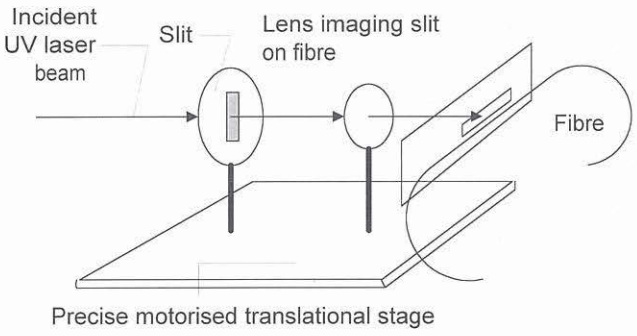

Figure 2.5: Schematic representation of point-by-point recording of FBG.

Such fabrication technology allows inscribing of gratings of any length and with any period, but a precise and stable motorised translational stage is very important for the creation of strong and high quality gratings. Grating recorded by Malo [Mal93] had 225 index perturbations resulting in the length 360 μm and reflected 70 % at the central wavelength 1536 nm. Malo *et al.* used KrF single-pulse excimer laser irradiating at 248 nm, a mask with 15 μm slit, and a lens with 15 mm focal length [Hil97]. Grating was written from the flat side of D-type polarisation maintaining fibre. Achieved refractive index modulation was $\Delta n = 6 \times 10^{-3}$.

One of the special aspects of such fabrication technology is that it is not possible to write the first order FBG because of the width of the photo-induced index perturbation. FBGs reflecting second and third orders were fabricated instead. Disadvantages of present technology include errors occurring due to the thermal effects and small variations in fibre strain during process. It is also important to

note that it is a very time-consuming procedure. A very stable and precise submicron translational system is essential for this technology. This method could be applied for custom fabrication.

2.2 Fibre Bragg gratings as the fibre optic sensing element

The application of an FBG as the fibre optic sensing element requires detailed understanding of the principles and peculiarities of its operation, properties, such as sensitivity to the strain and temperature, and additional effects arising in the result of influences of the medium such as general or local transverse stresses.

The simplest case of the FBG could be represented as a periodic modulation of the refractive index along a single mode silica fibre core. This type of grating is called uniform. Phase fronts of such grating are perpendicular to the longitudinal fibre axis and its planes have the constant period Λ.

2.2.1 Operation

Propagation of light through the FBG is shown schematically in *Figure 2.6*. Light propagated through the optical fibre with FBG will be reflected from the each plane of the FBG, if the wavelength corresponds to the Bragg condition

$$\lambda_B = 2n_{eff}\Lambda, \tag{2.2}$$

where λ_B is a Bragg wavelength, n_{eff} is an effective refractive index of the fibre core, and the distance between gratings planes is Λ (period of the FBG).

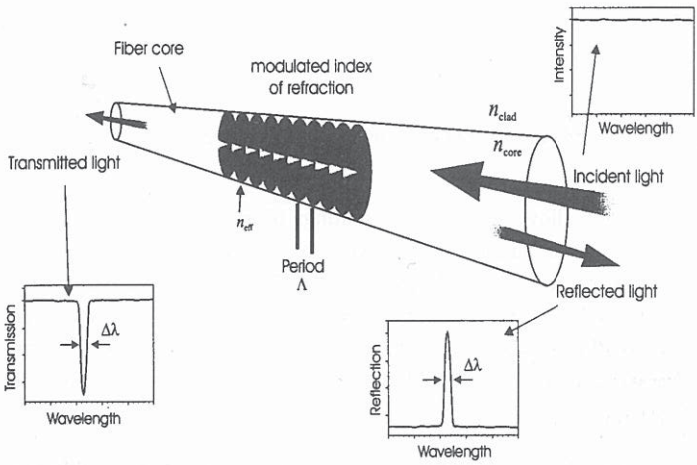

Figure 2.6: Schematic drawing of light propagation through the optical fibre with FBG on the fibre core (After: [Oth99]).

The other part of the light will be transmitted through the grating and propagating farther along the fibre (see *Figure 2.6*). Resonance light, which does not coincide with the Bragg wavelength, will be partially reflected at each of the planes of the grating because of the index difference. Such reflection accumulates over the length of the grating. For example, the 1 mm-long FBG at the wavelength 1500 nm with the strong refractive index modulation $\Delta n = 10^{-3}$ will reflect approximately 0.05 % of the off-resonance incident light [Mas97], [Oth99], [Kas99], [Tru01]. Spectra of incident, reflected and transmitted light are shown in *Figure 2.6*. Reflected light will form a peak with the central wavelength defined by Bragg condition (2.2) and the bandwidth

$$\Delta\lambda = \lambda_B m \sqrt{\left(\frac{\Delta n}{2n_{eff}}\right)^2 + \left(\frac{1}{N}\right)^2}\,, \tag{2.3}$$

where m is a fringe visibility of the index change (approx. 1 for strong gratings and approx. 0.5 for weak gratings), N is a number of grating planes [Rus93], [Erd97], [Rao97]. Transmitted light will form a notch, central wavelength of which will correspond to the Bragg condition and the bandwidth $\Delta\lambda$ (2.3). The grating, because of its geometry, is sensitive to the strain and temperature influences, which result in the change of the FBG's period Λ and an effective refractive index modulation of the FBG that make it important for sensor applications.

2.2.2 Properties and characteristics

Properties of the FBG, such as temperature and strain sensitivity, are the reason for their wide application in sensor field. However, being an intrinsic device, an FBG is sensitive to the gradient stress and temperature influence along its length. One of the effects which appear as a result of stress- or temperature- induced geometry changes is birefringence observed in FBG spectrum. This effect can be undesirable in some applications and therefore have to be investigated.

Strain and temperature sensitivity

The Bragg wavelength of the grating is a function of grating period and effective refractive index of the fibre core along the Bragg condition (2.2). The distance between grating planes Λ defines the wavelength reflected by the grating (see *Figure 2.6*). Tuning fibre core geometry along the fibre axis can change the wavelength reflected from the grating. Such properties make FBGs ideal temperature sensors or strain gauges [Jin97], [Mag97], [Sir98], [Tan96], [More89], [LeBl96], [Hua95a], [Hua94], [Hua95b], [LeBl00], [Ohn97], [Lin98]. Thus, temperature or strain influences can be measured with FBG sensor by monitoring of Bragg wavelength. When it is important to measure only one of those influences, the other has to be eliminated. For analysis of strain influence onto FBG, it is important to exclude temperature influences and vice versa.

The mathematical model for the calculation of strain and temperature influence on the FBG is well developed [Oth99], [Kas99]. By differentiation of equation (2.2) for temperature and elongation, the Bragg wavelength change will appear as follows:

$$\Delta\lambda_B = 2\left(\Lambda\frac{\partial n_{eff}}{\partial l} + n_{eff}\frac{\partial\Lambda}{\partial l}\right)\Delta l + 2\left(\Lambda\frac{\partial n_{eff}}{\partial T} + n_{eff}\frac{\partial\Lambda}{\partial T}\right)\Delta T\,. \tag{2.4}$$

Estimation of the dependence of the Bragg wavelength change $\Delta\lambda_B$ on the elongation of the grating Δl and the temperature change ΔT is shown in *Figure 2.7*. To express only temperature dependence from equation (2.4), it is taken into consideration that there are no strain effects

$$\Delta\lambda = \lambda_B\left(\alpha + \frac{1}{n_{eff}}\frac{dn_{eff}}{dT}\right)\Delta T, \tag{2.5}$$

where α is a coefficient of thermal expansion (CTE), n_{eff} is an effective refraction index of medium, and $\frac{dn_{eff}}{dT}$ is a thermo-optic coefficient. All values α, n_{eff} and $\frac{dn_{eff}}{dT}$ depend on the material of the medium and could vary [Oth99], [Rei98], [Lin98], [Wag96], [Kim92], [Stee95]. Following values for: $\alpha = 0.55 \times 10^{-6}$ 1/K, $n_{eff} = 1.482$, and $\frac{dn_{eff}}{dT} = 11 \times 10^{-6}$ 1/K can be taken for common silica glass fibre.

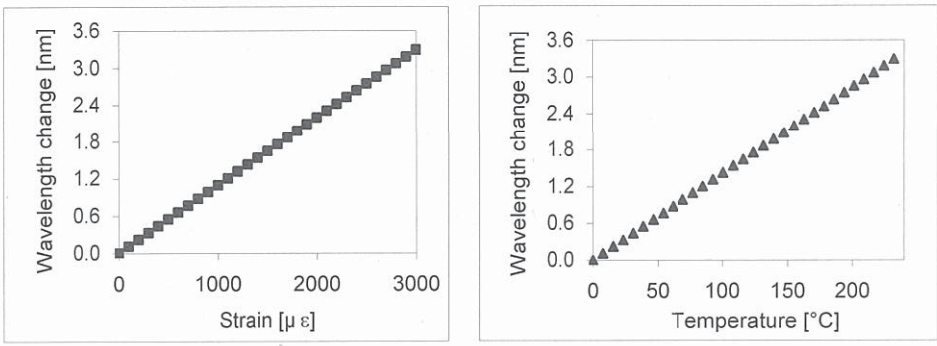

Figure 2.7: Dependence of a Bragg wavelength change on linear strain $\Delta\lambda(\varepsilon)$ and temperature $\Delta\lambda(T)$.

For modelling of strain influence onto FBG, it is taken into consideration that geometry of the medium is cylindrical and homogeneous in all directions. In the case of pure axial strain formulation (2.4) transfers to the appearance

$$\frac{\Delta\lambda_B}{\lambda_B} = K_\varepsilon \varepsilon_z, \tag{2.6}$$

where ε_z is an axial strain along the fibre axis z, $K_\varepsilon = (1 - p_e)$ is an axial strain Bragg wavelength coefficient, which can be defined experimentally and p_e is an effective strain-optic constant

$$p_e = \frac{n_{eff}^2}{2}[p_{12} - \nu(p_{11} + p_{12})], \tag{2.7}$$

where p_{11}, p_{12} are Pokel's coefficients of a strain-optic tensor, and ν is a Poisson's ratio.

Young's modulus for silica glass fibre is 74000 N/mm^2, and the effective strain-optic constant, calculated from (2.7) for a silica glass, is 0.213 [Dav96], [Oth99]. Below are given calculated dependencies of the wavelength change on applied temperature and strain. For the Bragg grating with the central wavelength 1550 nm, calculated sensitivity to an axial strain is 1.2 pm/με and sensitivity to a temperature is 14 pm/K.

Transverse stress-induced effect

Bragg gratings have a unique, but not always desirable, response to the gradients in stress and temperature along the grating length as well as transverse stress influence. They are intrinsic devises and therefore susceptible to birefringence [Sny81b], [Law95], [Hua96], [Mart99], [Gue02]. The refractive index of the FBG will change and two plane-polarised waves will propagate, with the principal axes of polarisation parallel (y) and perpendicular (x) to the direction of applied load (see *Figure 2.8*).

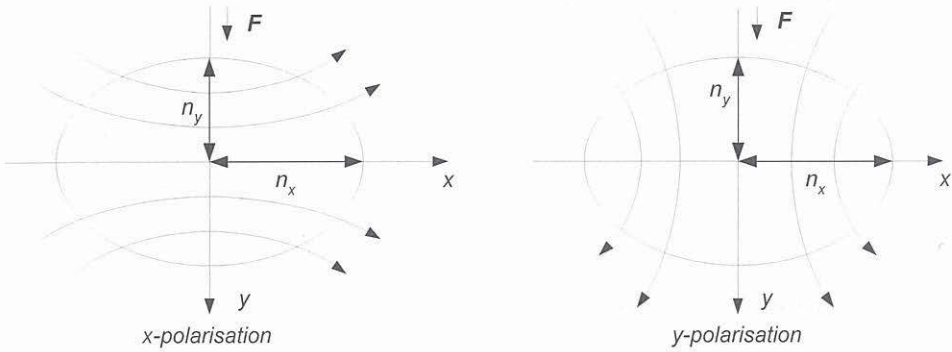

Figure 2.8: Orientation of the transverse electric field for the x-polarised (a) and y-polarised (b) fundamental modes on an arbitrary step-profile fibre [Sny81b].

Influence of the uniaxial, transverse strains and temperature on the Bragg wavelength change in x- and y- polarisation axes are given by

$$\begin{aligned}
\frac{\Delta\lambda_x}{\lambda_B} &= \left(1-\frac{n_{eff}^{\ 2}}{2}p_{12}\right)\varepsilon_z - \frac{n_{eff}^{\ 2}}{2}p_{11}\varepsilon_x - \frac{n_{eff}^{\ 2}}{2}p_{12}\varepsilon_y + \left(\frac{n_{eff}^{\ 2}}{2}(p_{11}+2p_{12})\alpha + \frac{1}{n_{eff}}\frac{dn}{dT}\right)\Delta T, \\
\frac{\Delta\lambda_y}{\lambda_B} &= \left(1-\frac{n_{eff}^{\ 2}}{2}p_{12}\right)\varepsilon_z - \frac{n_{eff}^{\ 2}}{2}p_{12}\varepsilon_x - \frac{n_{eff}^{\ 2}}{2}p_{11}\varepsilon_y + \left(\frac{n_{eff}^{\ 2}}{2}(p_{11}+2p_{12})\,\alpha + \frac{1}{n_{eff}}\frac{dn}{dT}\right)\Delta T,
\end{aligned} \tag{2.8}$$

where ε_x, ε_y are transverse strains and ε_z is an axial strain. For the germanosilicate fibre this system of equations is obtained:

$$\frac{\Delta\lambda_x}{\lambda_B} = 0.7233\varepsilon_z - 0.1241\varepsilon_x - 0.2767\varepsilon_y + \left(6.1756\times10^{-6}\right)\Delta T,$$
$$\frac{\Delta\lambda_y}{\lambda_B} = 0.7233\varepsilon_z - 0.2767\varepsilon_x - 0.1241\varepsilon_y + \left(6.1756\times10^{-6}\right)\Delta T. \quad (2.8a)$$

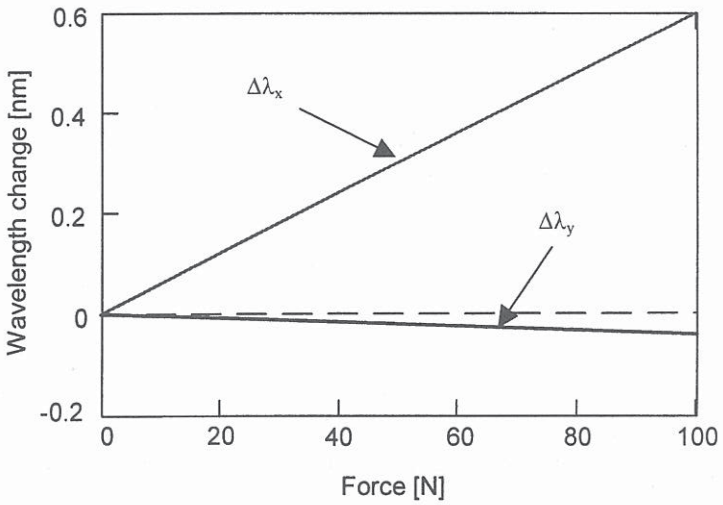

Figure 2.9: Calculated dependence of the Bragg wavelength on the applied force for x- and y-polarisation axis in a case of plane strain $\varepsilon_z = 0$.

An example of the Bragg wavelength changes along x - axis and y - axis at the plain strain for the 2 mm long FBG with (1550 nm) is presented in *Figure 2.9*.

As follows from (2.8a), change of the wavelength under uniaxial strain is much larger than induced by transverse strains, which can be seen from calculated data. In some cases, transverse strains can achieve general influence of 50 % [Mart99]. Bare FBG in isotropic material will react for temperature, axial and transverse strains as follows [Stee95]

$$\frac{\Delta\lambda_{avg}}{\lambda_B} = K_z\varepsilon_z + K_h\frac{\left(\varepsilon_x+\varepsilon_y\right)}{2} + K_T\Delta T, \quad (2.9)$$

$$\frac{\Delta\lambda_{diff}}{\lambda_B} = K_S\left(\varepsilon_x-\varepsilon_y\right), \quad (2.10)$$

where $\Delta\lambda_{avg}$ is the average wavelength change, $\Delta\lambda_{diff}$ is the differential wavelength resulting from birefringence and K_z, K_h, K_T, and K_S can be found experimentally and are defined by

$$K_z = \left(1-\frac{n_{eff}^2}{2}p_{12}\right) + \frac{n_{eff}^2}{2}\left(p_{11}+p_{12}\right)\frac{C_m - C}{2G_m + \frac{C}{\nu}}, \quad (2.11)$$

$$K_T = \left(\frac{n_{eff}^2}{2}(p_{11} + 2p_{12})\alpha^2 + \frac{1}{n_{eff}}\frac{dn_{eff}}{dT} \right) + \frac{n_{eff}^2}{2}(p_{11} + p_{12}) \frac{\frac{C_m}{\nu_m}(\nu + 1)\alpha_m - \frac{C}{\nu}(\nu + 1)\alpha}{2G_m + \frac{C}{\nu}}, \quad (2.12)$$

$$K_S = \frac{n_{eff}^2}{2}(p_{12} - p_{11}) \frac{4G_m(1 - \nu_m)}{G_m + (3 - 4\nu_m)G}, \quad (2.13)$$

where G is a shear modulus, C is a Lame's constant, ν is a Poisson's ratio, α is a coefficient of thermal expansion of the material, G_m, C_m, ν_m, and α_m are the same constants for a host material [Li01], [Lop02].

2.3 Application examples of the FBG sensors

At present, FBG sensors occupy a significant place on the world sensor market. Large-scale structure monitoring and investigation of new or complex materials are two main application fields, where FBG sensors are used extensively at present. Especially, FBG sensor networks are crucial in health monitoring of some specifically structured or susceptible composite materials where it is not possible to use other sensor types. FBG sensor schemes existing at present can be divided into three groups:

- *point (localised)*, in which information of a particular measurand is obtained at a particular location;
- *distributed*, in which information of the measurand can be determined along the length of the fibre itself;
- *quasi-distributed (multiplexed)*, in which information of the measurand is obtained at specific pre-determined points along the length of a fibre network [Mer96], [Gra00].

Some attempts of commercial types of localised FOSs maintaining one or few FBGs were successfully realised [AOS], [Gei99], [Tel], [Slo98]. One of them is, for example, Ω-shape sensor maintaining two gratings with application in the monitoring of bridges [Slo01]. Two gratings with PVC protecting coating are glued with epoxy on the surface of the Ω-shape steel construction [Kli96], [Schl99] (see *Figure 2.10a*). This sensor allows strain measurement with a sensitivity of approximately 1.24 pm/με after fabrication. Its operation rate lies between -3000 and 1000 microstrain [Schl99]. Another example could be strain-pressure steel sensor rod using fibre with FBG prestrained and fixed inside the steel tube [Tel], [Gei99], [AOS], [Schl99], [Glö99], [Voe99] (see *Figure 2.10b*). It is possible to measure strain up to 10 000 microstrain with a resolution of approximately 3 microstrain. There are also sensors for temperature measurement maintaining one FBG fixed on the quartz-substrate [Boss01], mechanically stabilised temperature sensors using one FBG glued inside a quartz capillary with siloxane glue [Teu00], and a thermal compensating sensor, which use optimised FBGs for the sensor network fixed in the quartz-borosilcate glass housing [Bar01].

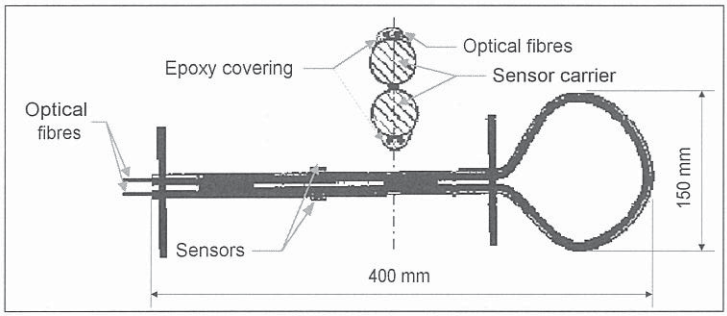

Figure 2.10a: Commercial localised FBG sensor types maintaining one or few FBGs: a) Ω–shape sensor (After: [Schl99]).

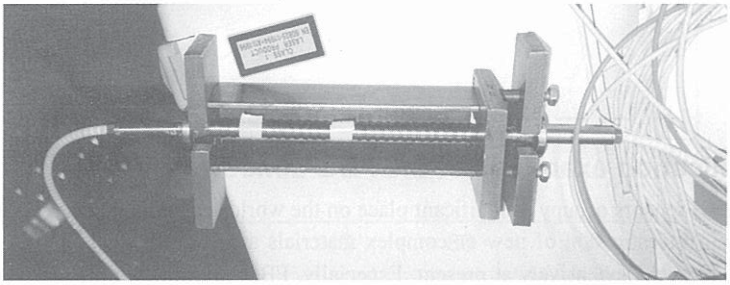

Figure 2.10b: Commercial localised FBG sensor types maintaining one or few FBGs: a strain-pressure sensor rod of Telegärtner Gerätebau GmbH (Lab. S.12, BAM).

There are also many different non-commercial FBG sensor designs, which have also found wide-spread industrial applications [Hoc79], [More89], [Kim92], [Mea92], [Stef94], [Law95], [Kli96], [Jin97], [Bha97], [Mag97], [Lo97], [Vri98], [Hab98], [Dew98], [Fuh98], [Hua98], [Voh98], [Ber00], [Jen00], [McK00], [Lau01], [Tru01], [Gue02]. Usually, for reliable application or embedment of FBG sensor or FBG sensor system it is better to fabricate or buy commercially available FBGs with precisely estimated characteristics and implement them into a sensor design. It helps to avoid further errors, which could be decisive for the sensor operation. Examples of the sensor design manufactured in laboratory could be strain-independent temperature measurement with two gratings laminated between two 20 µm thick polyimide sheets (see *Figure 2.11a*) or temperature-insensitive strain measurement with double-gratings sensor (see *Figure 2.11b*) [Har98], [Bet01], [Spi01].

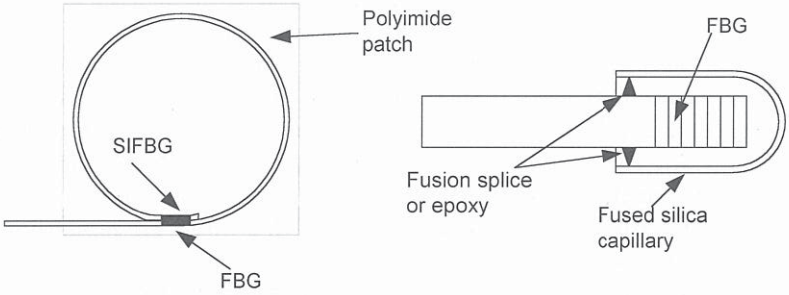

Figure 2.11a: Non-commercial localised sensor types: strain-isolated fibre Bragg grating (SIFBG) and an optical fibre sensor patch (After: [Har98]).

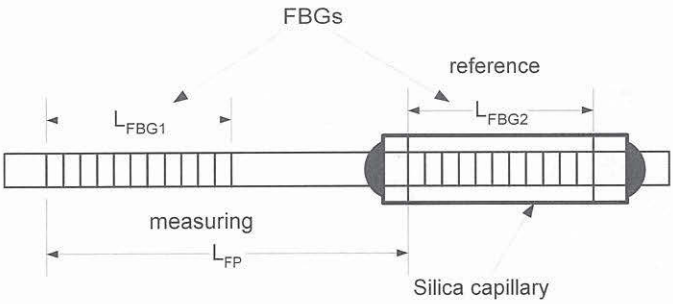

Figure 2.11b: Non-commercial localised sensor types: double Bragg grating strain sensor configuration for a temperature insensitive strain measurement (After: [Spi01]).

Bragg gratings fabricated for sensor application have a reflectivity less than 90 % and a narrow band wavelength reflection, which make possible also serial, parallel, or branching multiplexing of such sensing elements depending on the intended application. Therefore, FBGs can be implemented in any architecture of fibre optic network, allowing distributed or quasi-distributed sensing [Ala93], [Sir98], [Oth99], [Jen00], [Cul00] [McK00], [Ten00], [Lop02]. The following division-multiplexing techniques have been reported:

- *time* (TDM) exploits the ability to separate in time the response from one sensor separated from another by a length of optical fibre [Weis94], [Wils01];
- *spatial* (SDM) uses switching between different channels, each of which can contain one or more other multiplexing techniques [Kall95];
- *wavelength* (WDM) uses series of FBGs separated in the spectrum [Oth99];
- *frequency* (FDM) uses sources which power slightly unbalanced sensor interferometers and the sensor outputs carried only one signal from each of the source lasers [Dav95];
- *coherence* (CDM) uses pairs of gratings with different spacing along the fibre line and interrogates their reflections using a scanning Michelson interferometer to separate their returns in the coherence domain [Dak97].

Most extensively applied multiplexing techniques are TDM, WDM, and SDM as also their combinations [Rao96], [Cha99], [Cha01]. The combination of TDM and WDM techniques can allow multiplexing of larger number of sensors and sensor arrays by re-using the spectrum of the source. Several serial FBG arrays could be applied on the greater distance one after another in the serial scheme, which allow also TDM techniques to be used. A 10×10 system could be possible with such a multiplexing technique but problems can arise due to multiple reflections of overlapping wavelength FBGs separated in time, which could experience cross-talk through such "spectral shadowing" [Gra00]. Parallel and branching networks will eliminate this problem.

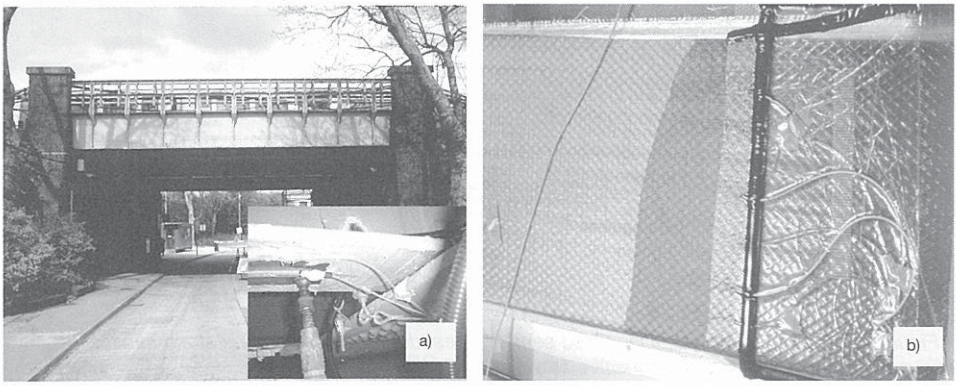

Figure 2.12: Point-sensing sensor types maintaining one or several FBGs: a) two sensor array installed in Acton Town Bridge (After: [Wei00]); b) branching FBGs network for cure monitoring of composite materials (Lab. S.12, BAM).

One of examples can be health monitoring with distributed FBG sensors network designed for space applications [Lat01]. *Figure 2.12a* presents two-sensor array applied for bridge monitoring by Damage Tolerance Group of Cranfield University [Wei00]. Branching quasi-distributed measurement with FBG arrays embedded into the FRC material are shown in *Figure 2.12b* [Lebi02]. Beside the architectures mentioned, there are also more complex networks composed on basic networks implemented.

2.4 Signal recording methods

The development and wide application of Bragg gratings give rise to a need for new interrogation techniques suitable for the recording of the signal provided with this structure. Response from the Bragg grating gives a spectrum of approximately Gaussian shape. The centre of such shape gives the central wavelength of the grating, which characterises the FBG. Measured parameters such as temperature, strain, or displacement induce changes in the grating spectrum. Interrogation schemes have to register changes in spectral response from FBG sensor or sensor networks. Measurement techniques used in the various applications depend on the measurement purpose and possibility [Mea92], [Ala93], [Weis94], [Vol96], [Dak97], [Mas97], [Fer99], [Oth99], [Fla99], [LeBl00], [Fuh00], [Wils01], [Tod01], [Weis01], [Zha02], [Baa02], [Lop02]. In sensor applications, primarily a broadband source (BBS) and an optical spectrum analyser (OSA) for spectral measurements are used [Mea98], [Chan99], [Cha00]. Interrogation technique applied for FBG signal recording has to convert FBG signal modulations into an appropriate optical intensity modulation and later into an electrical signal. Therefore, present research and development in the area of measurement concepts are directed to perform such transformations.

For strain or temperature measurement, wavelength resolution of such interrogation schemes have to achieve 1 pm to resolve a temperature change of 0.1 K and strain change 1 με and assure high quality measurement at initial grating wavelength 1300 nm [Oth99]. This places high demands for precise measurement of the Bragg wavelength shift of the FBG. The conventional case of passive broadband

interrogation technique from single FBG is shown in *Figure 2.13*. In such sensor schemes, simple source-detector technology is applied, where a variety of possibilities at present time exists [Lop02]. The FBG sensor is illuminated with BBS or tunable laser (TL), which cover the extent over which the sensor will operate under influence of the applied perturbations. The narrowband reflected light is directed to the detection system. There are various ways to differentiate any change in the reflected wavelength, such as basic spectrometer, passive or active optical filtering, and interferometric detection.

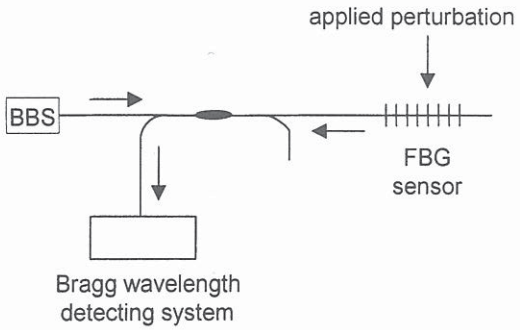

Figure 2.13: Example of the simple signal demodulation scheme from the localised sensor (After: [Gra00]).

Varieties of demodulation techniques have been presented in recent years. Interrogation techniques which find wide application at present, are given in *Table 2.1*.

Table 2.1: FBGs interrogation technique [Oth99].

	Edge filter	Tunable filter	Interferometric	Tunable laser	CCD-spectrometer
Range to resolution	10^2 - 10^3	10^3 - 10^4	10^3 - 10^4	10^3 - 10^5	10^3 - 10^4
Measurement speed	high	high	high	high	high
Long-term stability	good	good	good	good	good
WDM compatibility	low	high	high	high	high
Potential cost	low	medium	low	high	medium

Table 2.1 first shows example of a passive broadband interrogation (an edge filter), which was the first commercially available technique for the FBG signal recording. Edge filter provides a wavelength-dependent loss when the cutoff is close to the signal wavelength presenting a linear relationship between the wavelength shifts and the output intensity changes of the filter [Oth99]. Comparison of light transmitted through the filter with light passed along a reference path gives the wavelength shift of the FBG sensor. The measurement range is inversely proportional to the detection resolution. A low resolution of a few tens of με was demonstrated over a range of several mε [Mea92]. This approach is low cost and simple in handling but provides a limited range and requires filter stabilisation.

An example of interferometric interrogation technique is unbalanced optical fibre Mach-Zehnder interferometer (MZI). A sensitivity of 0.1 pm is possible with MZI. In addition, MZI can be applied for strain and temperature measurement. Reported strain response of the FBG (1550 nm) is 1.2 nm/mε [Mar92], [Ker92]. This interrogation technique requires referencing FBG or other methods for thermal drift compensation in the interferometer.

Scanning optical filters involve such devices as the tunable Fabry-Pérot filter (FPF), acousto-optic tunable filter (AOTF), and Bragg grating-based filter [Var96], [Rao96], [Hen], [Dye99], [LeBl00], [Xie02]. The demodulated output results from the tunable filter spectrum and the grating spectrum. It is optimised when the spectra match each other. Measured resolution of those devices is strongly dependent on the signal-to-noise ratio of the return signal and the line-widths of the tunable filter and the sensor. Strong gratings and sources have to be used to obtain the good wavelength resolution. In addition, measurements with low reflectivity gratings (2 %) and erbium sources (average powers of 10 mW) have demonstrated 1-με resolution. Such resolution together with the large effective range is sufficient for most structural monitoring applications [Weis94], [Mer96]. An example of filter interrogation which found wide telecommunication and sensor application is FPF. Tuning with FPF is achieved by accurate displacement of the mirror separation using a piezoelectric (PZ) element and, thereby, changing the cavity spacing. At present, it is possible to scan rates close to 1 kHz with FPF. In the scheme where only one FBG is applied, light from a broadband source illuminates the system; a narrowband signal is reflected from the FBG and directed to the FPF through the coupler. Filter bandwidth is comparable to the FBG bandwidth, whereas the free spectral range (FSR) is larger than the operating range of the grating. Resolution of approximately 0.1 pm over the working range of 40 nm could be achieved with FP filtering [Dav95], [Ros00]. FPF, operating in the wavelength-scanning mode, can be used to address several FBGs. The spacing between FBGs has to be between 2 and 4 nm, which limits the maximum number of gratings to 20 within a bandwidth of the typical BBS source 40 nm. This technique requires filter stabilisation. At present up to 60 FBGs can be measured with such an interrogation technique [Dav96b].

Another element of measurement technique, which has found wide application and ensures interrogation of any configuration of the fibre optic sensor with one FBG or an FBGs-array is calibrated narrow-linewidth single-frequency continuously wavelength-tunable erbium laser [Oth99]. The main advantage of this technique is improved signal-to-noise ratio, because the system determines the maximum in reflected power. Operating range reported by Ball *et al.* was 2.3 nm [Bal94]. Coroy *et al.* reported improved operating range 8 nm, and Maeda *et al.* achieved 38 nm [Mae99]. At present tunable lasers covering 100 nm spectrum with wavelength resolution better than 1 pm are available without use of tunable FP filter technique (ANDO Inc.).

A charge-coupled device (CCD) spectrometer overcomes limitations to the tuning range and the system bandwidth by parallel detection of the entire recovered-light spectrum [Ezb96], [Ezb97]. The CCD-spectrometer collects all the light reflected from each FBG over the entire scan period. It uses the bulk diffraction gratings, which direct the incident light across a linear array of detector pixels. Its resolution is typically 0.1 nm, but when the bandwidth of the measured wave exceeds one pixel the use of some processing techniques can result in improved wavelength resolution. A resolution of approximately 1 pm can easily be achieved when using a spectrometer with a 0.1 nm pixel resolution [Ezb98]. Strain sensitivities are better than 1 με using this approach. The advantage of this technology is that CCD spectrometer in contrast to the passive optical filters is stable towards environmental fluctuations.

Requirement for high-resolution measurement in laboratory conditions could be met with commercially available conventional systems. Usually, an optical spectrum analyser (OSA) together with tunable laser (TL), or broadband source (BBS), or, in some cases, swept diode laser (SDL), are used in the simple interrogation technique because of their high resolution, simplicity in handling, long term stability as well as possibility of quality analysis of any sensor network [Mec97], [Mori99], [Mae99], [Ros00]. Nevertheless, this technique cannot be considered as a practical solution for FBG signal demodulation due to their size and lack of robustness. Often, it is easier and more practical to use smaller and cheaper devices especially for field measurements, where large measurement equipment could be unsuitable or even impossible to use.

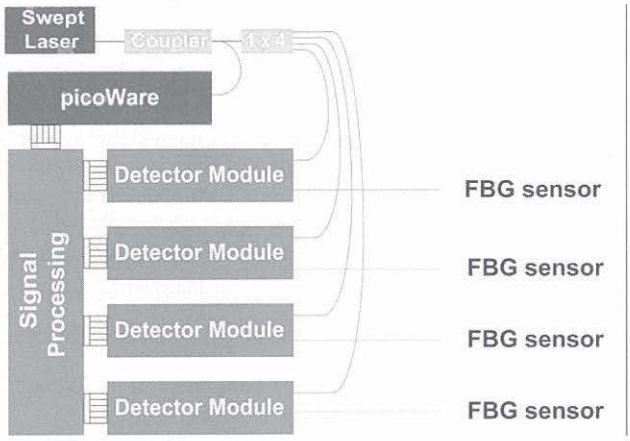

Figure 2.14: Swept laser interrogation scheme (After: Micron Optics Inc.).

One of the simple and practical solutions applied at present for field measurements is a swept laser interrogation (SLI) unit (Micron Optics Inc.). The FBG-SLI is a high-power, fast, multi-sensor measurement system. *Figure 2.14* shows this interrogation technique. The advantages of this technique include resolution better than 1 pm, operating range 40.95 nm, accuracy better than 0.005 nm under most conditions of operation, and possibility to demodulate signal from up to 64 FBGs in one fibre. Four channels and the powerful swept-laser source allow monitoring up to 256 sensors, which are scanned simultaneously at 108 Hz. The FBG-SLI unit found application for measuring strain, temperature, and pressure from dozens of sensors in a single fibre [MOI].

2.5 Technological problems

Problems resulting from the process of manufacturing and appearing at installation and operation of the FBG sensors can be divided into following groups:

reading of the sensor information obtained from measurand of interest besides of undesirable and unavoidable influences of medium such as vibrations, transverse or

unsteady strains, microbending, as well as residual stress after thermal or mechanical shocks;

- calibration of embedded sensors after an embedment procedure;
- reliability of FBG's coating:
    - acrylate coating, which has much smaller Young's modulus than the fibre core, can lead to creep effects and has influence on transmitted-reflected signal of FBG, for example in concrete, some composites, and metals;
    - polyimide coating dissolves under the influence of water, which prevents its application in the cases where water/moisture influence is unavoidable;
- packaging of FBG;
- embedding technique:
    - survival of FBG sensor in harsh environment or aggressive media such as cementitious materials;
    - reduction of perturbing influences such as microbending, micro-cracks, local indentation, or other micro effects arising during curing or in harsh environment or aggressive media such as cementitious materials;
    - influences of the measured matrix and environment at the operational stage;
    - optical stability e.g. for significant attenuation of the signal in the result of large transverse loads.
- demodulation technique:
    - stability of the Bragg wavelength under undesirable mechanical effects to avoid overlapping of neighbouring spectra in distributed sensor networks;
    - insufficient output power from light source to read the signal from FBG e.g. under large values of transverse load, where significant attenuation occurs;
    - insufficient bandwidth to cover bandwidth of FBG array;
    - insufficient resolution to fix narrow bandwidth of FBG;
    - high quality demodulation technique is too expensive for wide application.

It is important to define selection criteria to pick out unreliable and/or pre-damaged sensing elements before their integration into the sensor design. For example, in embedded FBG arrays, if one FBG suffers from significant spectral modulation it could lead to the failure of whole array, where repair is not possible.

3 Theoretical investigations of FBG signal changes due to perturbing influences

The sensor application requires flexibility in achieving desired spectral characteristics of the fibre-optic sensing element to ensure precision and stability in operation of the sensor. The FBG offers such flexibility [Erd97], [Bob97b], [Oth99], [Tru99a]. At present, it is possible to create FBGs with defined profile to achieve higher or lower reflectivity, broader or narrower bandwidth, steeper or sloping cutoff of the spectrum, and longer or shorter grating length. It is important to estimate FBG parameters before their application in the sensor scheme, which requires a well-developed theoretical approach for FBG design and understanding. This chapter considers some approaches applied for the analysis of FBG spectral characteristics under uniform conditions, and in the case of various influences, such as temperature, transverse stress or bending.

3.1 Analysis of the unperturbed and uniform FBG spectrum

For the propagation of electromagnetic radiation in the uniform and unperturbed FBG inscribed into the fibre core, it is important to create an analytical model in such a medium to study characteristics of the FBG. Traditional models of light propagation are rather inconvenient for the FBG analysis. It is possible to use Maxwell's equations for modelling light propagation in some periodical structures, but for fibres with circular cross-section, the equations are complex and include Bessel functions. Even if a precise solution is possible in this case, the physical content of phenomena is complicated with the need to solve characteristic equations. Snyder defined a range of intrinsic properties for Maxwell equations which complicate the solution, and elaborated a simple, approximate model of light propagation in the single mode fibre which allows calculation of fields, propagation constants, and other parameters necessary for description of the propagating mode along the optical fibre with a step-profile refractive index [Sny81a], [Sny81b]. More detail is given in Attachment A.

The theory of light propagation through periodical structures called coupled mode theory, which found wide application for the evaluation of FBGs, is a variety of perturbation theory and is elaborated sufficiently at the present time [Col73], [Ung80], [Lov84], [Yar84], [Mär95], [Erd97], [Hil97], [Bob97b], [Kas99], [Oth99]. Coupled mode theory is particularly useful when a slight perturbation has a large effect on the modal power distribution. The FBG-induced refractive index change Δn in the fibre core is noticeably smaller than the refractive index n_{co}. Therefore, the FBG can be considered as small perturbations which vary arbitrarily along a fibre core and cause a coupling and power exchange between the incident and reflected modes [Yar84]. The coupled mode theory for uniform FBG is described in Attachment B.

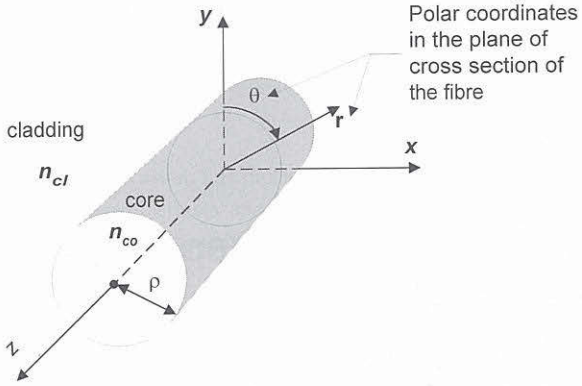

Figure 3.1: Schematic representation of the considered medium.

The general analysis considers a step-index single mode fibre, which consists of the core and the cladding - its geometry is taken to be cylindrical and axially symmetric (see *Figure 3.1*). The core and the cladding of the optical fibre have identical mechanical and photo-elastic properties but different refractive indices n_{co} and n_{cl}, where $n_{co} > n_{cl}$. The assumptions are valid for standard telecom single mode fibre. *Figure 3.1* shows a section of the optical fibre core with radius ρ and uniform refractive index n_{co} along the axis z.

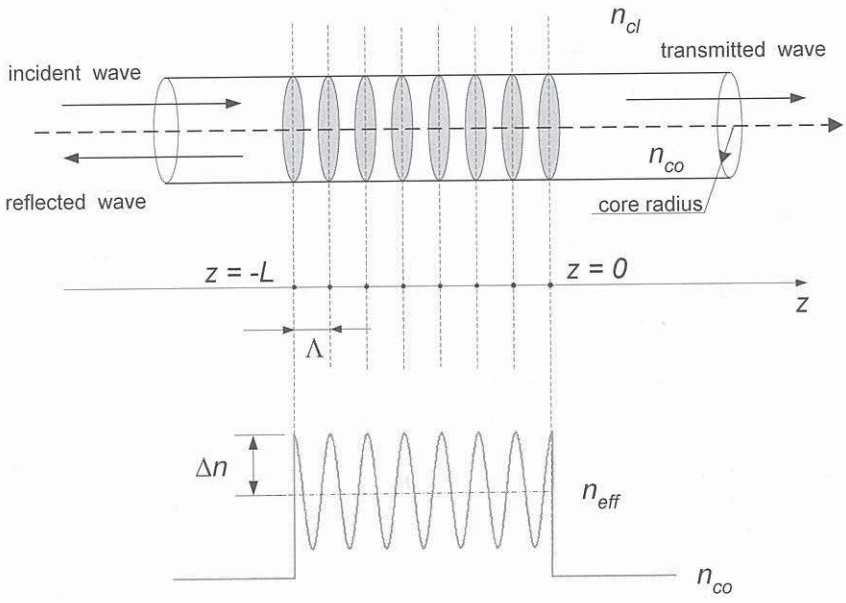

Figure 3.2: Schematically represented uniform FBG.

The UV-induced refractive index perturbation called an intra-core periodical structure, namely the

FBG, is shown in *Figure 3.2*. The effective refractive index $n_{eff}(z)$ of the fibre core with FBG is given by

$$n_{eff}(z) = n_{co} + \Delta n(z)\cdot\left[1 + m\cdot\cos\frac{2\pi}{\Lambda}z\right] = n_{co} + \Delta n(z)\cdot\left[1 + \frac{m}{2}\cdot\left(e^{j\frac{2\pi}{\Lambda}z} + e^{-j\frac{2\pi}{\Lambda}z}\right)\right], \tag{3.1}$$

where parameter m is a contrast determined by the visibility of the UV fringe pattern, $\Delta n(z)$ is the FBG-induced refractive index change along the axis z which essentially determines the optical properties of the resulting gratings.

3.1.1 Calculation of the FBG reflection spectrum

For a weakly guided fibre, when $n_{co} \cong n_{cl}$, polarisation effects can be ignored. Only x -polarisation of the field is considered. The strongest interaction between modes in the fibre core occurs at the Bragg wavelength determined as

$$\lambda_B = 2n_{eff}\Lambda, \tag{3.2}$$

where n_{eff} is an effective refractive index along the grating length.

Since a uniform FBG is examined, where coupling occurs between modes propagating in opposite directions, a simple solution for transmission and reflection could be obtained. An incident wave $A_1(z)\psi(r)e^{-j\beta z}$ and a reflected wave $A_2(z)\psi(r)e^{j\beta z}$ are considered, where $A_1(z)$ is the incident wave amplitude, $A_2(z)$ is the reflected wave amplitude, β is propagation constant and $\psi(r)$ is a scalar wave function. The system of equations for amplitudes of propagating and reflected modes is given by

$$\begin{aligned}\frac{d}{dz}A_1 &= -j\kappa A_2 e^{j\cdot\Delta\beta\cdot z},\\ \frac{d}{dz}A_2 &= j\kappa^* A_1 e^{-j\cdot\Delta\beta\cdot z},\end{aligned} \tag{3.3}$$

where $\Delta\beta = 2\beta - \frac{2\pi}{\Lambda}$ is a change of the propagation constant, and $\kappa = \frac{\pi}{\beta}\int_0^\infty r\psi^2(r)k_0{}^2(r)m(r)dr$ is a coupling coefficient, where $k_0(r)$ is a wave number and $m(r)$ is a contrast of the pattern. Solution of this system is found at boundary conditions: $A_2(L)=0$ and $A_1(0)=1$ and is given in Attachment B. Definition of the propagating and reflected waves amplitudes makes it possible to find the FBG reflectivity, which is given by

$$R = \left|\frac{A_2(0)}{A_1(0)}\right|^2 \tag{3.4}$$

[Yar84]. Substitution of the solutions for the propagated and reflected modes into (3.4) gives equations for calculation of the FBG reflectivity

$$R = \frac{\kappa^* \kappa \sinh^2[s \cdot (L-z)]}{s^2 \cdot \cosh^2[s \cdot (L-z)] + \left(\frac{\Delta\beta}{2}\right)^2 \cdot \sinh^2[s \cdot (L-z)]}, \text{ at } s^2 > 0,$$

$$R = \frac{\kappa^* \kappa \sin^2[s \cdot (L-z)]}{-s^2 \cdot \cos^2[s \cdot (L-z)] + \left(\frac{\Delta\beta}{2}\right)^2 \cdot \sin^2[s \cdot (L-z)]}, \text{ at } s^2 < 0, \tag{3.5}$$

where $s \neq 0$ and $s^2 = \kappa^* \kappa - \left(\frac{\Delta\beta}{2}\right)^2$. Maximum reflectivity occurs at $\Delta\beta = 0$, where $R_{\max} = \tanh^2|\kappa|L$. The reflection spectrum, to be exact the dependence of the reflectivity on the propagated wavelength, is characterised by a clear maximum and series of sidelobes. Sideband changes depending on the FBG length, period, and refractive index change.

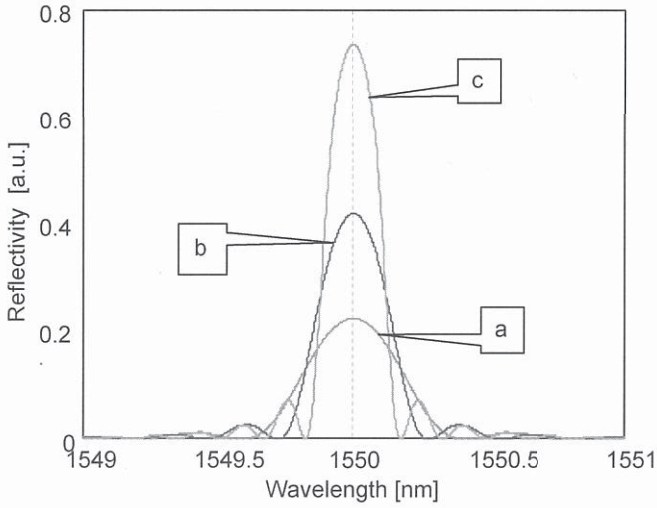

Figure 3.3: Reflectivity of different FBG lengths: a) 2 mm; b) 3 mm; c) 5 mm.

Figure 3.3 shows the FBG reflectivity of three gratings with different lengths. The refractive index for germanosilicate fibre is taken as 1.482, the refractive index modulation as $\Delta n = 10^{-4}$, and the period of the gratings as $\Lambda = 0.523$ µm. *Figure 3.3* shows maximal reflectivity for the longest FBG $L = 5$ mm. In this case, if the number of grating planes $N = \frac{L}{\Lambda}$ is larger (or smaller), the reflection bandwidth of the uniform FBG will be broader (or narrower) respectively, for a given value of the FBG length L.

3.1.2 Wave propagation in quasi-periodical medium

Results obtained in the previous subsection have shown that selection of the defined grating length makes it possible to obtain the FBG with larger reflectivity or narrower bandwidth. Now the definition of the FBG amplitude with a purpose to avoid high sideband of the FBG spectrum is considered.

The dielectric permittivity changes along the axis z in endless dielectric medium according to the equation:

$$\varepsilon(x,y,z)=\begin{cases}\varepsilon_a, & -\infty < z < -L \text{ and } 0 < z < \infty \\ \varepsilon_a + \varepsilon_1(z)\cos\left(\dfrac{2\pi}{\lambda}z\right), & -L \le z \le 0\end{cases}, \tag{3.6}$$

where ε_a is a permittivity constant, Λ is a period of permittivity modulations, $\varepsilon_1(z)$ is an amplitude of the variable component of the permittivity, where $\max|\varepsilon_1(z)| << \varepsilon_a$.

Changes of amplitudes $A_1(z)$ and $A_2(z)$ within the grating length L are described by the system of two first order differential equations (3.3). Planes of the uniform FBG are orthogonal to the axis z (see *Figure 3.2*). The coupling coefficient κ for this case appears from the equation:

$$\kappa = \frac{\pi}{\beta}\int_0^{\infty} r\psi^2(r)k^2 m(r)dr, \tag{3.7}$$

where k is a wave number, $n_{co} = \sqrt{\varepsilon_a}$. At the constant value of κ, the system of equations (3.3) has an analytical solution. The following expression is obtained by the z-axis differentiation of the amplitude reflection coefficient

$$\frac{d\rho(z)}{dz} = \frac{A_1\dfrac{dA_2}{dz} - A_2\dfrac{dA_1}{dz}}{{A_1}^2}. \tag{3.8}$$

The amplitude reflection coefficient $\rho(z)$ changes within the segment $-L < z < 0$ and depends on the z-axis, equals zero for $z > 0$, and has a constant value at $z < -L$ (see *Figure 3.2*). Substitution of the system (3.3) in equation (3.8) may be expressed as

$$\frac{d\rho(z)}{dz} = j\kappa\left(e^{-j\Delta\beta\cdot z} + \rho(z)^2 e^{j\Delta\beta\cdot z}\right). \tag{3.9}$$

The analytical solution could be found at $\Delta\beta = 0$ and initial conditions $\rho(0) = 0$, $A_2(0) = 0$, and $A_1(0) = 1$:

$$\rho(z) = j\tanh\left[\int_0^z \kappa(z)dz\right]. \tag{3.10}$$

This equation at the grating edge $z = -L$ is expressed as

$$\rho(-L) = j\tanh\left[\int_0^{-L} \kappa(z)dz\right]. \tag{3.11}$$

From the equation (3.11) it follows that the amplitude reflection coefficient is determined only by functions $\int_0^{-L}\kappa(z)dz$ and $|\rho(z)|<1$ at $\Delta\beta=0$ and $z=-L$. If $\left|\int_0^{-L}\kappa(z)dz\right|$ is small, then $|\rho(z)|<<1$ and equation (3.9) transfers into

$$\frac{d\rho(z)}{dz}\cong j\kappa(z)e^{-j\Delta\beta\cdot z}. \tag{3.12}$$

Therefore,

$$\rho(\Delta\beta,-L)=-j\int_{-\infty}^{\infty}\kappa(z)e^{-j\Delta\beta\cdot z}dz. \tag{3.13}$$

Hence, the amplitude reflection coefficient $\rho(\Delta\beta,-L)$ is related to $\kappa(z)$ by Fourier transform. For example, a frequency response for the filters on surface acoustic waves is also equal to the Fourier image of the electrode weight function [Kay90]. Necessary frequency characteristic of such filters is obtained by electrodes apodization, which corresponds to the present case of the function $\kappa(z)$ definition. The present task has a solution only if $|\rho(z)|<<1$.

Solution of the differential equations system

Since amplitudes of incident $A_1(z)$ and reflected $A_2(z)$ modes have real and imaginary parts, they may be expressed as

$$\begin{aligned}A_1(z)&=A_{11}(z)+jA_{12}(z),\\ A_2(z)&=A_{21}(z)+jA_{22}(z).\end{aligned} \tag{3.14}$$

After substitution of (3.14) into (3.3) and after the selection of real and imaginary parts of the system, it appears as follows:

$$\begin{cases}\dfrac{dA_{11}}{dz}=\kappa(A_{21}\sin\Delta\beta z+A_{22}\cos\Delta\beta z)\\ \dfrac{dA_{12}}{dz}=-\kappa(A_{21}\cos\Delta\beta z-A_{22}\sin\Delta\beta z)\\ \dfrac{dA_{21}}{dz}=\kappa(A_{11}\sin\Delta\beta z-A_{12}\cos\Delta\beta z)\\ \dfrac{dA_{22}}{dz}=\kappa(A_{11}\cos\Delta\beta z+A_{12}\sin\Delta\beta z)\end{cases} \tag{3.15}$$

The system (3.15) could be solved by the Runge-Kutta method of the fourth order with initial conditions: $A_{11}(0)=1$, $A_{12}(0)=0$, $A_{21}(0)=0$, and $A_{22}(0)=1$ [Corn74]. The square of the amplitude reflection coefficient $\rho(-L)$ can be calculated, when A_{11}, A_{12}, A_{21}, and A_{22} are known:

$$|\rho(-L)|^2=\frac{A_{21}{}^2(-L)+A_{22}{}^2(-L)}{A_{11}{}^2(-L)+A_{12}{}^2(-L)}. \tag{3.16}$$

The following equation

$$M(-L)=A_{11}{}^2(-L)+A_{12}{}^2(-L)-A_{21}{}^2(-L)-A_{22}{}^2(-L) \tag{3.17}$$

is used for the model verification, where $M(-L)$ has to be stable and in this case, has to be of one. The step of integration is selected to satisfy the condition $|M(-L)-1|\leq 10^{-4}$ in the process of solution. System (3.15) is initially solved for the 10 mm long FBG at $\kappa = 250$ m^{-1}, $n_0 = 1.47$, and $\Lambda = 0.534013605$ μm. The reflectivity is found to be 0.973408 at the wavelength $\lambda = 1570$ nm ($\Delta\beta = 0$) according to (3.10). The same value is obtained according to equation (3.16). The step of integration is 0.1 mm.

The reflectivity R is shown in *Figure 3.4*. From *Figure 3.4* it follows that the grating reflectivity increases and the bandwidth broadens at the increase of the grating constant amplitude. The highest sideband of the reflection spectra is 22 % for $\kappa = 100$ m^{-1}. For the coupling coefficient of value 500 m^{-1} the sideband increases until 50 %.

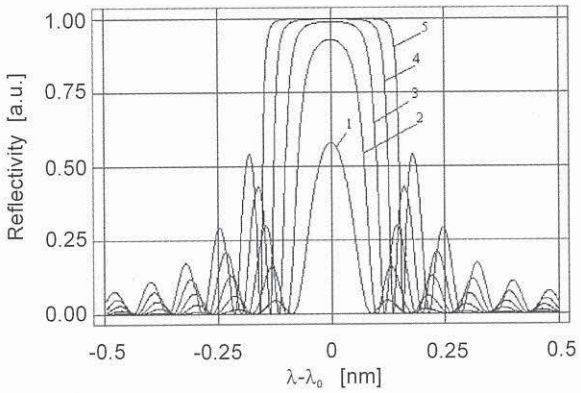

Figure 3.4: The reflectivity of the 10 mm long grating for the following values of the coupling coefficient κ : 1 - 100 m^{-1}, 2 – 200 m^{-1}, 3 - 300 m^{-1}, 4 - 400 m^{-1}, 5 - 500 m^{-1}.

The solution of the system (3.15) by the Runge-Kutta method of the fourth order for the different functions $\kappa(z)$ and for the condition that $\left|\int_0^{-L}\kappa(z)dz\right| = 2.5$, where $max\,\kappa(z) = 250$ m^{-1} is given by

$$\kappa_{1,n}(z)=\kappa_{0,n}\left[\left(\frac{L}{2}\right)^2-\left(z+\frac{L}{2}\right)^2\right]^n, \tag{3.18}$$

$$\kappa_2(z)=-\frac{1{,}25\pi}{L}\sin\frac{\pi z}{L}, \tag{3.19}$$

$$\kappa_3(z) = \frac{6}{L}\exp\left[-\frac{18\left(z+\frac{L}{2}\right)^2}{L^2}\right],$$

$$\kappa_4(z) = 0{,}837\,\frac{\sin\left[\frac{8\pi}{L}\left(z+\frac{L}{2}\right)\right]}{z+\frac{L}{2}}, \text{ and}$$

$$\kappa_5(z) = 595{,}24\left[0{,}42 + 0{,}5\cos\frac{2\pi}{L}\left(z+\frac{L}{2}\right) + 0{,}08\cos\frac{4\pi}{L}\left(z+\frac{L}{2}\right)\right],$$

where $n = 1, 2, 3, 4, 5$.

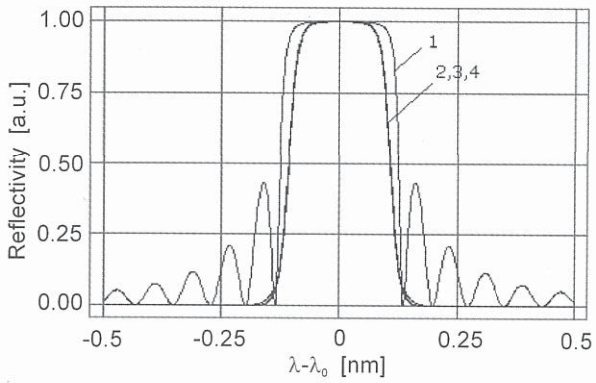

Figure 3.5: The grating reflectivity calculated for the following functions: 1 - $\kappa_{1,0}(z)$; 2 - $\kappa_3(z)$; 3 - $\kappa_5(z)$; 4 - $\kappa_{1,5}(z)$.

Reflectivity of different gratings calculated for the different functions $\kappa(z)$ for the conditions that $\left|\int_0^{-L}\kappa(z)dz\right| = 4$ and $max\,\kappa(z) = 400\ \mathrm{m}^{-1}$ are shown in *Figure 3.5*. The grating reflectivity R equals 0.9734 with the condition that $\Delta\beta = 0$ for all found functions. The grating amplitude apodization has a significant influence on the shape of the grating spectrum and practically eliminates a sideband. The bandwidth of the grating reflection spectrum broadens when the sideband is attenuated notably. Calculated values for the first five functions of coupling coefficients are shown in *Table 3.1*.

Table 3.1: Values of some coupling coefficients $\kappa_{0,n}$ (see equation (3.18).

The coupling coefficient $\kappa_{0,n}$	Obtained value
$\kappa_{0,1}$	$0.15 \cdot 10^{8}$ m^{-3}
$\kappa_{0,2}$	$0.75 \cdot 10^{12}$ m^{-5}
$\kappa_{0,3}$	$0.35 \cdot 10^{17}$ m^{-7}
$\kappa_{0,4}$	$0.15 \cdot 10^{22}$ m^{-9}
$\kappa_{0,5}$	$0.693 \cdot 10^{26}$ m^{-11}

It is not possible to realise large values of the coupling coefficient κ for all cases in practice. Therefore, calculations for some functions at different grating lengths are provided as examples. Grating lengths calculated for some functions of the coupling coefficient $\kappa_{m,n}(z)$ within the margins of the grating $-L \le z \le 0$ are given in *Table 3.2*. The step of integration is chosen for the condition $|M(-L)-1| \le 10^{-4}$.

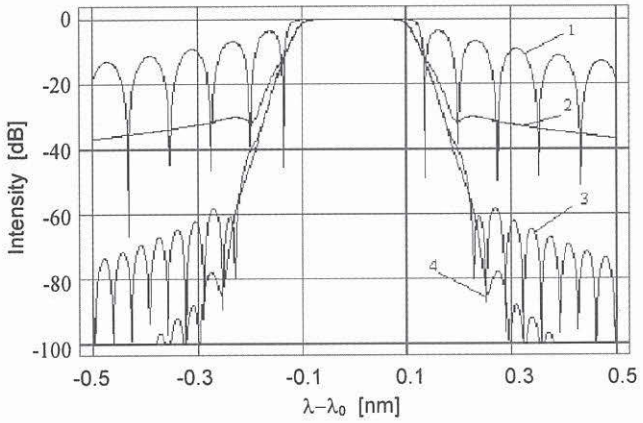

Figure 3.6: The grating reflectivity spectra for the following functions: 1 - $\kappa_{1,0}(z)$, 2 - $\kappa_3(z)$, 3 – $\kappa_5(z)$, 4 - $\kappa_{1,5}(z)$.

Figure 3.6 shows the grating apodization along functions $\kappa_{1,0}(z)$, $\kappa_3(z)$, $\kappa_5(z)$ and $\kappa_{1,5}(z)$ for the function type $\kappa_{1,n}(z) = \kappa_{0,n}\left[\left(\frac{L}{2}\right)^2 - \left(z+\frac{L}{2}\right)^2\right]^n$ with the condition that $max|\kappa(z)|$ =250 m^{-1}. Attenuation of the sideband increases with the increase of n. The best results are observed for the functions $\kappa_{1,4}(z)$, $\kappa_{1,5}(z)$ and $\kappa_5(z)$ (*Table 3.2*). Theoretically estimated attenuation of the sideband appears correspondingly: 60, 67 and 54 dBm. It is typical for those functions that their values and values of lowest derivatives on the grating edges equal zero. For the fifth function $\kappa_{1,5}(z)$, four lowest derivatives on the grating edges equal zero too.

Table 3.2 Calculated lengths of the FBG for defined coupling coefficient functions.

$\kappa_{m,n}(z)$	**Function, m^{-1}**	**Length of the FBG, m**
$\kappa_{1,3}(z)$	$1.460265\cdot10^{14}\left[\left(\frac{L}{2}\right)^2-\left(z+\frac{L}{2}\right)^2\right]^3$	$2.1875\cdot10^{-2}$
$\kappa_{1,4}(z)$	$0.475746\cdot10^{18}\left[\left(\frac{L}{2}\right)^2-\left(z+\frac{L}{2}\right)^2\right]^4$	$2.46093\cdot10^{-2}$
$\kappa_{1,5}(z)$	$0.121145\cdot10^{22}\left[\left(\frac{L}{2}\right)^2-\left(z+\frac{L}{2}\right)^2\right]^5$	$2.70703\cdot10^{-2}$
$\kappa_{1,6}(z)$	$0.253067\cdot10^{25}\left[\left(\frac{L}{2}\right)^2-\left(z+\frac{L}{2}\right)^2\right]^6$	$2.93262\cdot10^{-2}$
$\kappa_{1,10}(z)$	$1.132873\cdot10^{37}\left[\left(\frac{L}{2}\right)^2-\left(z+\frac{L}{2}\right)^2\right]^{10}$	$3.70097\cdot10^{-2}$
$\kappa_4(z)$	$250\frac{\sin\left[\frac{8\pi}{L}\left(z+\frac{L}{2}\right)\right]}{\frac{8\pi}{L}\left(z+\frac{L}{2}\right)}$	$8.42097\cdot10^{-2}$
$\kappa_5(z)$	$250\left[0.42+0.5\cos\left[\frac{2\pi}{L}\left(z+\frac{L}{2}\right)\right]+0.08\cos\left[\frac{4\pi}{L}\left(z+\frac{L}{2}\right)\right]\right]$	$2.381\cdot10^{-2}$

Figure 3.7 shows also the grating reflectivity for functions $\kappa_{1,1}(z)$, $\kappa_{1,3}(z)$, $\kappa_5(z)$ and $\kappa_{1,5}(z)$ for the condition that $\left|\int_0^{-L}\kappa(z)dz\right| = 4$.

The largest observed attenuation was received for the function $\kappa_{1,10}(z)$*. Values of this function and first *n-1* derivatives on the grating edges ($z = 0$ and $z = -L$) are equal to the zero.

* estimated of approximately 160 dBm.

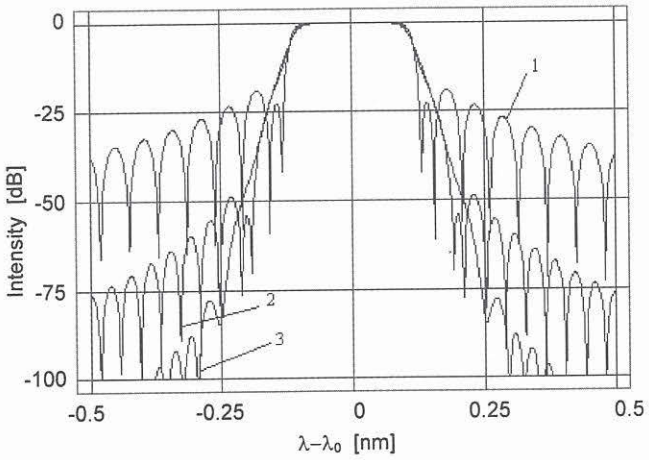

Figure 3.7: The grating reflectivity spectra for the following functions: 1 - $\kappa_{1,1}(z)$; 2 - $\kappa_{1,3}(z)$; 3 - $\kappa_{1,5}(z)$.

Calculations show that with formation of a well-defined quasi-periodical grating, the amplitude of the grating sideband could be decreased considerably and desired FBG reflection spectrum could be obtained. It is possible to realise the whole class of functions $\kappa(z)$ for the optical fibre but they have to correspond to condition $\kappa(z)>0$ and have to be limited by maximum refractive index modulations induced by the UV irradiation during the grating inscription. Quasi-periodical gratings described by functions $\kappa_{1,n}(z)=\kappa_{0,n}\left[\left(\frac{L}{2}\right)^2-\left(z+\frac{L}{2}\right)^2\right]^n$ could be achieved at $n<6$. For the practical purposes, this is sufficient.

3.2 Light propagation in FBG exposed to the external influences

Parameters of unperturbed FBG are described in section 3.1. There were assumed that light propagates through the single mode fibre, which is a uniform isotropic dielectric medium with a circular cross-section, and that the fundamental mode propagating along the axis z is linearly polarised. The FBG was not subjected to any influences, neither disturbances, nor measured signals.

Parameters of the FBG exposed to the measured values such as temperature, or exposed to the perturbation field of the surrounding medium such as bending or transverse stress, will now be considered.

3.2.1 Temperature influence

Calculation of an FBG response to strain or temperature influences was described in Chapter 2. Formulations used for the analysis of the FBG exposed to strain or temperature are shown in

subsection 2.1.2. In this subsection, FBG characteristics under temperature influence are calculated and the example of a simple sensor design for temperature measurement is considered.

Theoretical background

Temperature induced changes in FBG's spectrum are calculated on the basis of the coupled modes theory for a non-uniform medium [Sny79], [Yar89], [Lebi98], [Gaf00]. It is possible to calculate the FBG reflectivity and dependence of the reflectivity on temperature changes taking into consideration properties of the FBG, namely changes in the FBG's period and the fibre refractive index in the result of the temperature induced expansion or contraction of the material. *Figure 3.8* shows calculated shift of the FBG central wavelength induced by a temperature increase of 80 K.

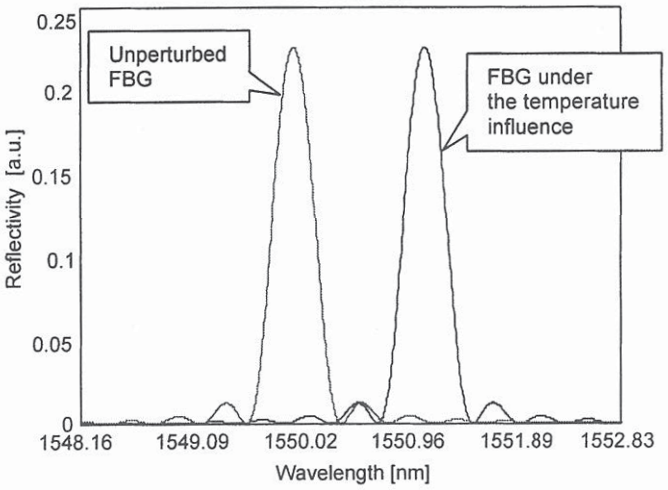

Figure 3.8: Reflectivity of the 2 mm long FBG (1550 nm).

The FBG is sensitive to temperature changes due to the temperature-dependent refractive index $n(T)$ of the fibre core and the grating period $\Lambda(T)$

$$\begin{aligned} n(T) &= n_{eff}\left[1+\alpha_n(T-T_0)\right] \\ \Lambda(T) &= \Lambda_0\left[1+\alpha(T-T_0)\right] \end{aligned}, \tag{3.20}$$

Where n_{eff} is an effective refractive index of the unperturbed grating, α_n (or $\frac{dn_{eff}}{dT}$) and α characterise the fibre material and α_n is a thermo-optic coefficient of the germanosilicate fibre (approximately $8.6 \times 10^{-6}\ K^{-1}$), α is a thermal expansion coefficient of the silica fibre (approximately $0.55 \times 10^{-6}\ K^{-1}$).

Example of a simple temperature sensor design

One of the main fields of current research is in sensor systems that can detect and quantify optical information from measured medium and translate this to the output signal. Special attention is paid to primary transducers, which are subjected to requirements such as immunity to electromagnetic interference or operability in highly contaminated or aggressive media. Fibre optic sensors belong to the separate class of long-term transducers which are able to assure reliable translation of the measured signal into an output signal.

A sensor scheme is proposed as example of temperature sensing consisting of a laser 1, an optical fibre 2, 4, detectors 5, 6, amplifiers 7, 8, and a signal-processing device 9 [Lebi98]. The FBG operates as a thermo-sensitive element of a localised sensor. The device is shown in *Figure 3.9*.

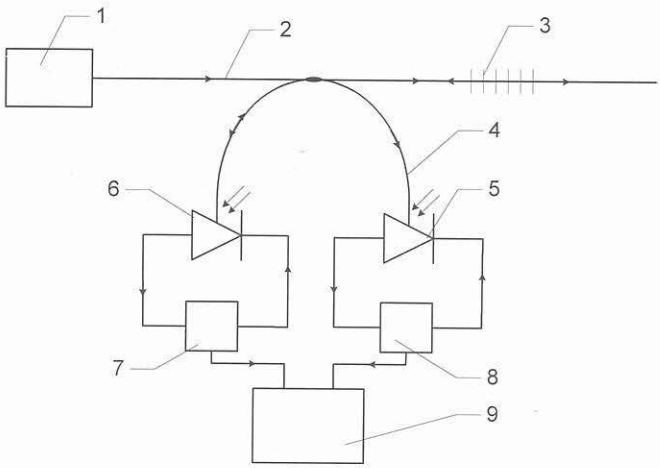

Figure 3.9: A proposed temperature sensing mechanism: 1 - laser, 2 - optical fibre, 3 – FBG, 4 - optical fibre, 5, 6 - detectors, 7,8 - amplifiers, and 9 - signal processing device.

The light is launched into the fibre 2 with the initial power P_0, and the power $P_1 = kP_0$, where k is a splitting ratio of the coupler and $k < 1$, reaches detector 5. The rest of the light with power $P_0(1-k)$ propagates along the fibre 2 until it reaches the FBG 3. After the reflection from the FBG with the coefficient $R(T)$, light propagates in the reverse direction with the power $R(T)(1-k)P_0$. The part of the reflected light with the same coefficient k appears in the fibre 4 and reaches detector 6 with the power $P_T = k(1-k)R(T)P_0$ (see *Figure 3.9*). Induced photocurrents

$$I(T) = S_f k(1-k)R(T)P_0 \text{ and}$$
$$I_1 = S_f kP_0, \tag{3.21}$$

where S_f is the proportionality factor or responsitivity of the photodetector, will be registered by a signal-processing device

$$\frac{I(T)}{I} = (1-k)R(T). \tag{3.22}$$

The results of measurement with such a simple sensor construction do not depend on the light source efficiency, but will require an FBG with a specific wavelength to make the scheme more cost effective.

Figure 3.10 shows the calculated output signal dependence on temperature at the wavelength of the laser source equal 1550 nm. The dependence has a parabolic shape with a clear maximum. It can be seen that the sensor presents linear operation within the range from 0 °C until 30 °C with the uncertainty of 0.01 °C. Lower boundary of the sensor operation range could be selected by changing the grating's period.

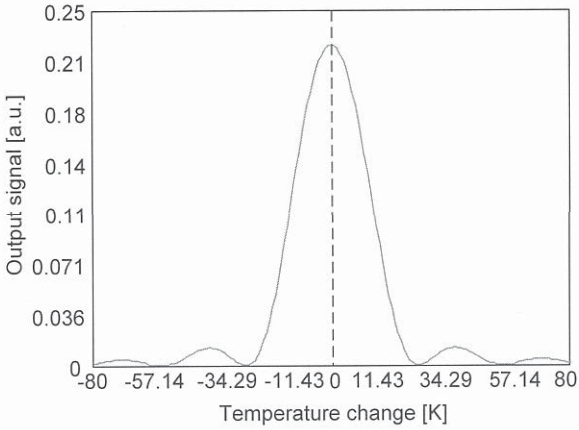

Figure 3.10: Calculated dependence of the output signal on the temperature change $R(\Delta T)$ for the 2 mm long FBG (1550 nm).

Modelling the FBG behaviour requires additional consideration of temperature-dependent properties of the materials used for gratings (fused silica, acrylate or polyimide coating) at low or high temperatures. The FBG wavelength changes at low temperatures will have non-linear character for some coating materials [Hab98], [Tru00a].

3.2.2 Analysis of the birefringence effect

If the FBG is subjected to a perturbation field such as a stress or low temperatures, its refractive index is altered; a phenomenon termed the photoelastic effect. In the case of transverse stress, a birefringence will be induced due to the stress distribution and geometrical modifications of the fibre core.

In the case of the FBG, birefringence induces bifurcation of the FBGs main reflection peak, which could be crucial in some sensor applications. Different approaches can be applied to define FBG characterisation parameters in this case: an approximation of fibre parameters with rectangular cross-section [Kum84], the perturbation model [Sny81b], or the coupled-mode theory for perturbed media

[Yar84], [Nod86]. According to these models, a birefringence of modes is expressed as a sum of two parts $B = B_G + B_S$, where B_G is a geometrical part related to the elliptical shape of the fibre core, and B_S is a stress part concerned to the residual stress in the optical fibre. Whereas the residual stress effect is often neglected, Martynkien *et al.* have found that it can reach 50 % of the total birefringence value [Mart99] which can be critical in our case. The approximation for rectangular cross-section is given in more detail in Attachment C. The square of the normalised propagation constant (P^2) is used in this approach to simplify calculations. For an elliptical fibre core this parameter is given by

$$P_x{}^{0^2} = \frac{\beta_x{}^2 - k_0{}^2 n_{cl}{}^2}{k_0{}^2\left(n_{co}{}^2 - n_{cl}{}^2\right)},$$
$$P_y{}^{0^2} = \frac{\beta_y{}^2 - k_0{}^2 n_{cl}{}^2}{k_0{}^2\left(n_{co}{}^2 - n_{cl}{}^2\right)}. \tag{3.23}$$

Two corrections are considered to define normalised propagation constants in elliptical-core fibre using values for rectangular-core fibre. Geometrical corrections $P_x{}^{G2}$ and $P_y{}^{G2}$ represent the difference in shape between a rectangle and an ellipse. After that, stress corrections for the normalised propagation constants $P_x{}^{S2}$ and $P_y{}^{S2}$ are considered. The general normalised propagation constant is given by:

$$P_i^2 = P_i^{0^2} + P_i^{G2} + P_i^{S2}, \tag{3.24}$$

where index i describes a polarisation axis. Knowing normalised propagation constant of modes, it is possible to calculate general birefringence of the fibre

$$B = \sqrt{P_x{}^2\left(n_{co}{}^2 - n_{cl}{}^2\right) + n_{cl}{}^2} - \sqrt{P_y{}^2\left(n_{co}{}^2 - n_{cl}{}^2\right) + n_{cl}{}^2} \tag{3.25}$$

and geometrical birefringence:

$$B_G = \sqrt{\left(P_x{}^{0^2} + P_x{}^{G^2}\right)\left(n_{co}{}^2 - n_{cl}{}^2\right) + n_{cl}{}^2} - \sqrt{\left(P_y{}^{0^2} + P_y{}^{G^2}\right)\left(n_{co}{}^2 - n_{cl}{}^2\right) + n_{cl}{}^2}. \tag{3.26}$$

General and geometrical parts of the birefringence allow estimation of the stress part of the birefringence, which is additionally temperature dependent. This approach allows the estimation of the birefringence and its components for elliptical cross-section fibres using approximation for rectangular cross-section fibres. For such a simple case as light propagation in a silica glass single mode fibre, where the geometrical difference between circular and elliptical cross-sections is very small, this approach introduces larger inexactitude as the perturbation theory applied for a field calculation in an elliptical-core fibre [Sny81b]. The approximation used for a single mode fibre in the perturbations theory leads to simplified equations making it possible also to understand the physical content of the model.

It is assumed that there are small changes in the fibre geometry, when a square of the circular fibre cross-section equals a square of the elliptical fibre cross-section and satisfies the correlation $\rho^2 = \rho_x \cdot \rho_y$, where ρ_x and ρ_y are the fibre radius changes along the x - and y - axes

respectively. The eccentricity is given by $e = \sqrt{1 - \frac{\rho_y^2}{\rho_x^2}} << 1$. *Figure 3.11* shows four shaded regions which are considered as perturbation zones. Assuming that the deformation is small, the perturbation zone is tiny. This makes it possible to approximate the scalar wave function in polar coordinates $\psi(r,\phi)$ by $\psi(\rho,\phi)$. Radial width of perturbed region can be defined as $\delta r = e^2 \frac{\rho}{4} \cos 2\phi$ by transfer of elliptical interface into polar coordinates. It is assumed that the radius of the single mode fibre is 4.1 μm and the deviation of the fibre core from the circular reaches maximum $\delta r = \pm 0.2$ μm.

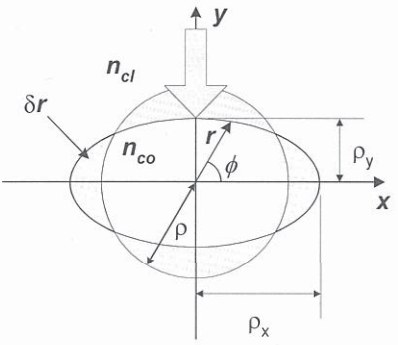

Figure 3.11: Representation of the fibre deformation.

Such assumptions allow the definition of the scalar propagation constant in the elliptical medium: $\beta = \overline{\beta} + \delta\beta$. The correction $\delta\beta$ consists of two parts for x- and y- polarisation axes $\delta\beta = \delta\beta_x - \delta\beta_y$ and is given by

$$\delta\beta = \frac{(2\Delta)^{3/2}}{4\pi V} \frac{\int_{s_e} \left\{ n_x \frac{\partial\psi}{\partial x} - n_y \frac{\partial\psi}{\partial y} \right\} \psi ds}{\int_0^\infty \psi^2 r dr}, \tag{3.27}$$

where s_e is the elliptical interface, $ds \cong \rho \left\{ 1 + \frac{1}{4} e^2 \cos(2\phi) \right\} d\phi$, V is a fibre parameter; for a single mode, weakly guided fibre it is given by $V = 1.65$, n_x and n_y are x- and y- components of the refractive index given by

$$\begin{aligned} n_x &= \left(1 - e^2 \sin^2\phi\right) \cos\phi, \\ n_y &= \left(1 - e^2 \cos^2\phi\right) \sin\phi, \end{aligned} \tag{3.28}$$

Then, the normalised birefringence of the optical fibre with elliptical cross-section is given by

$$B_p = \frac{\delta\beta\rho}{e^2\Delta^{3/2}}. \tag{3.29}$$

A stress influence on the fibre causes refractive index changes in the isotropic medium with a low intrinsic birefringence which, according to the photoelasticity theory [Gia81], [Gaf97], can be found as

$$\begin{aligned}\Delta n_x &= -\frac{(n_{eff})^3}{2E}\{(p_{11}-2\nu p_{12})\sigma_x + [(1-\nu)p_{12}-p_{11}](\sigma_y+\sigma_z)\},\\ \Delta n_y &= -\frac{(n_{eff})^3}{2E}\{(p_{11}-2\nu p_{12})\sigma_y + [(1-\nu)p_{12}-p_{11}](\sigma_x+\sigma_z)\},\end{aligned} \tag{3.30}$$

where E is the Young's modulus of the germanosilicate fibre core of approximately 74 kN/mm^2, p_{11} and p_{12} are Pokel's coefficients of the strain-optic tensor of approximately $p_{11} = 0.113$ and $p_{12} = 0.252$, and ν is the Poisson's ratio of approximately 0.16. In this low birefringence case, the birefringence introduced by the strain can be found from

$$B_S = \frac{|\Delta n_y - \Delta n_x|}{n_{eff}}. \tag{3.31}$$

Figure 3.12 shows the calculated stress part of the birefringence depending on the applied force.

FBG parameters are defined to use the coupled-mode theory for the perturbed medium. Initial conditions in the coupled-mode theory taken in section 3.1 are not acceptable in this case. It is important to take into consideration x- and y- polarisation components of the fundamental mode propagating along the fibre with elliptical cross-section. Changes in the dielectric tensor as the result of an applied transverse load will split into two parts

$$\begin{aligned}\Delta\varepsilon_x &= \varepsilon_a(n_x - n_{eff})^2,\\ \Delta\varepsilon_y &= \varepsilon_a(n_y - n_{eff})^2,\end{aligned} \tag{3.32}$$

where n_x and n_y are the refractive indices for the x- and y- polarisation respectively.

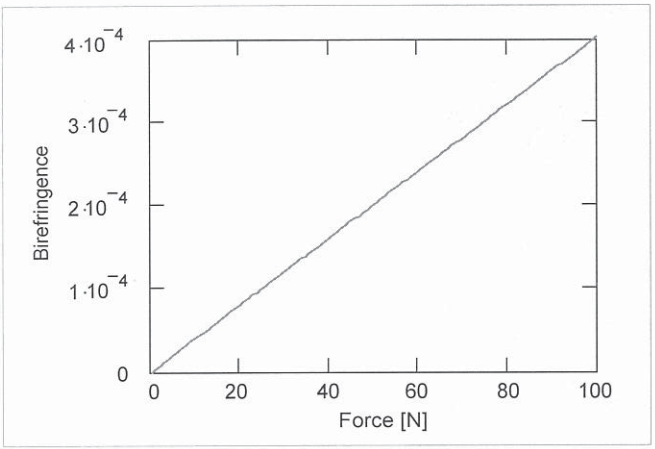

Figure 3.12: Calculated change of birefringence of the fibre in the result of load-induced geometry changes of the fibre.

The system of differential equations for the incident and reflected waves are given

for x-polarisation

$$\frac{dA_{1x}}{dz} = -j\kappa_x A_{2x} e^{j\Delta\beta_x z}, \qquad \frac{dA_{2x}}{dz} = j\kappa_x^{*} A_{1x} e^{-j\Delta\beta_x z},$$

for y-polarisation

$$\frac{dA_{1y}}{dz} = -j\kappa_y A_{2y} e^{j\Delta\beta_y z}, \qquad \frac{dA_{2y}}{dz} = j\kappa_y^{*} A_{1y} e^{-j\Delta\beta_y z}, \tag{3.33}$$

where A_{1x}, A_{1y} are forward-wave amplitudes and A_{2x}, A_{2y} are backward-wave amplitudes for x- and y- polarisation axes, $\Delta\beta_x = \beta - \beta_x$ and $\Delta\beta_y = \beta - \beta_y$ are x- and y- polarisation components of propagation constant change, κ_x and κ_y are x- and y- polarisation components of the coupling coefficient

$$\kappa_x = \frac{\pi}{\beta_x} \iint_{core} r\psi_x^{\,2}(x,y) k_0^{\,2}(x,y) m dx dy,$$
$$\kappa_y = \frac{\pi}{\beta_y} \iint_{core} r\psi_y^{\,2}(x,y) k_0^{\,2}(x,y) m dx dy, \tag{3.34}$$

where $\kappa = \kappa_x + \kappa_y$ and $\psi(x,y) = \psi_x(x,y) \cdot \psi_y(x,y)$. The scalar of the wave function in elliptical-core fibres can be given by

$$\psi(x,y) = \exp\left\{-\frac{1}{2}\left[\left(\frac{x}{x_0}\right)^2 + \left(\frac{y}{y_0}\right)^2\right]\right\}, \tag{3.35}$$

where x_0 and y_0 can be defined by the variation method (see Attachment A).

Using this model, reflectivity of the FBG for the case of an elliptical deformation is found as shown in *Figure 3.13*. The grating reflectivity will also have two components for x- and y- polarisation axes:

$$R_x = \frac{{\kappa_x}^2 \sinh^2[s_x \cdot L]}{{s_x}^2 \cosh^2[s_x \cdot L] + \left(\frac{\Delta\beta_x}{2}\right)^2 \sinh^2[s_x \cdot L]},$$

$$R_y = \frac{{\kappa_y}^2 \sinh^2[s_y \cdot L]}{{s_y}^2 \cosh^2[s_y \cdot L] + \left(\frac{\Delta\beta_y}{2}\right)^2 \sinh^2[s_y \cdot L]}. \quad (3.36)$$

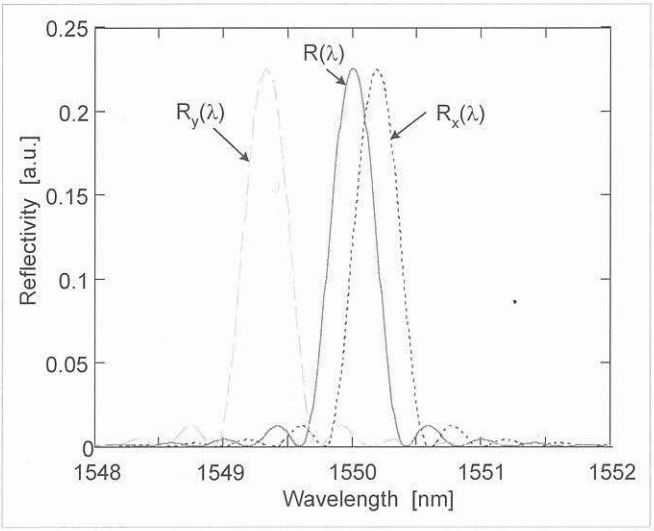

Figure 3.13: Reflectivity of 2 mm long FBG (1550 nm) with a circular and an elliptical cross-section of the fibre.

Elliptical cross-section induces splitting of the main Bragg peak into two.

Figure 3.14 shows reflection spectra of the uniform unperturbed FBG and the FBG under transverse load influence (plain strain case, where $\varepsilon_z = 0$). The grating reflection spectrum of perturbed with the stress linearly distributed along the grating axis also shows two clear peaks.

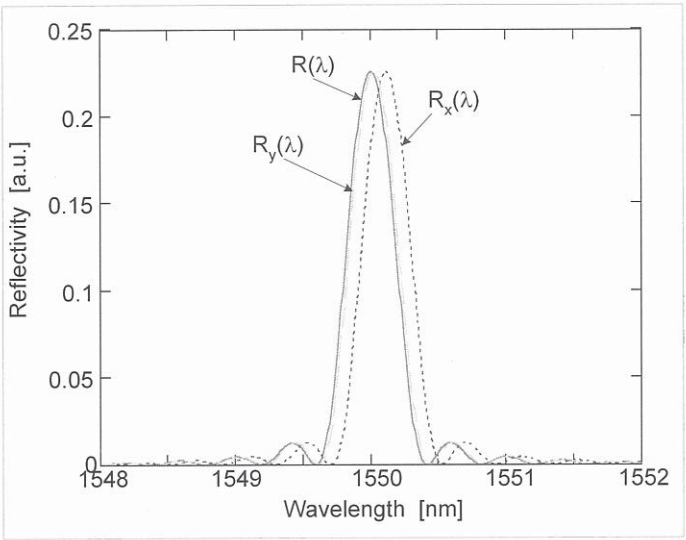

Figure 3.14: Reflectivity of 2 mm long FBG (1550 nm) at an applied transverse load of 15 N.

Calculations were provided for a short grating written in the core of germanosilicate single mode fibres. In such a medium, calculated stress component of birefringence shows noticeable changes in the reflected spectrum starting from a load of 15 N.

3.2.3 Effects of light propagating through the bent FBG

In praxis, FBGs are often exposed to microbending effects, especially due to the embedment procedure. There are few influences which have to be distinguished at modelling of the bent FBG. The refractive index changes along the transverse coordinates of the fibre are caused by the stress of the fibre material and lead to the birefringence effect. The resulting splitting and shift of the FBG wavelength are caused by the birefringence in the bent area and the grating planes inclination. The optical path of the transmitted light changes which lead to the transmitted light loss.

The theoretical approach can consider tilted structure (see *Figure 3.15*) [Oth99], [Pra02] or non-uniform inclinations of the grating planes [Gon01] in the case of a long FBG. It is possible to evaluate behaviour of the grating signal in such a situation using coupled-mode and perturbation theories for light propagation in perturbed medium [Oth99].

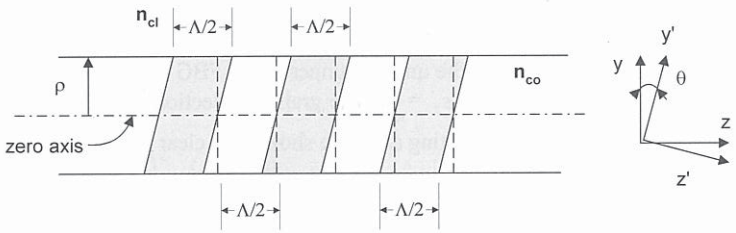

Figure 3.15: Schematic representation of the tilted FBG.

The model describing symmetrical inclinations of the grating planes to the grating axis (see *Figure 3.16*) will be used in this chapter. The wavelength shift [Gon01] as well as a reflectivity loss [Pra02] of a bent FBG depends on the radius of the bent area curvature. In such a case, the FBG could not be considered as a uniform structure anymore. Bent fibre suffers from compression on the one side and from expansion on the other side (see *Figure 3.16*). The light propagating through this area of the fibre at the same refractive index value finds different lengths between points. It is possible to convert this difference of the optical paths into inclination of the gratings planes as shown in *Figure 3.16*.

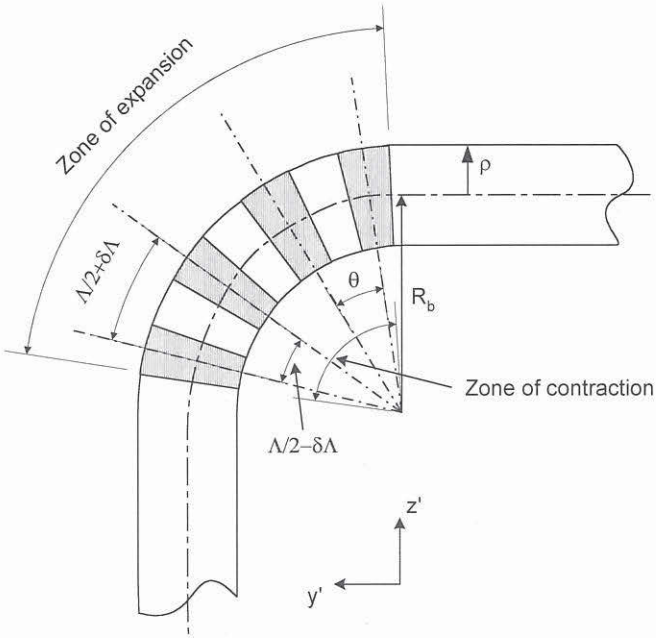

Figure 3.16: Schematic representation of the bent fibre with FBG.

The modification of the grating period owing to the bending effects is shown in *Figure 3.16*. The correction of the FBG period is given by

$$\delta\Lambda = \frac{\Lambda'}{2}, \tag{3.37}$$

where $\Lambda' = \frac{\Lambda}{2R_b}\zeta$, ζ is the distance from the axis of the fibre and R_b is the bending radius. The induced changes in the refractive index of the perturbed FBG along the fibre axis z are

$$\delta n_{eff}(y,z) = \Delta n(z')\left[1 + m\cos\left(\frac{2\pi}{\Lambda}z'\right) + \varphi(z')\right], \tag{3.38}$$

where $z' = z\cos\theta$, $\Delta n(z')$ is the refractive index changes in the fibre core along the axis z', m is the fringe visibility of the refractive index, and $\varphi(z')$ is a part accounting perturbations in the

gratings geometry, for example induced by strain: $\varphi(z') = \frac{2\pi}{\Lambda}\frac{\varepsilon_{z'}}{1+\varepsilon_{z'}}$. The modified modal distribution of the propagated and reflected modes in the bend area introduces change into the coupling coefficient. The coupling coefficient can be defined as follows

$$\kappa(z,\theta) = \frac{\pi n_{co}}{2\lambda} m\Delta n(z') \iint_{co} \psi^2(r,\phi) \exp\left(\pm j\frac{2\pi}{\Lambda} y \tan\theta\right) r\partial r\partial\phi \,, \tag{3.39}$$

where $y = \begin{cases} r\cos\phi \\ r\sin\phi \end{cases}$ for the grating planes tilted in the direction of the bend and opposite.

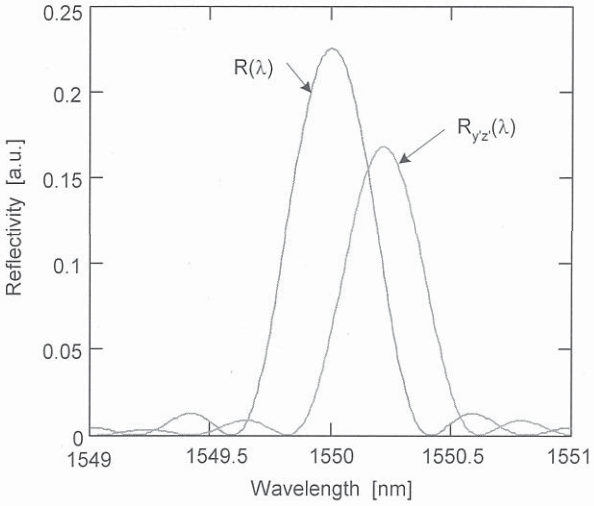

Figure 3.17: Changes in the 2 mm long FBG reflection spectrum due to the uniform bending with a radius 2.5 mm.

Considering this, the calculated reflection spectrum of a bent FBG is shown in *Figure 3.17*. For short gratings, the radius has to be small (< 2.5 mm) to induce a large deviation from the uniform spectrum. The splitting of the grating wavelength occurs due to the birefringence effect within the stressed area of the fibre. In other terms, inclination of the grating planes and strain, which produce this inclination, cause the grating wavelength displacement, refractive index changes, which induce splitting of the FBG main peak, and changes of the optical path of the propagated light in the bent area result in the reflectivity loss.

4 Investigations of thermal and mechanical influences

For the past decade, FBG sensor architectures have found wide application in monitoring large-scale structures or their parts, as well as in research of new materials, and they have proved their capability to replace existing techniques for measurement of linear strain, non-uniform strain fields, transverse load, temperature, vibrations, or combinations of these values, such as strain-temperature or vibrations-temperature influences. Fibre Bragg gratings are characterised by their small dimensions, absolute measurement ability, good response time and sensitivity, reliable operation in adverse environments, such as radiation, extreme temperatures, or embedment into composite or other complicated materials. But problems in this field still remain, even if some solutions have been found, such as application of FBG sensors recoated with polyimide or ORMOCER® material, when the FBG strain-response or the FBG temperature sensitivity has to be linear, and improvements of embedment technique in a case of concrete or composite material-integrated FBG sensors [Hab00], [Tru01], [Heg01], [Lop02].

This chapter discusses aspects of various influences. Some of them, such as uniaxial strain or temperature, represent the measured signal. Another influences, such as bending, transverse local or general stress, are considered as perturbations of the measured signal. These influences have to be qualified and quantified to evaluate sensor response correctly and reliably.

Following FBGs were investigated in this chapter: 10 single FBGs from AOS GmbH, one single FBG from IPHT Jena, 18 single FBGs, 9 embedded FBGs, one embedded 3-FBGs array, one embedded 8-FBGs array, and one not applied 8-FBGs array from Ingenieurbüro Jens Peupelmann, and FBG Sensor Rod from Telegärtner GmbH. These gratings were mostly acrylate-recoated including two bare gratings (details see in Attachment D).

4.1 Strain sensitivity

FBG behaviour under influence of a uniaxial strain and comparison between the behaviour of a bare grating, an industrial sensor based on the FBG, an embedded grating, and a grating attached to the surface of investigated material, is investigated in the following subsection. The purpose of these investigations is to prove some problems connected with the FBG application on or inside the sensor housing or material and show possible solutions.

Standard fibre Bragg gratings were used for linear strain investigations in an experimental set-up. Characteristics of the FBG were recorded using available industrial measurement equipment, such as a broadband source (BBS, JDS Uniphase) or a tunable laser (TL, ANDO Electric Co. Ltd.) and an optical spectrum analyser (OSA, ANDO Electric Co. Ltd.) with a resolution of 8 pm, or a swept laser

interrogator (SLI, Micron Optics Inc.) with a resolution of 1 pm. All investigations were conducted under stable climate-room conditions to reduce additional influences such as temperature, moisture, and vibrations.

4.1.1 Uniaxial strain of the bare grating

Before going on to more complicated cases, where gratings are attached to or embedded in a material, a simple case of a "bare FBG" was considered. A single mode fibre with inscribed short FBG into a fibre core, recoated with acrylate coating, will be referred to as a "bare FBG" in this subsection. Calibrated equipment of BAM Laboratory S.11 "Reliability of Testing and Measurement Systems" was used for measurement of mechanical parameters. The measurement set-up could be divided into monitoring scheme of mechanical and optical characteristics. The mechanical equipment consists of a special tensile testing machine with two free-moving joints 1, a load cell 3 calibrated up to 50 N (see *Figure 4.1*), and an elongation meter 3 (see *Figure 4.2*). The optical equipment consists of light sources 1 and an OSA 2, which allows recording of FBG characteristics during experiments (see *Figure 4.2*).

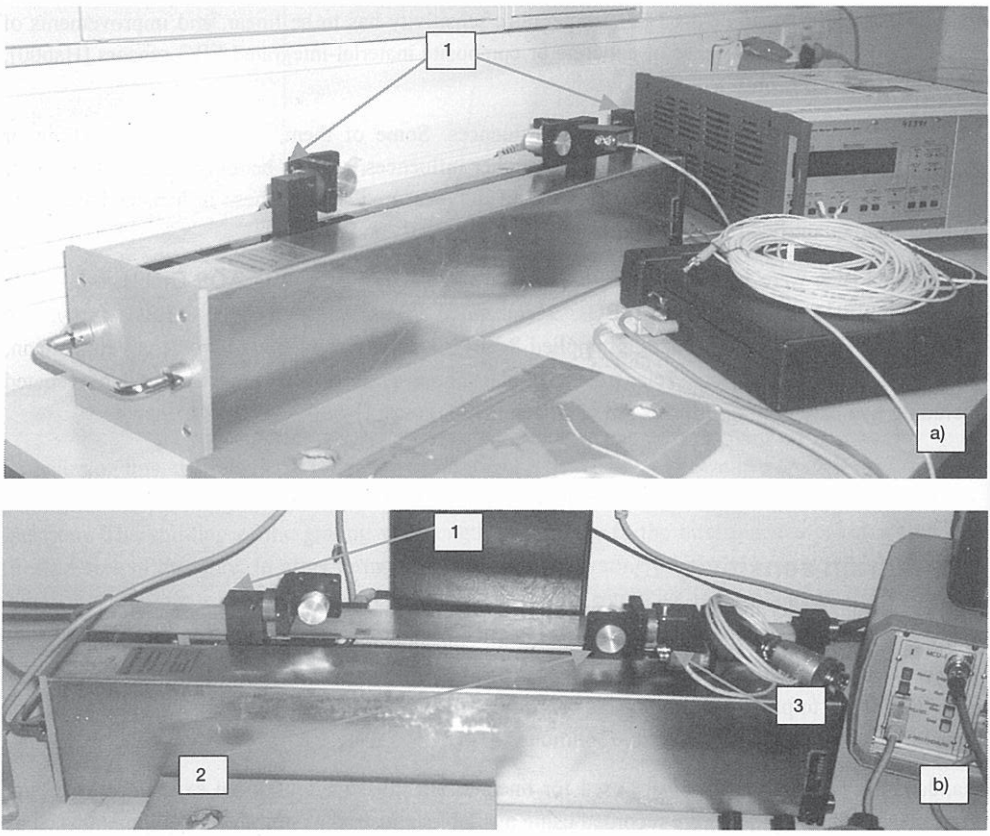

Figure 4.1: The tensile test machine: 1 - free-moving joints; 2 - aluminium cylinders; 3 - load cell.

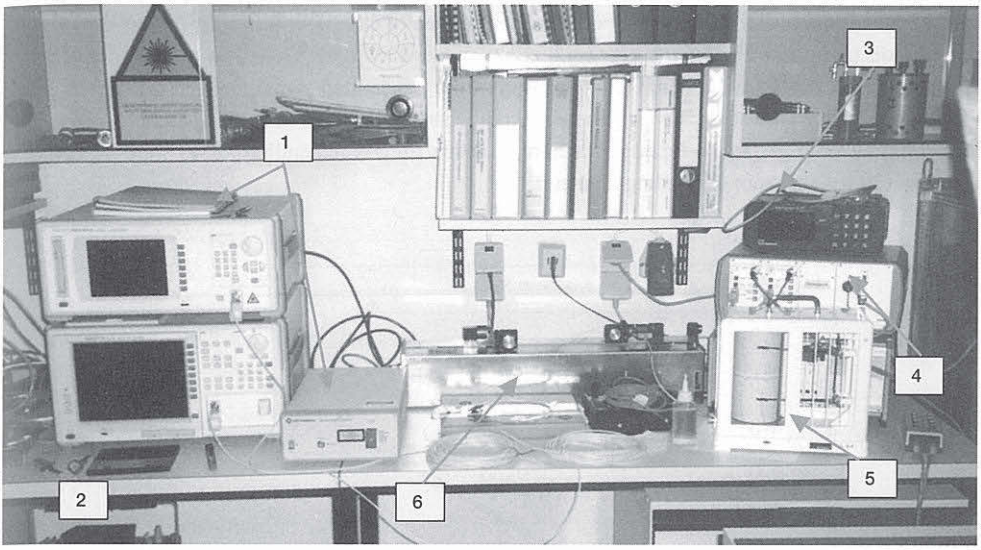

Figure 4.2: Measurement set-up: 1 - light sources; 2 - OSA; 3 – elongation meter; 4 – controlling unit of the tensile test machine; 5 – moisture and temperature meter; 6 – tensile test machine.

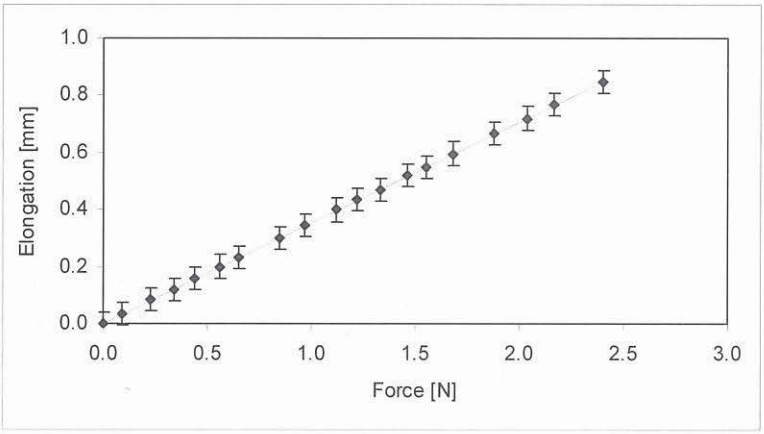

Figure 4.3: Dependence of the elongation of the fibre on an applied force during one of the experiments.

A step-wise operation program was chosen for a tensile machine to increase a fibre tension. The first "zero" position is achieved when the FBG is prestrained to approximately 0.01 N. The operation program is created so that it reached the previously defined maximum strain value in 20 steps and then moved back. The tensile machine stops for 5 minutes when the defined load value is achieved. This provides the time needed for the measurement of mechanical and optical values. *Figure 4.3* shows the fibre elongation dependence on the applied force measured during experiment.

The FBG was fixed in the tensile testing machine so that the fixing points had the minimum influence on it, which did not affect the transmitted signal. The leading fibre was wrapped around

aluminium cylinders and fixed at two points on the surface of each cylinder by using two-component epoxy glue (measurement length between fixing points 316 mm). Cylinders with a diameter of 25 mm were chosen to avoid bending attenuation of the transmitted signal through the optical fibre. FBGs used for present investigations were inscribed into a commercially available telecommunication germania-doped silica fibre. For this fibre type bending losses were observed at less than (20.0 ± 0.1) mm of bending diameter.

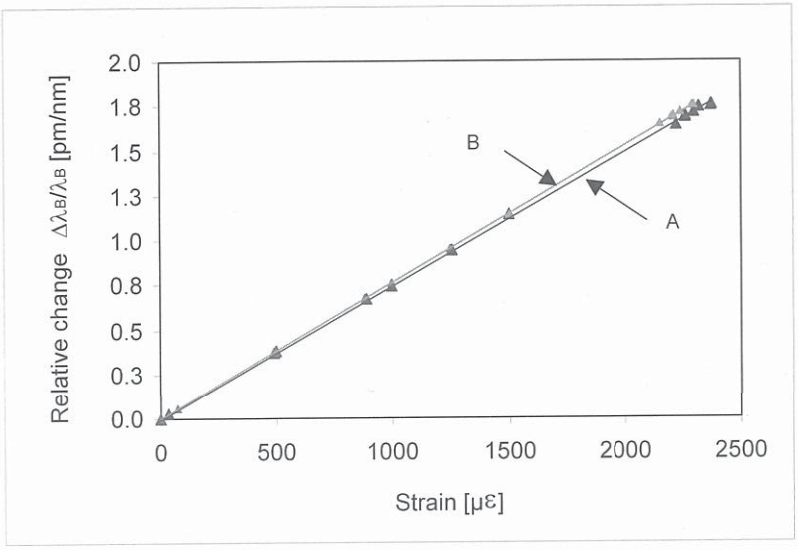

Figure 4.4: Dependence of the Bragg wavelength change on the strain measured by tensile test machine (A) and calculated from the well known FBG strain sensitivity theory (B).

Figure 4.4 (A) shows the dependence of the Bragg wavelength change on the strain of the fibre measured with the tensile test machine. Existing mathematical model of the axial intra-grating strain influence is described in Chapter 2. Along this model, calculated sensitivity of the FBG to the axial strain is 1.2 pm/$\mu\varepsilon$. Measured values of the fibre elongation and the force applied to the fibre ends are larger than the elongation and the force acting in the FBG area (see *Figure 4.4* B). This introduces relative deviation between measured and calculated data of 2.12 % for the strain value 0.25 %.

It is important to notice also that the theoretical model do not consider the coating influence of the FBG, which in some cases, can have large influence on the measured data, too [Tru01]. In the praxis, most important parameters of optical fibre and its coating are not available such as exact period of the grating, effective refraction index, material properties: thermo-optic and photoelastic coefficients, elasticity modulus, and temperature sensitivity coefficient of the grating. There data are not commercially available. Therefore, it is very difficult to compare experimental data with theoretically obtained one.

The experiment was repeated 10 times, and afterwards the FBG was strained with an applied load of (2.290 ± 0.018) N for 25 days. *Figure 4.5a* shows the grating wavelength measurement (1572.498 ± 0.002) nm over 25 days. Deviations of the measured data occurred between the 7th and

9th days due to temperature variations of ± 1.1 °C. It corresponds to the data (A) in *Figure 4.5a*. *Figure 4.5b* shows measured force during the same period.

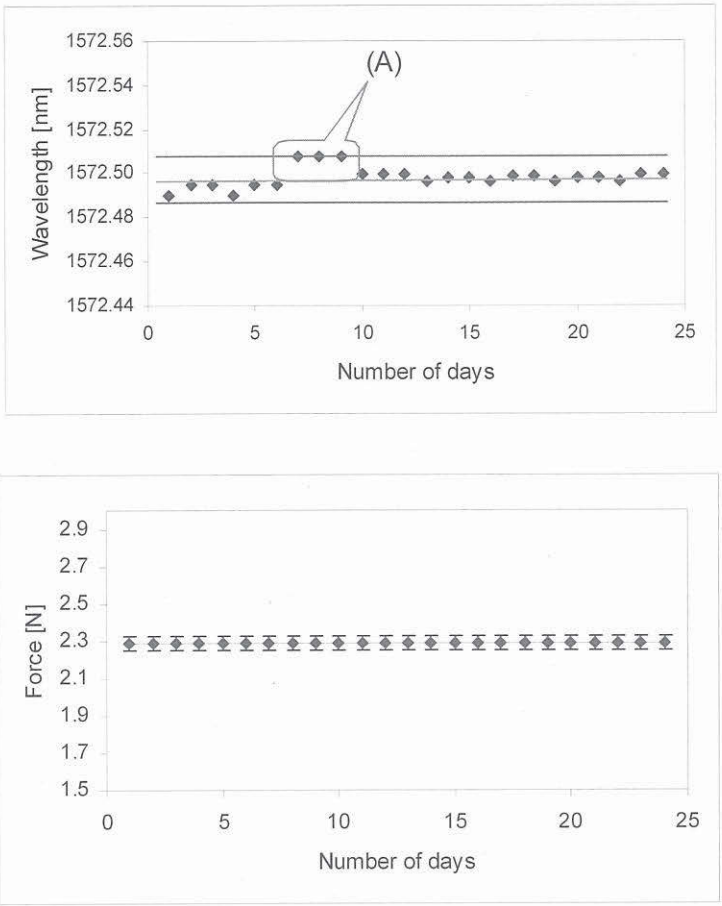

Figure 4.5: Measurements of the wavelength (a) and the force (b) under stable conditions over 25 days.

Figure 4.6 shows loading diagram of investigated FBG during 6 months. *Figure 4.7* shows strain sensitivity of the FBG before and after 6 months of testing with applied strain of approximately 0.25 %. After 6 months of axial straining, FBG shows smaller strain sensitivity approximately of 3.2 %.

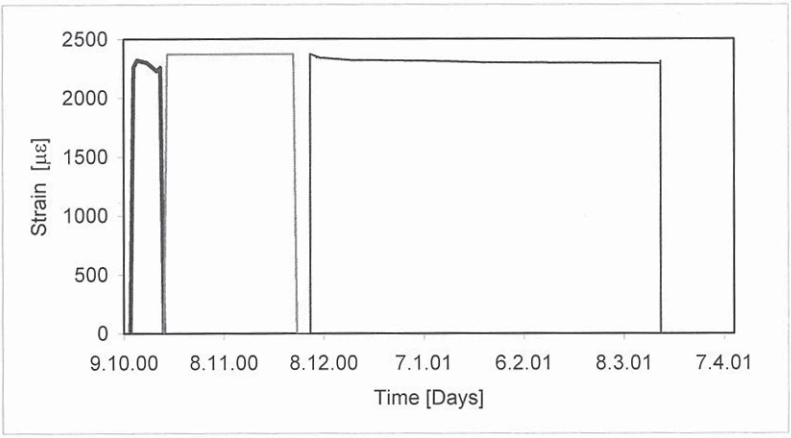

Figure 4.6: Loading diagram of the FBG during 6 months.

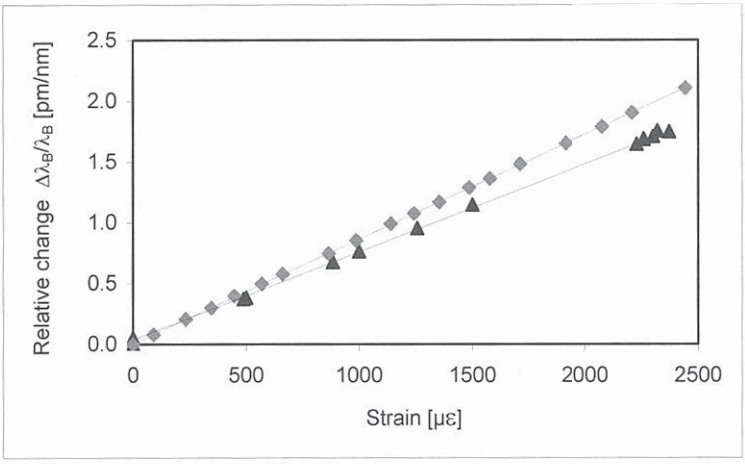

Figure 4.7: Strain sensitivity of FBG measured on the beginning and after 6 months of investigations.

Figure 4.8 shows grating transmission spectra under an applied strain of approximately 0.25 % measured at the beginning and after 6 months of investigations. For these two cases, evaluated FBG strain sensitivity at the beginning of investigations was (1.202 ± 0.002) pm/με * and after 6 months of investigation was (1.262 ± 0.024) pm/με *.

* The expanded standard uncertainty with the coverage factor 2 includes repeatability and correctness of the measurement.

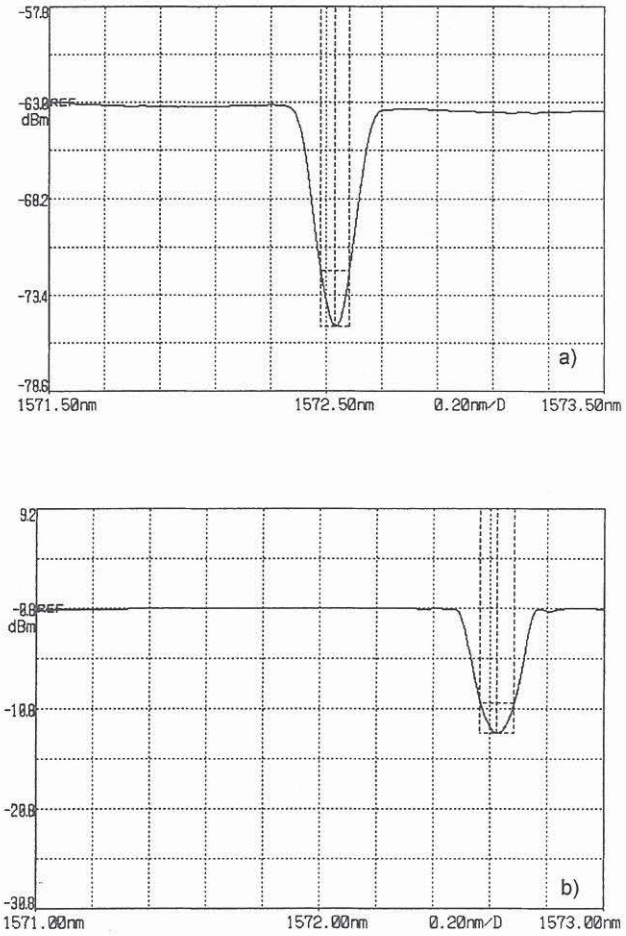

Figure 4.8: Transmission spectrum of the FBG (1569.816 nm) under applied strain approximately of 0.3 %: a) on the beginning of investigations; b) after 6 months of investigations***.*

Long-term stability of FBGs used in the telecommunication field are already investigated by EMPA laboratory [Nel00]. There were no changes in the grating sensitivity to applied strain observed. Present investigations with the FBG fabricated for sensor applications revealed small strain-sensitivity deviation. It is important to provide further investigations of the FBG strain sensitivity to prove if this is systematic problem or only defect of this one grating.

* Measured with the BBS.

** Measured with the TL.

4.1.2 Uniaxial strain of a FBG fixed in a sensor rod

A Bragg grating (1553.13 nm) has been fixed inside a steel rod in order to make the fibre-grating sensor usable for construction areas [Peu99]. In the present subsection the strain or contraction behaviour of such a rod has been tested under axial strain deformation. The schematic drawing of the housing of the steel sensor rod (SR) is shown in *Figure 4.9*.

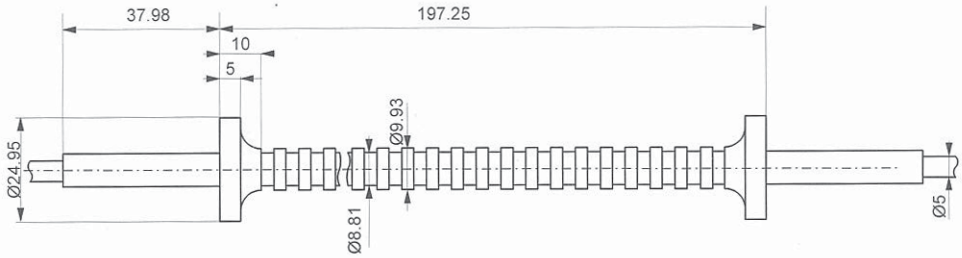

Figure 4.9: Schematic drawing of the steel sensor rod housing (in mm).

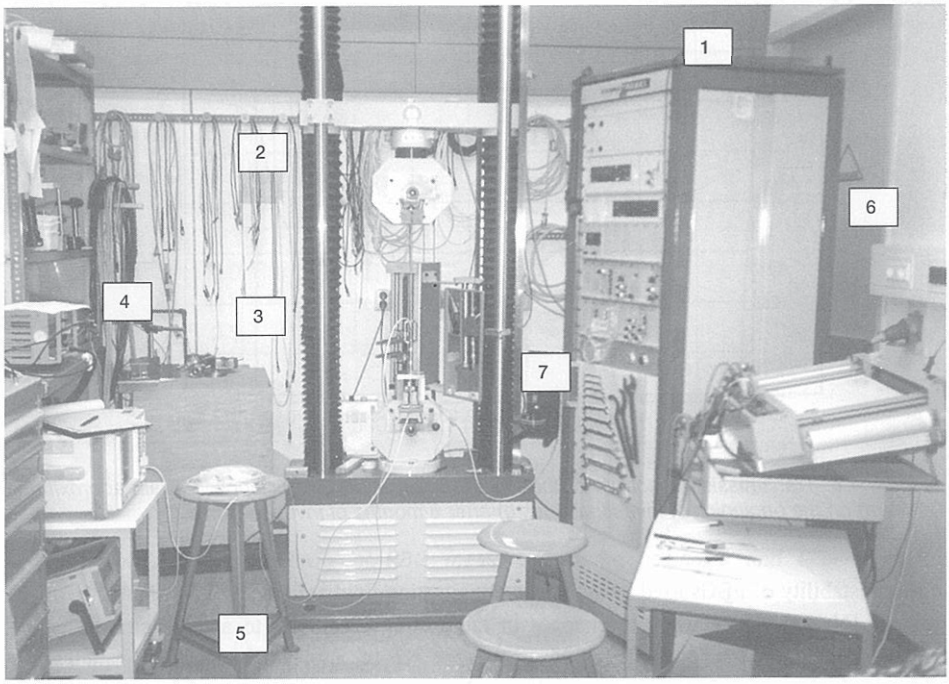

Figure 4.10: Measurement set-up: 1 – tensile test machine; 2 – load cell; 3 – steel sensor rod; 4 – OSA; 5 – broadband light source; 6 – plotter; 7 – elongation meter.

The experimental set-up included: a tensile testing machine calibrated for a load up to 10 kN, an elongation meter, an OSA, and a BBS (see *Figure 4.10*). This equipment allowed recording of mechanical characteristics and the evaluation of the shape changes in the FBG transmission spectrum. A bending-free fixation of the SR in the grips of the tensile machine was chosen (see

Figure 4.11). This type of fixation avoids bending of the rigid sensor housing in a case of a stiff fixing.

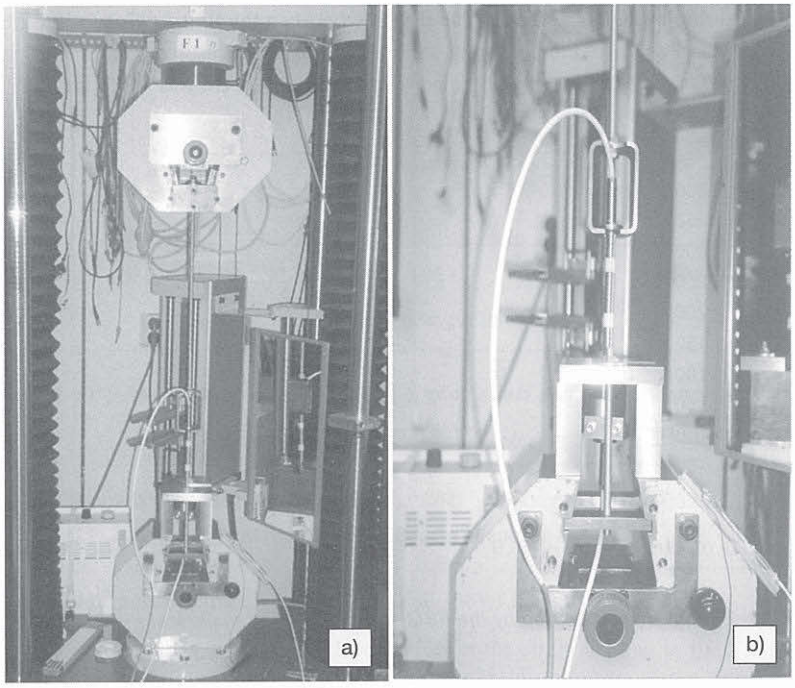

Figure 4.11: Sensor rod fixing.

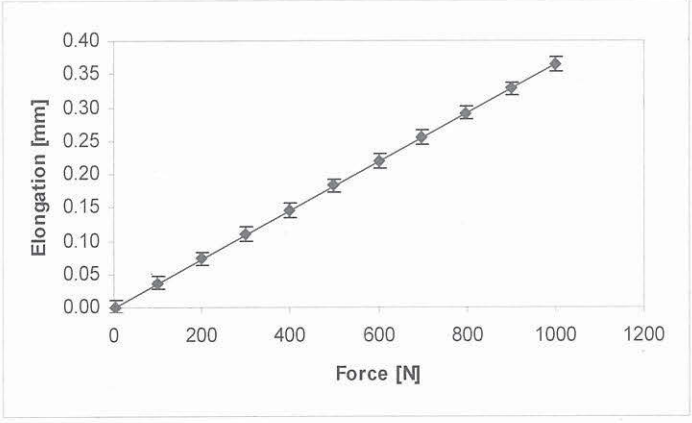

Figure 4.12: The dependence of elongation of the steel sensor rod on applied force read by mechanical tensile test machine.

Figure 4.12 shows the dependence of the steel rod elongation on an applied force. The standard uncertainty of an elongation meter is ± 0.2 mm and of the tensile machine is ± 2.2 N. The tensile test

machine is controlled in the same way as in previous subsection: it moves up till the maximum force of 1 kN in 12 steps and stops at each step for 5 minutes. Uniaxial tensile tests were repeated 7 times. The measuring basis defined by the distance between the SR caps was 187.25 mm (see *Figure 4.11*). The chosen measuring basis is the same as the distance between the fixing points of the fibre inside the sensor housing. For each measurement step, the mean of measured values was taken into consideration. The standard uncertainty of the wavelength measurement was $\pm$ 5 pm.

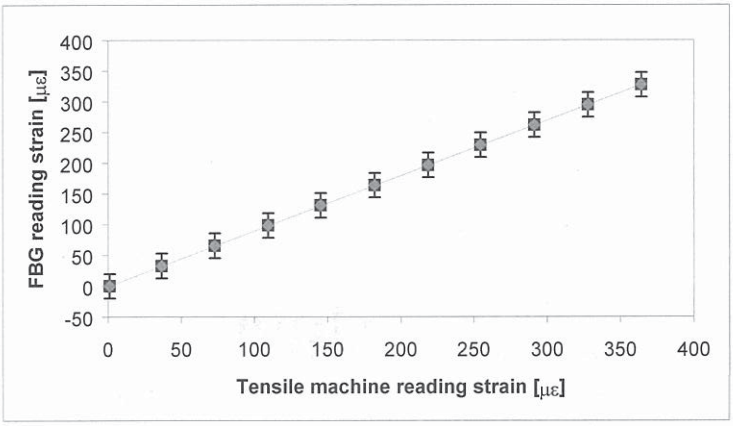

Figure 4.13: Strain values recorded by the FBG sensor and the tensile test machine sensor.

Strain values read with the FBG sensor and the tensile testing machine sensor are shown in *Figure 4.13* for a series of investigations. An estimated relative deviation of reading strain with FBG sensor is 3.82 % and with the tensile machine sensor is 3.52 %.

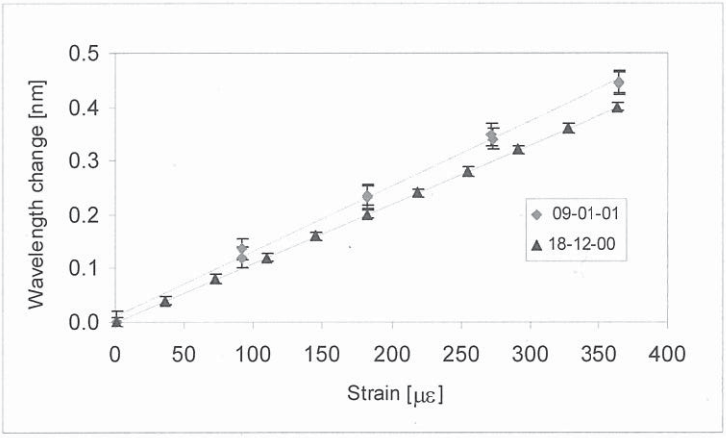

Figure 4.14: The Bragg wavelength dependence on strain applied to the SR.

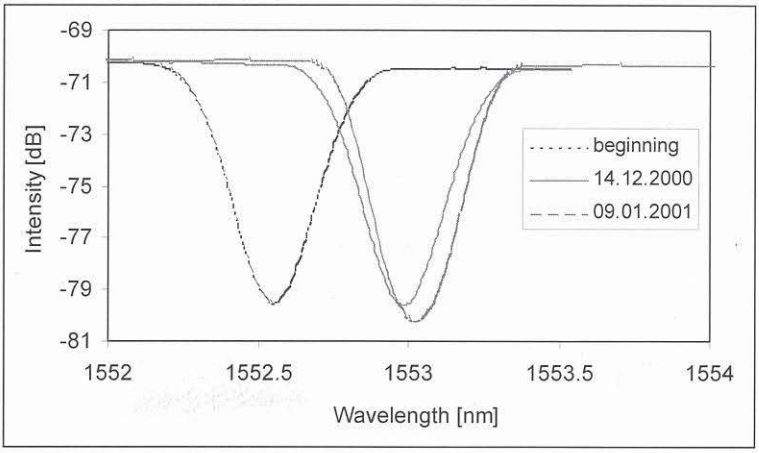

Figure 4.15: FBG transmission spectra without applied strain and at 0.3 % strain applied to the SR before and after permanent straining.

The grating wavelength changes by 0.4 nm and the steel SR elongates by (0.067 ± 0.012) mm at the applied force of 1 kN. The strain of $\varepsilon_z = \frac{\Delta l}{L} \cdot 100\%$ = 0.036 % corresponds to these conditions. Measured grating response to the elongation of the SR shows linearity.

Figure 4.14 shows the Bragg wavelength dependence on the strain applied to the SR for two tests made before and after permanent straining of the sensor. At the beginning of the investigation, the average FBG sensitivity over the SR strain estimated after five tests was (1.14 ± 0.05) pm/με. Then the SR was strained until 0.3 % for three weeks under stable climate conditions. The evaluated FBG sensitivity afterwards was (1.223 ±0.037) pm/με.

The Bragg wavelength shift from normal position is shown in *Figure 4.15*. The last value of the FBG strain sensitivity agrees well with the theoretical value. All trials have shown excellent reiteration along two curves shown in *Figure 4.14*, so it can be concluded that some permanent changes were introduced to the sensor housing. The FBG response, however, kept its linearity. On the other hand, with such a small strain, no disagreement or non-linearity in measured data can be expected.

4.1.3 Embedded gratings

Embedded FBGs can directly sense mechanical influences affecting the structure. This capability is used to investigate new materials, such as composites. In some cases, it cannot be avoided that the surrounding material perturbs the FBG signal. Such perturbing influences could be microbending, transverse or point-wise pressure. The latter influences cannot only introduce distortions into transmitted or reflected signal of the FBG, but also lead to extensive damage of the fibre or the FBG inside the material to be evaluated.

Embedment

Four simple FBG sensors, 3-FBG-sensor and 8-FBG-sensor arrays were embedded into a specifically structured, composite material to evaluate the signal behaviour of the embedded gratings.

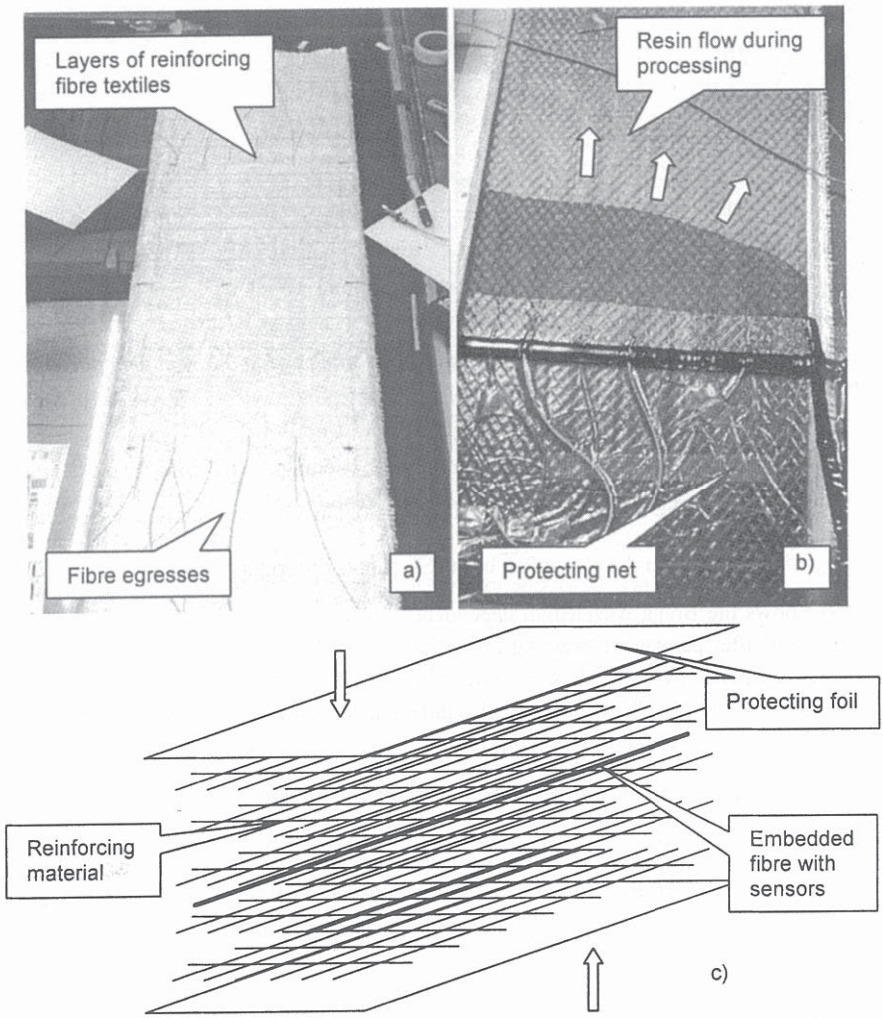

Figure 4.16: Embedment procedure: a) fibre sensors integration into the composite; b) filling up the composite with epoxy resin; c) scheme of the reinforced material.

The reinforcing material is a special texture formed by the crossings of tiny fibre bundles as shown in *Figure 4.16*. Several layers were placed one over the other. Optical fibres with FBG sensors were placed between reinforcing layers. Afterwards, the structure was covered with a protecting foil and filled under vacuum with an epoxy. The epoxy was cured at 60 °C for one hour. Fibre egresses were protected with a polyethylene film sealed with a black resin to avoid ingress of the epoxy.

Complications were expected when embedding optical fibres into such composite material, due to crossings of reinforcing fibre bundles (see *Figure 4.17*). Periodical microbending and small tangential stress effects as well as a transverse stress affecting the fibre in composite were expected after curing. These periodical perturbations induced by the reinforcing material have a point-wise character, taking into consideration dimensions of reinforcing material crossings. *Figure 4.17a* shows the microsection of the laminated plate with fibre egresses protected from the epoxy with a buffer. Longitudinal crosscut shows straight horizontal position of the fibre and transverse bending of the fibre inside the material (see *Figure 4.17b*).

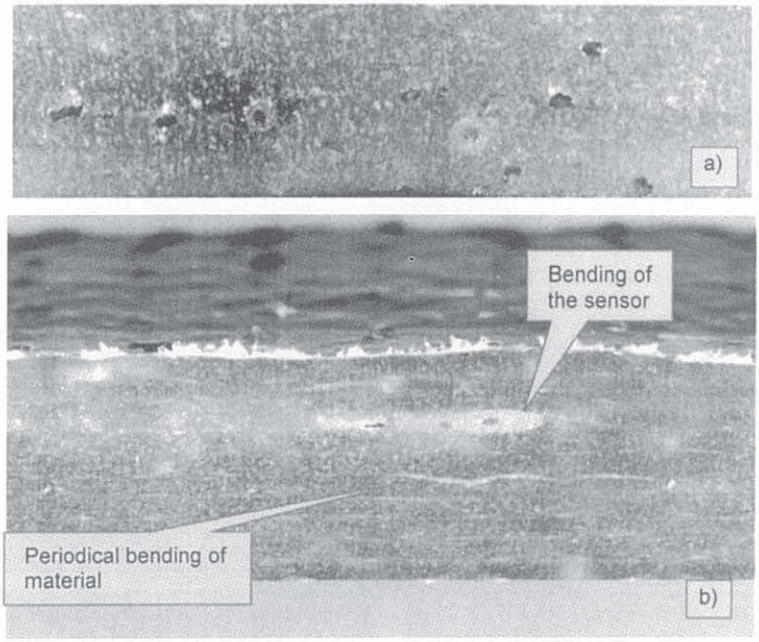

Figure 4.17: Digital photos of crosscuts of the specimen with embedded fibres: a) cross-section; b) longitudinal section.

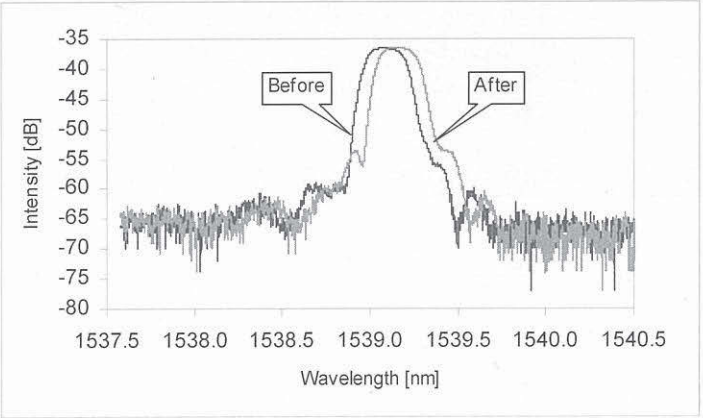

Figure 4.18: Reflection spectra of the FBG before embedment and after curing.

Nevertheless, all FBG sensors survived after embedment and showed satisfactory behaviour. Small changes in the spectrum reflected from the embedded FBGs were observed. Observed residual changes in the signal reflected by one of the gratings are shown in *Figure 4.18*. A sideband increase of 2 dB and 7 dB and spectrum broadening are results of the transverse stress influence. The estimated theoretical transverse strains, which induce central wavelength shift of 0.092 nm, are $\varepsilon_x = 85.5\ \mu\varepsilon$ and $\varepsilon_y = -24.6\ \mu\varepsilon$. This leads to a Poisson effect, which results in a strain causing FBG wavelength shift to the right side of the spectrum.

Creation of specimens

Specimens have to be cut from the composite plate with embedded sensors for further investigations. In order to form the specimen, two cutting techniques were taken into consideration: mechanical and water-beam cutting*. Microsections of cut specimens are shown in *Figures 4.19* and *4.20***.

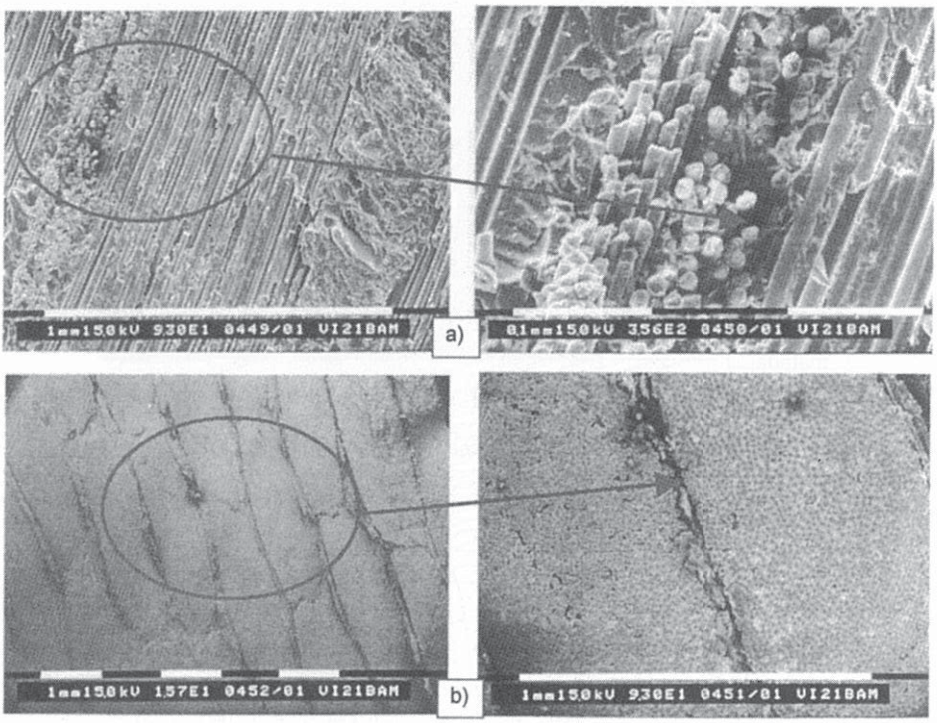

Figure 4.19: Microsections of the composite cut made by a mechanical cutting technique: a) longitudinal sections; b) cross-sections.

* Cutting procedures using equipment of the Laboratory S.322: Workshops for Scientific Instruments and Samples, BAM.

** SEM photos were taken in Laboratory VI.21: Micromechanics of Polymers and Composites; Interfaces, BAM.

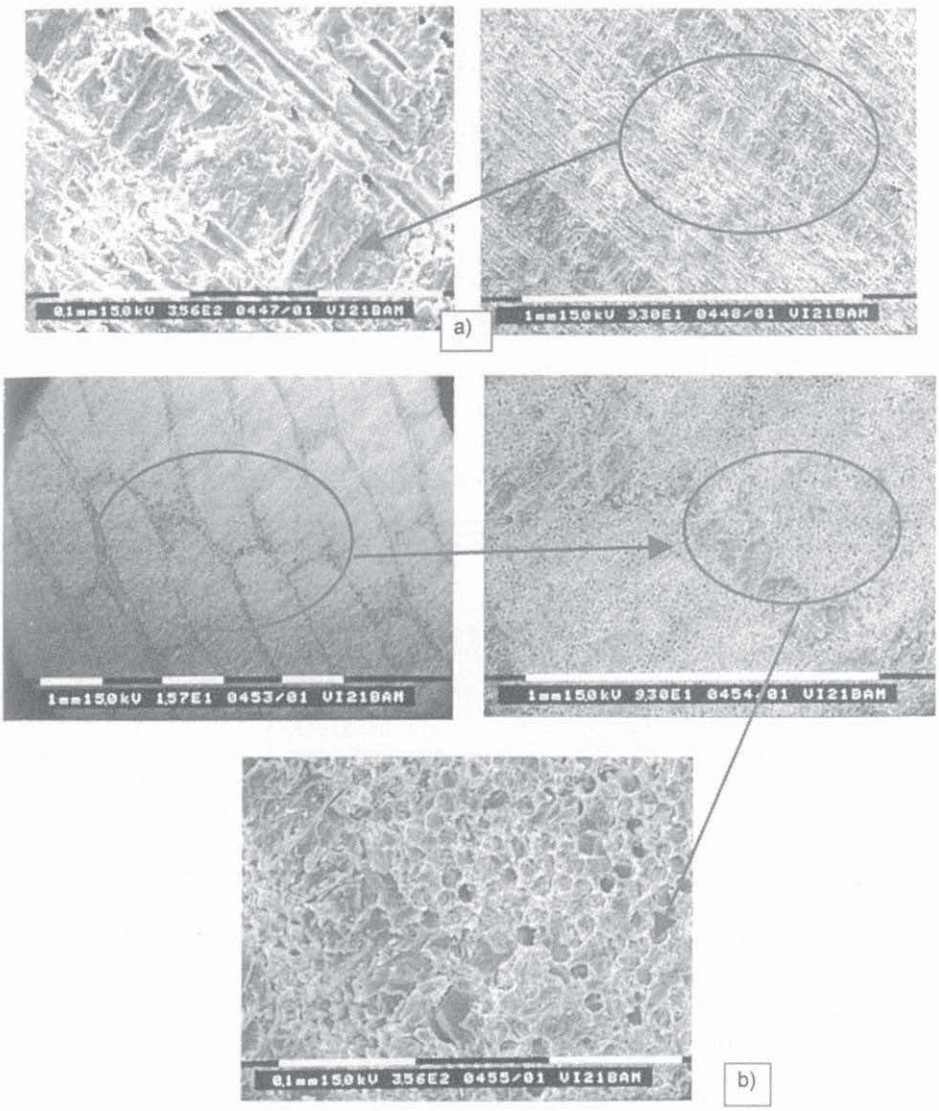

Figure 4.20: Microsections of the composite cut by a water-beam cutting technique: a) longitudinal sections; b) cross-sections.

After the lamination, crossings of the reinforcing texture layers made composite non-homogeneous, especially, deflect embedded sensor fibres. A microsection investigated in a scanning electron microscope (SEM) revealed undulations in the internal structure (see *Figure 4.19b left*). *Figures 4.19a* and *4.20a* show longitudinal cuts of the plate made with the different cutting techniques. Differences in cut surfaces can clearly be observed. The specimen surface cut with the water-cutting machine looks smoothly (see *Figure 4.20b*) and in the result of numerous investigations, delamination was not observed.

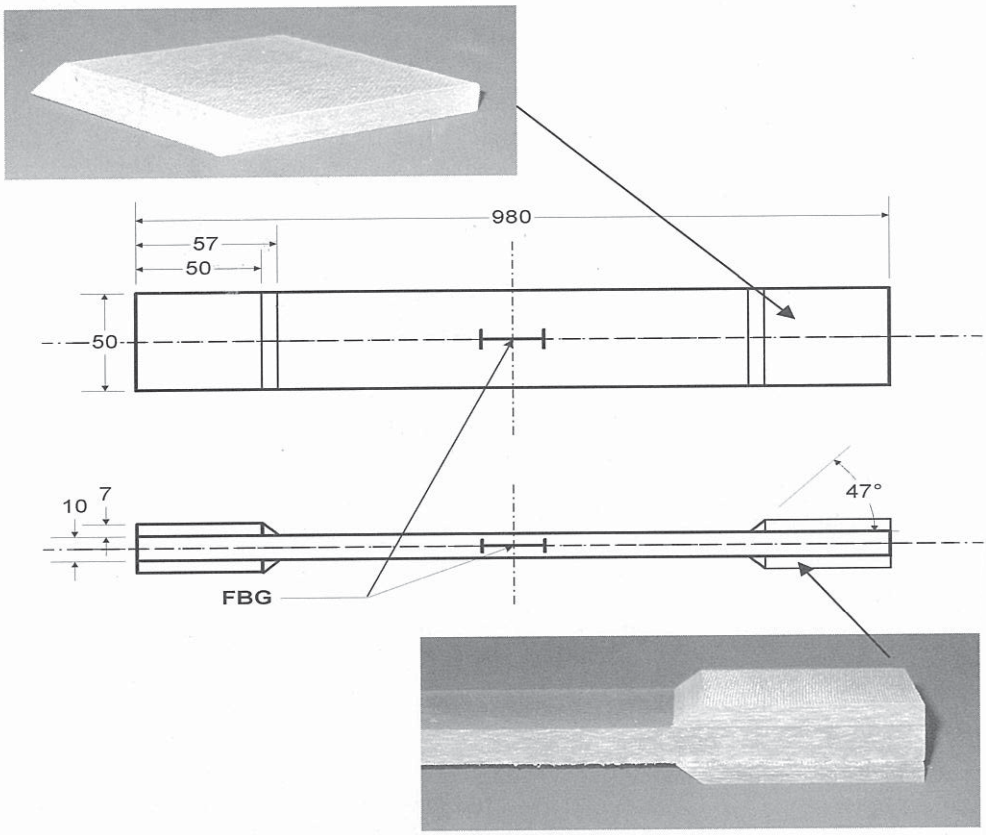

Figure 4.21: Geometry and dimensions of the specimen in mm.

The manufactured composite plate with embedded sensors was cut for further tests into five specimens. Specimens have been designed according to recommendations of the European Standard EN 61"Glasfaserverstärkte Kunststoffe" ("Textile-reinforced plastics; determination of tensile properties") for mechanical testing of composite materials. *Figure 4.21* shows specimen prepared for further investigations.

Uniaxial strain

In order to investigate the influence of a uniaxial strain on the manufactured specimen, a tensile test machine calibrated for loads up to 250 kN, an elongation meter, and a swept laser interrogation unit (SLI) were chosen (see *Figure 4.22*). Specimens were fixed in free-moving grips of the tensile test machine as shown in *Figure 4.22c*.

The tensile test machine was controlled to strain the specimen until 0.3 %. After that, it was held for 15 minutes and then the load was decreased to zero. The strain value of 0.3 % corresponds to the applied load of approximately (56.72 ± 0.01) kN and to the specimen elongation of (3.245 ± 0.004) mm. Mechanical characteristics show linearity and stability over the tested range for

5 tested specimens. A standard uncertainty for the FBG wavelength measurement of one sensor was ± 0.5 pm.

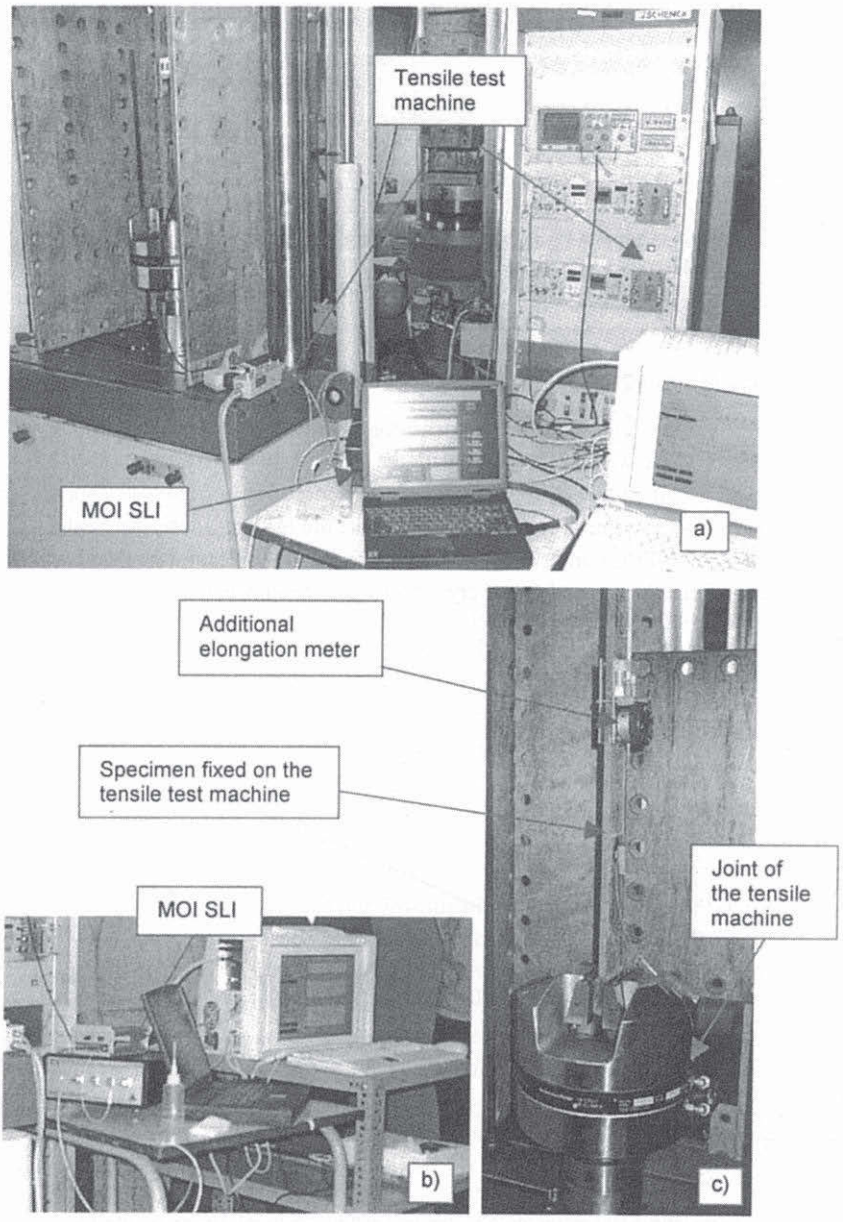

Figure 4.22: Measurement set-up.

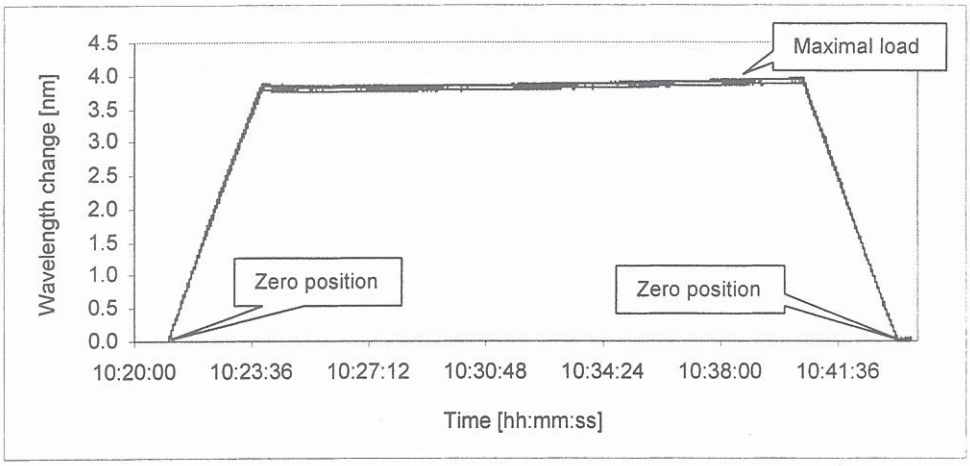

Figure 4.23: Measured Bragg wavelength changes of a 3-FBGs array at straining until 0.3 %.

The tensile test machine was synchronized with the swept laser interrogation unit (SLI) to provide a real-time record of all measured data. The real time measurement allowed data recording every 40 milliseconds. Five specimens were tested to evaluate the FBG response. The real time wavelength measurement of the 3-FBGs array is shown in *Figure 4.23*. The Bragg wavelength was changed by approximately 3.9 nm during straining every sensor in the specimen until 0.3 %.

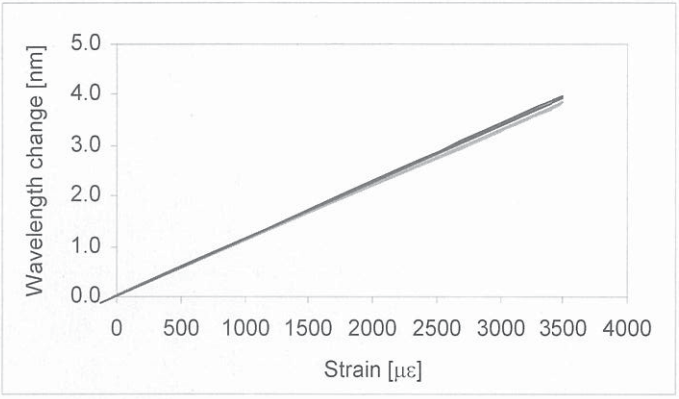

Figure 4.24: Measured dependence of Bragg wavelength change on applied strain for two embedded FBGs.

Figure 4.24 shows the FBG wavelength changes when an axial strain is applied to the specimen containing two FBG sensors. An excellent linearity of the sensor responses is registered for every tested specimen under these testing conditions, but the difference between strain sensitivity of these two sensors of ± 0.0025 pm/με can be observed. This deviation result from different positions of the sensors in the material and from additional local influences as well. Comparing data obtained from

two sensors positioned between the same layers inside the material, the deviation of ± 0.0019 pm/με is registered.

For a strain of $\varepsilon = 0.3$ %, an averaged grating wavelength shift equals 1.2 nm/mm. The mean FBG sensitivity to an applied strain to the specimen of all tested sensors is 1.1736 ± 0.0131 pm/με.

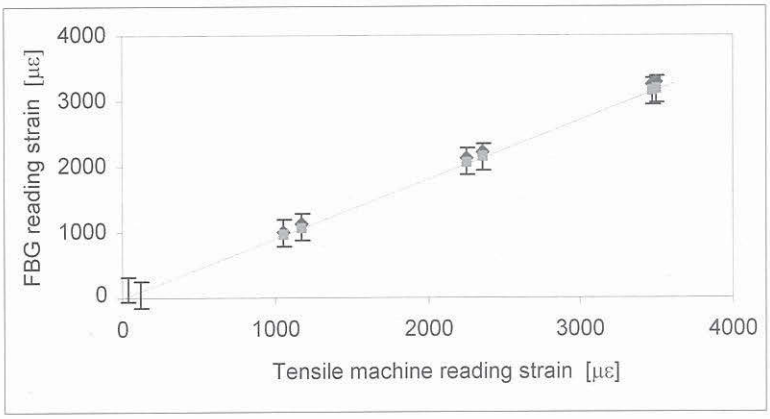

Figure 4.25: Comparison of the strains registered by the FBG sensor and by the tensile testing machine for two sensors.

Figure 4.25 shows the correlation of the specimen strain read out with FBG sensor and with the tensile test machine sensor. A relative deviation of the machine-read strain is calculated at 7.16 %. The FBG sensor-read strain is calculated at 7.74 %. The estimated errors are comparable and a reliable measurement is possible with this type of sensor. The FBG sensor strain sensitivity differs by 4.8 % from the theoretical value (see Chapter 2). Evaluated sensitivity includes the FBG response to the strain, which is applied to the composite specimen but not directly to the grating.

Uniaxial strain of attached FBG sensors

Four FBGs and one specimen were chosen for investigation in this subsection. The purpose of following research is to prove if it will be possible to attach sensors to surface for the case when embedment failed. The acrylate-recoated FBG sensors were glued to the surface of the specimen with two types of epoxy glue: X60, commonly used glue for resistive strain gauge sensors, and R&G GmbH two-component epoxy glue. Three gratings were glued with the R&G epoxy on the surface as follows: one grating in the middle and two gratings ¼ from both sides of the specimen. One FBG was glued with X60 in the middle of the specimen near those glued with R&G epoxy. This case was used to show possible creeping effects by attachment of optical fibre. All FBG sensors were covered with glue homogeneously along their length*.

The specimen fixed at both ends in the tensile testing machine was strained to 0.3 %, which corresponds to an applied load of (57.90 ± 0.03) kN and a specimen elongation of (3.2492 ± 0.0007) mm. Considerable non-linearity was observed for the FBG fixed with X60, which

* Gratings were covered of approximately 1 mm with glue.

depends on the material characteristics of this glue. Strong creeping was observed already during gluing. Afterwards, when the specimen was strained, additional creeping and slipping effects occurred, which also influenced the FBG response (see *Figure 4.26a*).

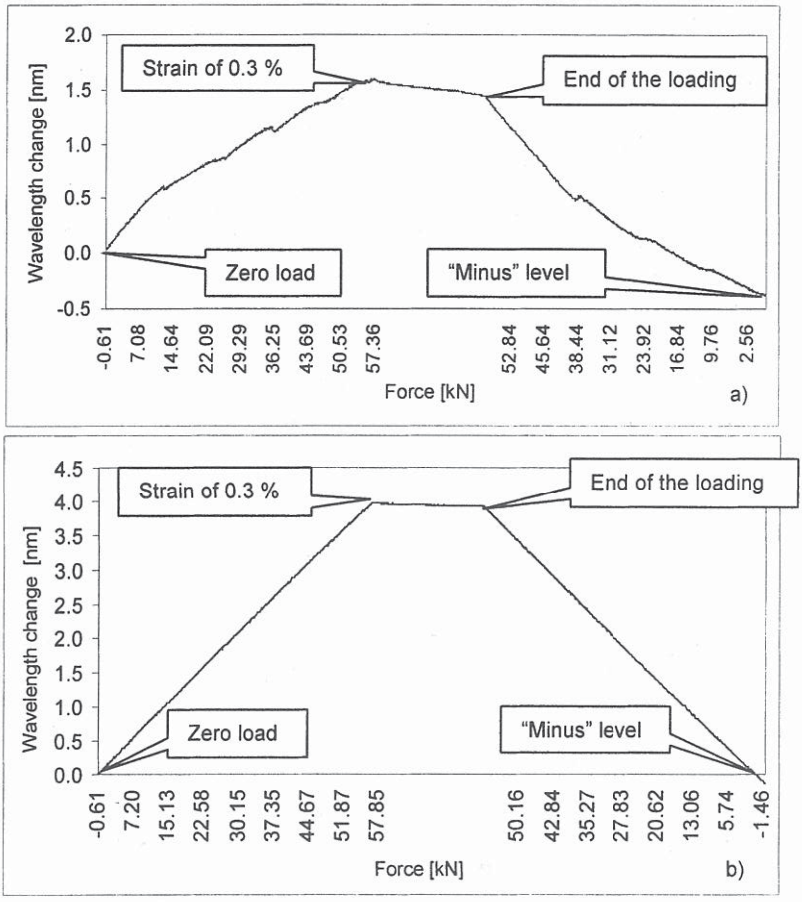

Figure 4.26: Straining of the specimen with surface-attached gratings: a) using X60 glue; b) using R&G epoxy.*

The elongation sensitivity of the FBG fixed in the middle of the specimen was (0.45495 ± 0.00002) nm/mm for X60** and (1.06804 ±0.00005) nm/mm for the R&G epoxy. The FBG sensitivity to strain applied to the specimen was (1.018 ± 0.003) pm/με for R&G epoxy. This is shown in *Figure 4.27*.

* Measurement was provided in real-time mode; 30000 measured points.

** This value is estimated between measured minimum and maximum points because of high non-linearity of the sensor response.

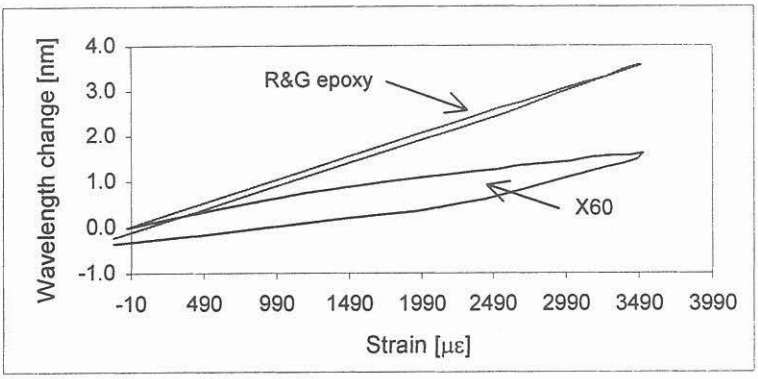

Figure 4.27: Measured dependence of the Bragg wavelength change $\Delta\lambda_B$ on the applied strain to the specimen.

The relative deviation of the data measured with FBGs fixed with R&G epoxy is 22.84 %. These gratings show lower sensitivity to strain applied to the specimen in contrast to embedded grating. However, the strain dependence has linear character. In the case if attachment of FBGs will be required for the measurement of the strain on the composite surface, R&G can be applied for small ranges of strain.

4.2 Temperature sensitivity

4.2.1 FBGs response to applied temperature changes

Temperature sensitivity of FBG sensors has been widely investigated by laboratories worldwide [Hol89], [Ala93], [Dav97], [Bra97] [Sun99], [Mac99], [Wilk99], [Bur00], [Teu00], [Mors00], [Mizu01]. This property of Bragg gratings is a subject of numerous applications in telecom and in sensor field. Temperature response of FBG sensors and networks are evaluated for different gratings types such as long-period FBG, chirped FBG, and FBG recoated with various coatings [Tru99a], [Fer99], [Ker99], [Mac99], [Wu00], [Teu00], [Liu00a], [Tru00b], [San01], [San02], [Li01], [Rao02] [Fer00], [Lee00], [Han00], [Fal97].

In the present subsection, an overview is given of results concerning thermal sensitivity of different FBGs and for different temperature ranges. It is difficult to select data for comparison from the literature, because the authors show different values as result of their work, or do not explain grating characteristics, such as thermo-optic coefficient, coefficient of thermal expansion of the fibre core, grating length, coating material, and measurement uncertainty. In general, it is possible to summarise that the dependence of the Bragg wavelength on applied temperature is nearly linear. The slope of this dependence differs for the temperature ranges of $T > 0$ °C and $T < 0$ °C. Significant deviation of the Bragg wavelength from linearity have to be expected at liquid nitrogen temperature (-196 °C) [Rei98].

Table 4.1: Temperature sensitivity of free FBGs.

Bragg wavelength	FBG thermal sensitivity [pm/K]	Temperature range [°C]
1550 nm Theoretical	13.7	-
1552 nm [Ala93]	13.7	20…160
1538 nm [Dav96]	10.18 ± 0.03	20…80
1551 nm [Dav97]	10.1 ± 0.1	25…70
1500 nm [Fal97] (chirped FBG/L = 10 nm)	13.0	0…750
1521 nm/bare [Tru01]	9.64	-50…70
1545 nm (polyimide coating) [Tru98]	10.08 ± 0.1	-50…70
1307 nm [Rei98]*	8.8	-269…77
1307 nm [Rei98]**	10.3	-269…77
1304 nm [Fer00]	10.4 ± 0.5	20…130
1530 nm (bare FBG) [Tru99b]	9.62	-60…110
1530 nm (polyimide coating) [Tru99a]	8.98	-50…190
1548 nm [Wad01]	10.3 ± 0.3	20…140

* FBG from United Technologies.

** FBG from 3M.

One reason for the non-linearity of the Bragg wavelength at low temperatures is the temperature dependence of the thermo-optic coefficient. *Table 4.1* shows data presented in literature. Reid *et al.* evaluated the thermo-optic coefficient for FBGs manufactured by United Technologies at $\frac{dn}{dT} = 9.1 \times 10^{-6}\ K^{-1}$ at a temperature of 20 °C and of $3.5 \times 10^{-6}\ K^{-1}$ for -196 °C. For FBGs manufactured from 3M the thermo-optic coefficient is evaluated at $10.7 \times 10^{-6}\ K^{-1}$ for 20 °C and $6.3 \times 10^{-6}\ K^{-1}$ for -196 °C. The thermo-optic coefficient decreases nearly by a factor of three in one case and a factor of two in the other case for a temperature change of 216 °K.

The non-linear response of recoated FBGs for the temperature range from -196 °C to 20 °C could be explained with additional stress introduced on the FBG during recoating process. Trutzel *et al.* have shown that acrylate-recoated FBG sensors show higher non-linearity at low temperatures than polyimide-recoated gratings. Investigations with polyimide-recoated FBG sensors show linear Bragg wavelength response for the temperature range from -40 °C until 70 °C and weak polarisation dependence after embedment of such sensors. For embedded FBG sensors with acrylate coating, large polarisation dependence of the Bragg wavelength was found induced by geometry changes of the embedded fibre. In this case, it is important to take into consideration temperature-dependent birefringence induced by intrinsic stress within a FBG sensor and residual stress after embedment.

For evaluation of temperature dependence of the FBG wavelength, linear approximation is usually used. Reid *et al.* and Trutzel *et al.* have shown that this approximation is valid only for ambient temperatures.

Table 4.2: Temperature sensitivity of the embedded FBG sensors.

FBG wavelength [nm]	FBG coating	Host material	FBG thermal sensitivity [pm/K]	Temperature range [°C]
835 nm [San01]	-	Nickel	21	500...560
845 nm [San02]	-	Nickel	19.6	500...560
1530 nm [Tru98]	polyimide	CFP	11.6 ± 0.04	-50...100
1300 nm (after temperature cycles) [Li01]	-	Nickel	23.7 21	20...260
1529.981 nm [Tru01]	ORMOCER®	Aluminium	34.52	-60...200
1535.594 nm [Tru01]	ORMOCER®	quasi-isotropic CFP	11.41	-60...200
1535.762 nm [Tru01]	ORMOCER®	quasi-isotropic CFP	10.66	-60...200
1545.174 nm [Tru01]	polyimide	quasi-isotropic CFP	8.47	-60...200
1535.355 nm [Tru01]	polyimide	quasi-isotropic CFP	8.32	-60...200

4.2.2 Embedded FBGs

The purpose of investigations in this subsection is the evaluation of embedded FBG sensors during three temperature cycles in the range from -40 °C to 60 °C and the comparison of FBG characteristics before and after temperature cycling. The temperature steps for one cycle are shown in *Table 4.3*. The cycle duration was approximately 12 hours.

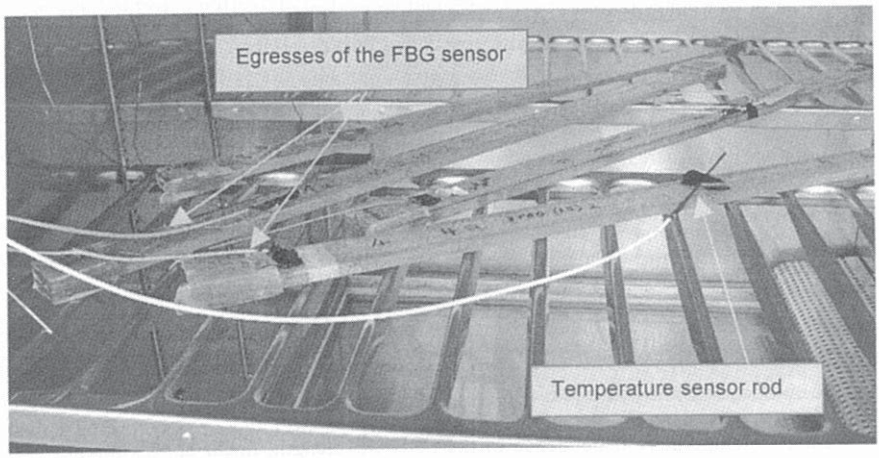

Figure 4.28: Samples inside the temperature chamber.

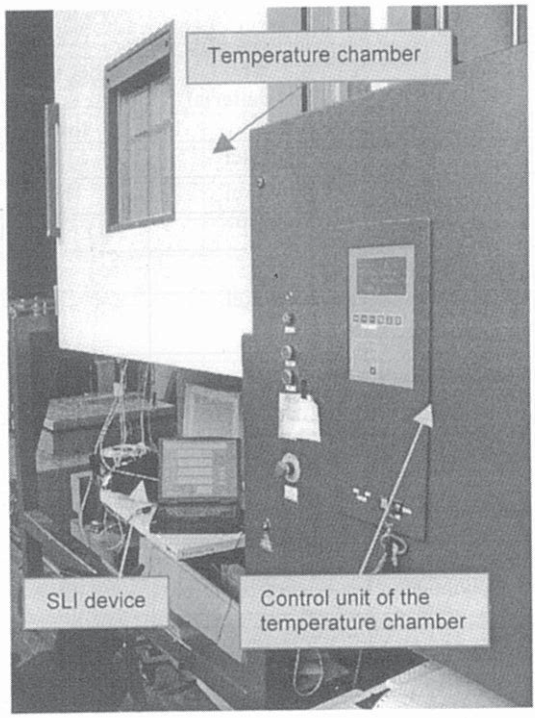

Figure 4.29: Measurement set-up.

Figure 4.29 shows a temperature chamber in which the temperature cycles were controlled according to *Figure 4.30*. In order to measure the temperature near the surface of chosen samples, a special temperature sensor rod was applied. *Figure 4.30* shows the temperature cycle measured with the climate chamber sensor and with the temperature sensor rod. The standard uncertainty of the measured data are ± 0.02 °C for the temperature chamber sensor and ± 0.01 °C for the sensor rod.

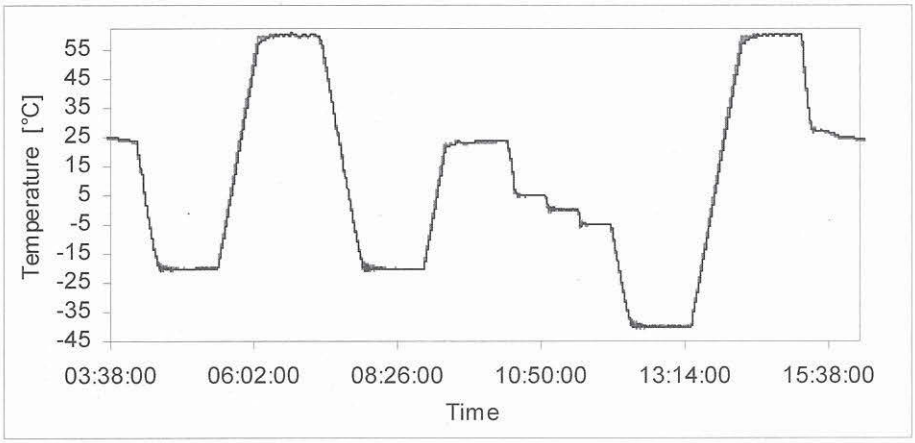

Figure 4.30: One temperature cycle measured with the climate chamber sensor and with the temperature sensor rod.

Figure 4.31 shows the temperature response of four FBG sensors. The mean deviation of measured grating wavelengths was ± 16 pm. Response of all three FBG sensors at the same values of temperatures shows good reiteration. The thermal sensitivity is evaluated at (17.907 ±0.005) pm/K. This value is found for the whole temperature range from -40 °C to 60 °C.

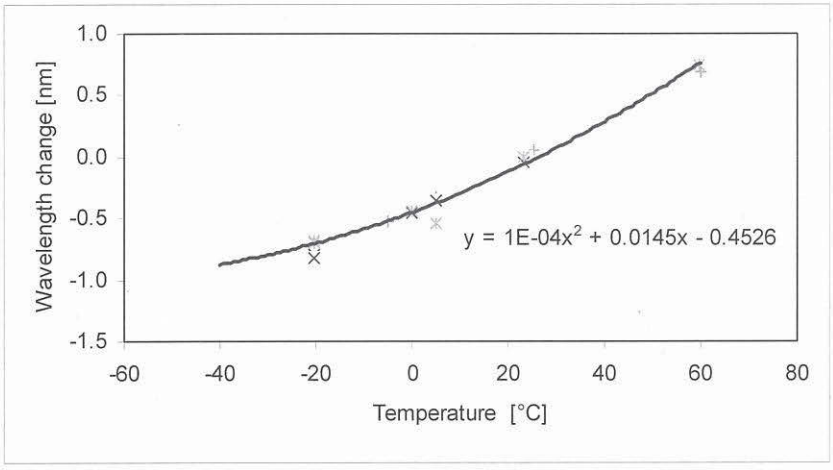

Figure 4.31: Response of four FBG sensors to temperature change.

Figure 4.32 shows the Bragg wavelength change of one of the sensors during the temperature cycles as shown in *Figure 4.30*. The Bragg wavelength splitting was observed at -40 °C only for one of the investigated sensors. The reason for this can be a larger intrinsic stress inside the FBG at low temperatures, since the FBG is placed between reinforcing textures (see *Figure 4.16*). *Figure 4.17* shows typical undulations in the internal structure of the composite cross-section. The FBG sensor inside such structured material is additionally subjected to periodical local transverse loads by crossings of the reinforcing fibre bundles. It is impossible to predefine the FBG sensor position inside this composite precisely and, therefore impossible to avoid such influences inside this structure.

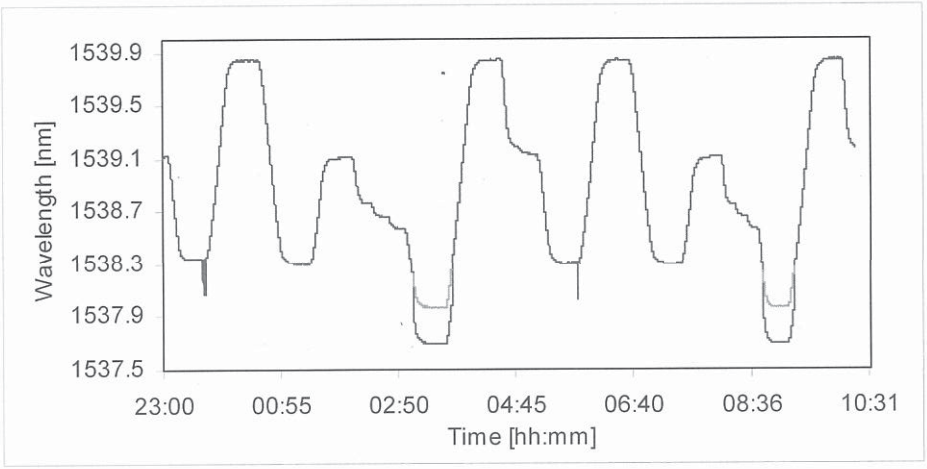

Figure 4.32: A real-time measurement of the Bragg wavelength during two temperature cycles.

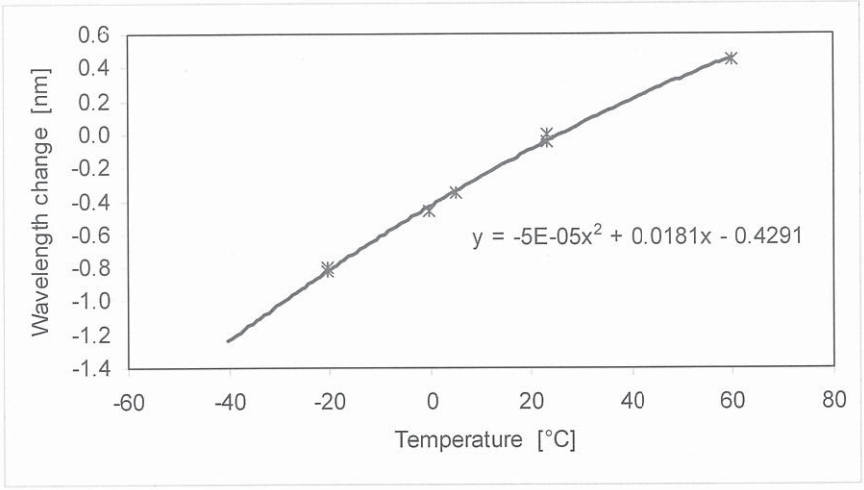

Figure 4.33: Bragg wavelength changes of the FBG that shows the peak wavelength splitting at T = -40 °C.

Figure 4.33 shows the Bragg wavelength changes of this FBG at temperature changes. As analysed in the previous subsection, the FBG thermal sensitivity at low temperatures can differ from the sensitivity near room temperature.

In order to avoid an evaluation mistake, it is important to consider and analyse obtained data in two parts $T > 0$ °C and $T < 0$ °C. The curve fittings for temperatures $T > 0$ °C show linearity and their slopes are similar for every sensor. The mean thermal sensitivity for four FBG sensors in the temperature range from 0 °C till 60 °C is (18.8 ± 0.1) pm/K.

The thermal sensitivities of two of the investigated sensors for temperatures $T < 0$ °C are (17.19 ± 0.55) pm/K and (18.06 ± 0.77) pm/K. The curve slopes of temperature sensitivity for these sensors are different and both differ definitely from those for temperatures $T > 0$ °C. The uncertainties in both cases are high and can be explained by the temperature sensor uncertainty as well as by the non-linearity of the temperature dependence at lower temperatures even if it was only -40 °C. For comparison, the thermal sensitivity of one of sensors for temperatures $T > 0$ °C is (19.46 ± 0.12) pm/K and for temperatures $T < 0$ °C is (17.52 ± 0.02) pm/K.

It should be noted that the thermal sensitivity of FBGs obviously depends on the position of the sensor in the laminated material. If there is no possibility to achieve an appropriate position of the sensor inside the composite material, only average sensor sensitivity to temperature changes can be taken into consideration.

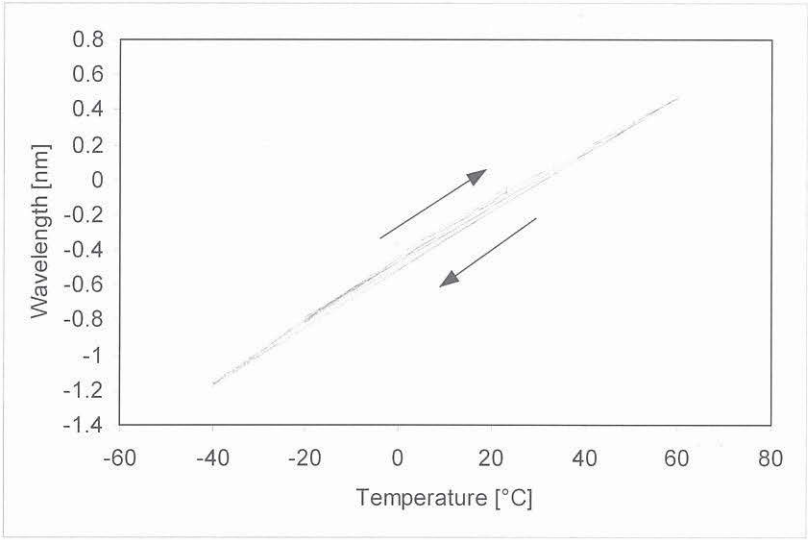

Figure 4.34: The Bragg wavelength dependence on the temperature for a number of cycles.

Table 4.3 shows the calculated thermal sensitivity coefficient for one of the investigated gratings for different temperature steps. The small difference can be observed also in the thermal sensitivity coefficient K_T calculated from measured data.

Table 4.3: K_T of the FBG (1530.73 nm) for several temperature steps.

No.	K_T [10^{-6} /K]	Temperature range [°C]
1.	11.606 ± 0.3606	23…-20
2.	12.751 ± 0.4876	-20…60
3.	11.867 ± 0.3445	60…-20
4.	13.402 ± 0.6618	23…5
5.	12.479 ± 0.2535	5…0
6.	12.31 ± 0.472	0…-5
7.	11.781 ± 0.1276	-5…-40
8.	12.792 ± 0.3527	-40…60
9.	12.129 ± 0.1354	23…-20

The temperature investigations revealed apparently very little hysteresis, which is less than the uncertainty of the temperature controlling of the climate chamber (*Figure 4.34*). The small decrease in the characteristics should be traced back to the drift of the climate chamber.

4.3 Bending of FBGs

The purpose of the following investigation is to evaluate the bending influence on simple free FBGs, attached FBGs, and embedded FBGs. A short FBG responds to small bending radii, which can cause significant signal attenuation. However, it is difficult to investigate this in practice. In real applications, this situation arises, for example, when gratings are embedded into composite materials.

4.3.1 Uniform bending of free gratings

Some authors provided investigations of bending influence, but usually with long-period gratings (LPFBG) [Ber00], [Gon01], [Pra02]. Such gratings respond to larger bend radii, which make investigations easier. Gonzalez *et al.* noticed that considerable changes in a LPFBG spectrum occur at a bending radius < 30 mm. For a usual short FBG, this value is expected to be smaller. It is also important to note that a Telecom single mode fibre shows significant bending attenuation of 0.5 dB for a bend radius of approximately 17 mm [Corni02].

Bending-induced spectral changes of uniform standard FBGs (1533.8 nm and 1547.9 nm), which are wrapped around mandrels with defined diameters, were investigated. In order to record the spectral characteristic changes of the FBGs, a broadband source, a polariser, a polarisation controller, and an optical spectrum analyser were used. There were expected to register a light loss in the bent area of the fibre, a FBG spectrum broadening and a Bragg wavelength splitting.

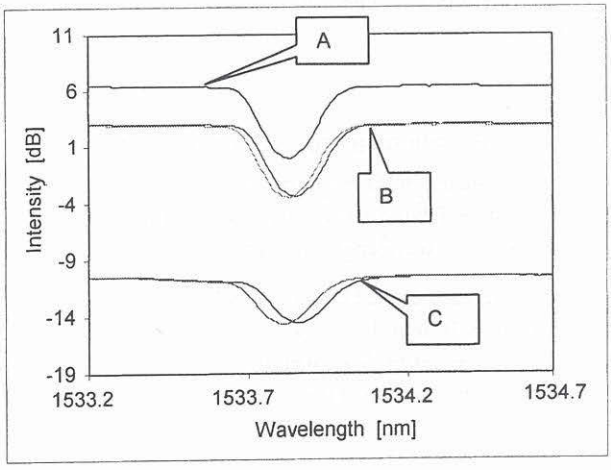

Figure 4.35: FBG transmission spectra at bending influence: without influence A; the bending radius is 6 mm B ($\Delta\lambda_{bending}$ = 49 pm); the bending radius is 2.5 mm C ($\Delta\lambda_{bending}$ = 64 pm).

Noticeable changes in the FBG spectrum occurred at radiuses below 6 mm and significant changes in the transmitted FBG signal were observed starting from the bending radius of 2.5 mm. A small shift of the central Bragg wavelength $\Delta\lambda_{avg} = (49 \pm 8)$ pm was recorded for a bending radius of (6 ± 0.1) mm. For a bending radius of (2.5 ± 0.1) mm, this shift was

$\Delta\lambda_{avg}$ = (64 ± 8) pm. These correspond to signal attenuation of 3 dB and 14.59 dB respectively (see *Figure 4.35*). A broadening of the transmitted signal was also noticed. For a bending radius of 6 mm, the spectral width differs from the uniform case of 15 pm and for a radius of 2.5 mm, the difference is 115 pm. Polarisation measurements shown that a distance between two polarisation peaks at bending radius of 6 mm is $\Delta\lambda_{diff} \cong 46$ pm and at 2.5 mm is $\Delta\lambda_{diff} \cong 55$ pm.

It was complicated to carry out reliable measurement for very small bending radii without damage of the FBG. For this reason, the data in this subsection are provided as a source for comparison with other investigations. Summarising the results, beside the signal attenuation in the system it has to be taken into consideration that there is also attenuation induced by the FBG. The grating usually responds to the critical bending radii with a birefringence effect and a signal broadening. Bending-induced geometry changes of the fibre and grating explain these effects. The strain ε in the bent fibre with radius R_b is given by

$$\frac{1}{R_b} = -\frac{\varepsilon}{h} = \frac{1-\cos\left[\frac{L}{2R_b}\right]}{h}, \tag{4.1}$$

where L is the fibre length, h is the distance of the bend area from the neutral axis [Gon01], [Pra02]. Along this formulation, for a bending radius of 2.5 mm, estimated bending-induced strain on the strain side of the optical fibre is 1640 με. The change in the refractive index along the transverse coordinates of the bent fibre in the result of the stress induced by bending, causes modification of modal distribution of the modes in the bend. This birefringence introduces also a shift of the grating wavelength.

4.3.2 Bending behaviour of gratings attached to a bent cantilever beam

A FBG sensor attached to a structure surface can be subjected to flexure influences. In such a case, an FBG experiences, besides flexure stress, stress induced by the material which glues or fixes it on a surface, which produce a wavelength shift and a chirp of the main peak.

The following investigation have been carried out on a flexible composite plate 980 mm long with rectangular cross-section 50 mm x 10 mm. It was fixed at one side, while the other side was bent to a defined deflection Δd (see *Figure 4.36*). According to the bend characteristics for a slab chucked on one end, the strain on the surface of the sample at a certain position z follows from

$$\varepsilon(z) = \frac{3}{2}\frac{\Delta d \cdot h}{L^3} \cdot z, \tag{4.2}$$

where z is a variable value along the longitudinal axis of the beam and L is the length of the specimen.

Three commercially fabricated gratings (1529.6 nm, 1539.55 nm, 1549.7 nm) for sensor application were used. They were spliced together into an array and afterwards attached to the surface of the plate along its axis. Each FBG is attached using two-component epoxy glue along its full length. The response from the FBG sensors was measured with a broadband source and an optical spectrum analyser.

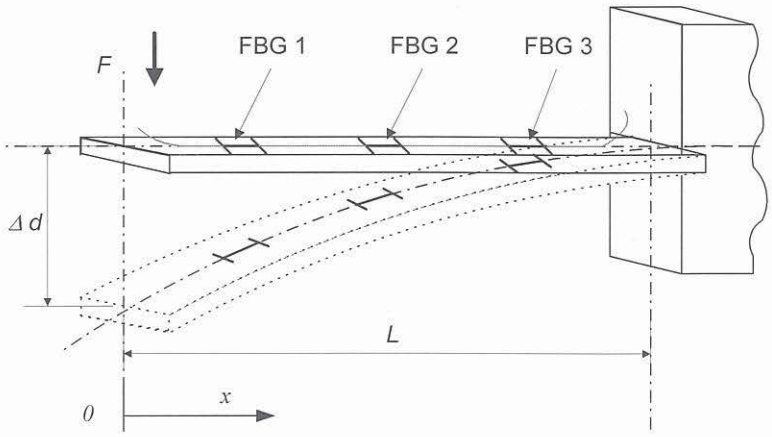

Figure 4.36: Schematic representation of the experiment with the cantilever composite beam.

Applying the load F, one side of the material is in the tension zone, the other in the contraction zone. If the grating is attached in the tension zone, it will be strained. This case differs from the bending of the bare grating, because here the attached sensor will be influenced by fixing on the surface of material and will sense increasing strain distribution along the length of the grating, which produces chirp of the FBG main peak.

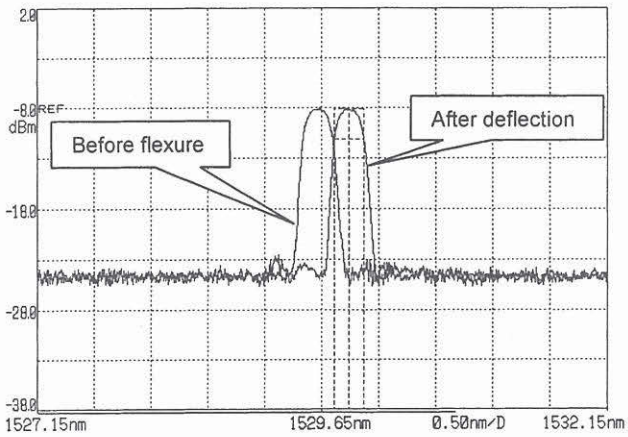

Figure 4.37a: Reflection spectra of attached FBG sensor No. 1 before flexure of cantilever beam and after deflection of 65 mm.

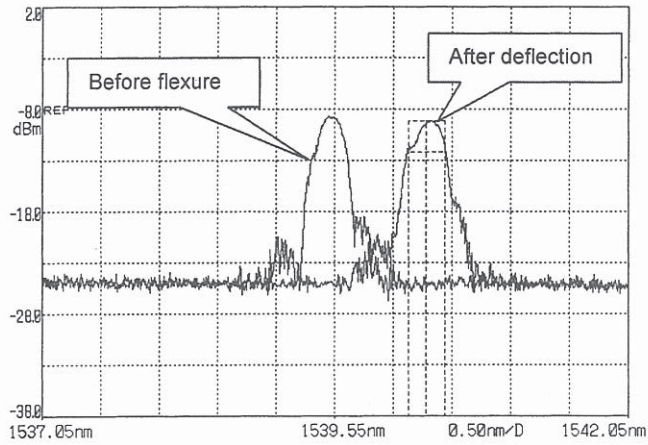

Figure 4.37b: Reflection spectra of attached FBG sensor No. 2 before flexure of cantilever beam and after deflection of 65 mm.

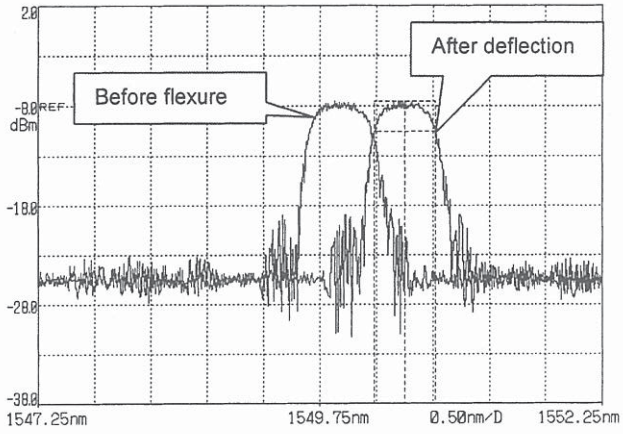

Figure 4.37c: Reflection spectra of attached FBG sensor No. 3 before flexure of cantilever beam and after deflection of 65 mm.

Figure 4.37 (a) to (c) shows changes in the reflection spectra of three FBG sensors before and after flexure of the cantilever beam with a deflection of 65 mm, which corresponds to a bending radius of R_b = mm. At this deflection, FBGs show wavelength shift which correspond to the grating elongation by (0.5 ± 0.03) µm (Sensor 1), (1.5 ± 0.03) µm (Sensor 2), and (1.39 ± 0.02) µm (Sensor 3). This corresponds to the intra-grating strain of 247 ± 15 µε, 758 ± 17 µε, and 695 ± 11 µε for the three sensors. In this particular case of the plate flexure with small deflection there was no chirp effects observed.

Values of the strain influencing the FBG directly at flexure of the beam are comparable with the mechanical data calculated where the FBG sensors are positioned on the beam surface (see *Figure 4.38*). Estimated relative deviation between theoretical and experimental data was 15 %.

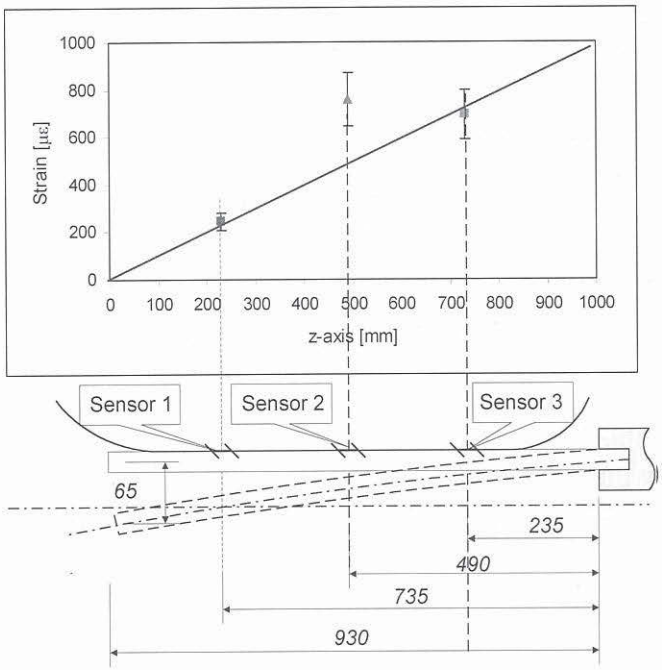

Figure 4.38: Schematic representation of the experiment with the cantilever composite beam.

In this case, FBGs operated as localised sensors. The chosen sensors allow reliable evaluation of the strain distribution on the surface of the cantilever beam with the exception of the Sensor 2 positioned in the middle of the beam. This sensor is exposed to a larger strain as predicted from calculation. This is explained with an error of an attachment technique, where two-component epoxy glue is used. FBG is covered with a 1 mm thick epoxy layer. In this particular case, epoxy shown a small crack and was partially detached from the surface which caused a larger stress to the grating due to the not proper adhesion with the beam surface.

4.3.3 Bending behaviour of gratings embedded in a bent cantilever beam

An example of embedded FBGs, placed between reinforcing layers in the composite material is described in detail in subsection 4.1.3 (see *Figure 4.16*). The SEM microphotograph of the composite cross-section has shown that the possible bending radius of the embedded grating is approximately 1.8 mm (see *Figure 4.39*). As shown in subsection 4.3.1, this value is critical and can cause signal failure.

Three FBG sensors (1546.351 nm, 1552.52 nm, 1556.744 nm) spliced to each other and embedded into the composite material (described in subsection 4.1.3) will be considered here. The FBG

response to a flexure of the composite beam was investigated. Depending on the position of FBGs according to the zero axis of the beam, they will experience contraction or tension. Depending on the distance to the fixed edge of the beam, they will sense different strain values. Schematic representation of the bent area is given in *Figure 4.40*.

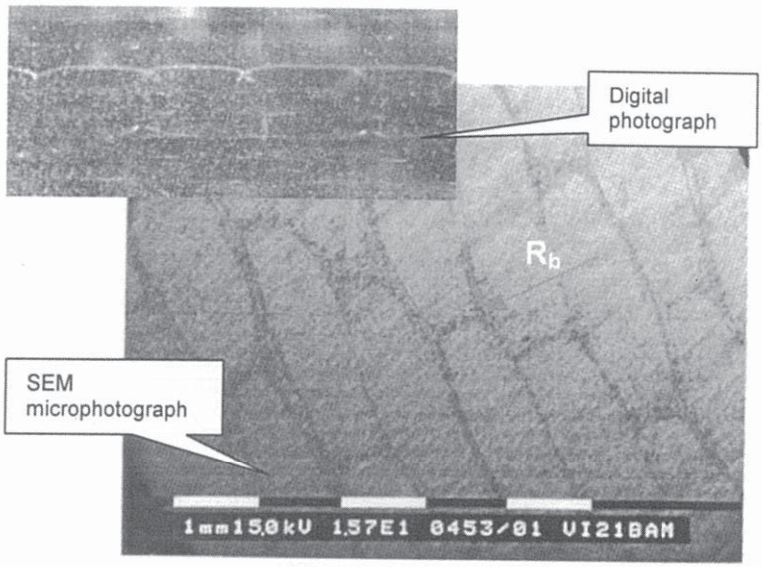

Figure 4.39: Images of the composite cross-section.

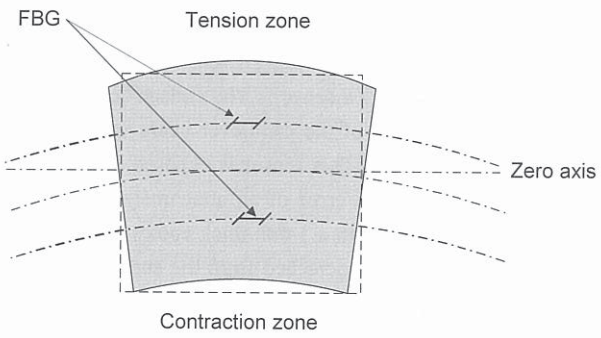

Figure 4.40: Bending of the material area, where FBG sensors are embedded.

Flexure investigations were carried out with the cantilevered composite beam as shown in *Figure 4.36*. *Figure 4.41* shows examples of transmission spectra of three FBG sensors for a cantilever beam with a deflection of 40 mm. FBG sensors respond in one case for strain and in the other for contraction. Maximal applied deflection to the beam was 50 mm.

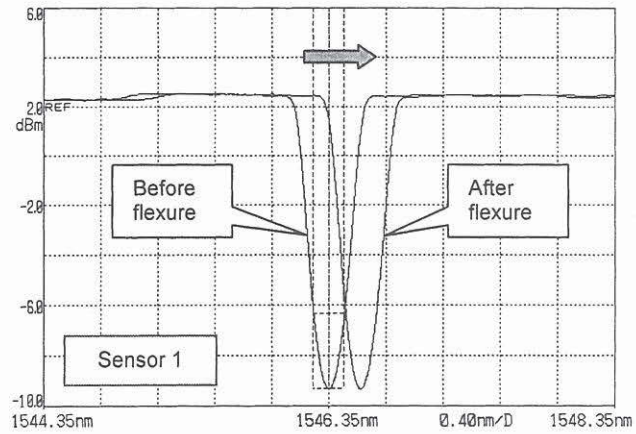

Figure 4.41a: Transmission spectra of embedded FBG sensor No. 1 before flexure of the composite beam and after deflection of 40 mm.

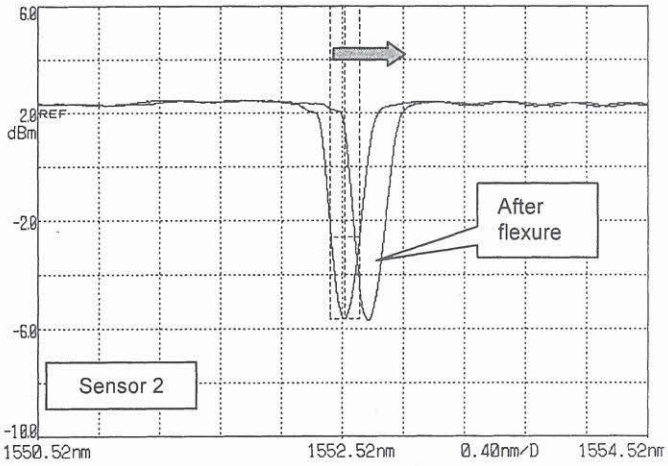

Figure 4.41b: Transmission spectra of embedded FBG sensor No. 2 before flexure of the composite beam and after deflection of 40 mm.

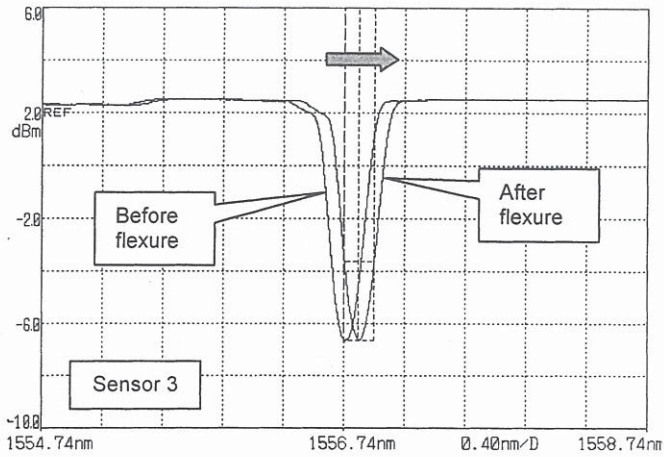

Figure 4.41c: Transmission spectra of embedded FBG sensor No. 3 before flexure of the composite beam and after deflection of 40 mm.

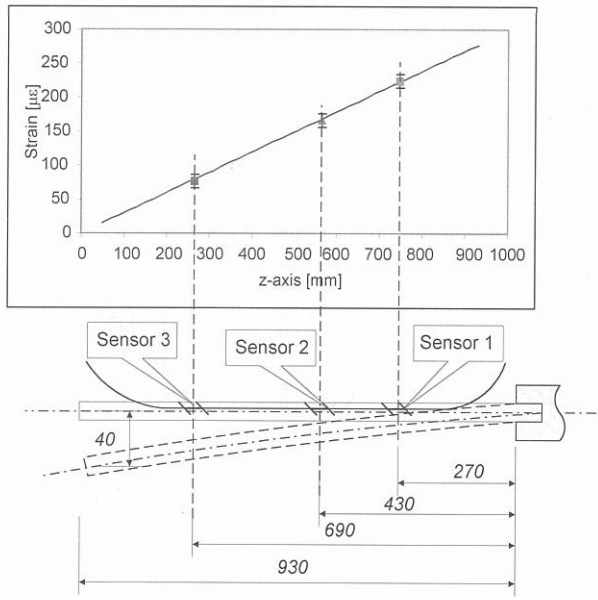

Figure 4.42: Strain distribution inside the composite material close to the zero-axis for a deflection of 40 mm.

Figure 4.42 shows the strain distribution inside the plate approximately 2 mm from the zero-axis. Calculated strain distribution is shown in comparison with the strain measured with embedded FBG sensors. At the deflection of 40 mm, the maximum strain is about 200 με. A relative deviation of measured and calculated data of 1.8 % was estimated.

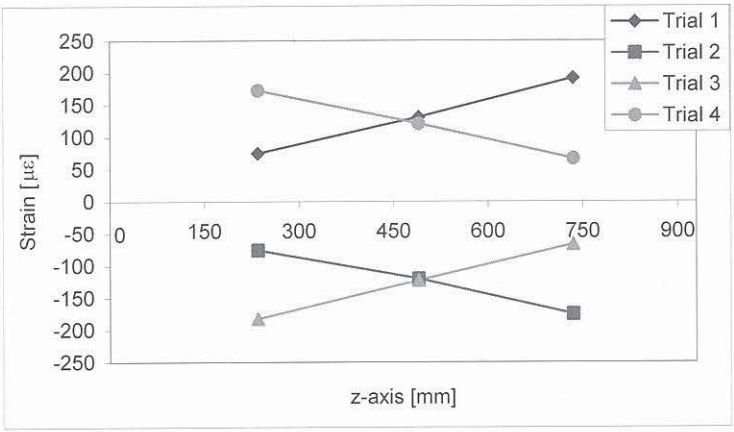

Figure 4.43: Strain-contraction response of three embedded FBG sensors.

Table 4.4: Strain values (με) for 3-FBG array sensor at cantilever bending of the composite beam.

	Strain με		
	Sensor 1	**Sensor 2**	**Sensor 3**
Trial 1	68.193	105.571	164.054
Trial 2	-74.766	-117.846	-173.032
Trial 3	-179.932	-120.301	-66.111
Trial 4	170.073	118.665	62.030

The measured response of three FBGs in the tension zone (Trial 1) and contraction zone (Trial 2) are shown in *Figure 4.43*. This investigation was provided to ensure that an embedded FBG sensor work reliably. The same procedure was repeated with the same cantilever beam fixed from the other side (Trial 3 and Trial 4). The sensor responses show relative good reiteration. Data of bending-induced strain for these trials are in Table 4.4.

4.3.4 Bending behaviour of gratings centrally embedded in a three-point bent beam

FBG sensors embedded into a composite plate with dimensions of 840 x 370 mm were investigated at three-point flexure (see *Figure 4.44*). Three FBG sensors were placed approximately 2 mm from the surface of the plate and positioned side by side.

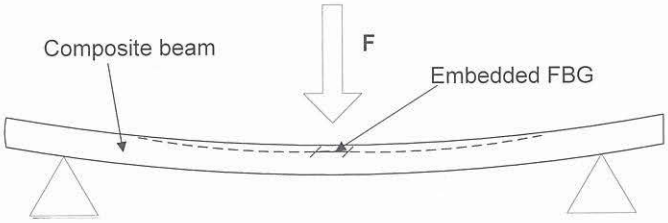

Figure 4.44: Schematic representation of experiment.

The reflection spectrum of one of the embedded sensors before and after embedment is shown in *Figure 4.45*. Small changes in the central wavelength of the sensor and small increase of the sideband were observed after embedment.

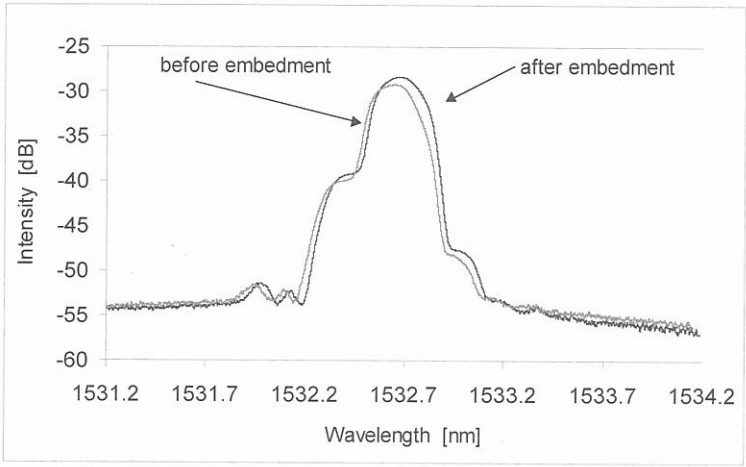

Figure 4.45: Reflection spectra of the FBG (provided by J. Peupelmann) before and after embedment into a CRP composite.

Figure 4.46 shows the FBG response under three-point flexure of the composite plate (central loading). The maximum flexure-induced strain in the middle of the plate surface is -51.95 με. For maximum deflection of the plate, the FBG wavelength shift is -0.22 nm.

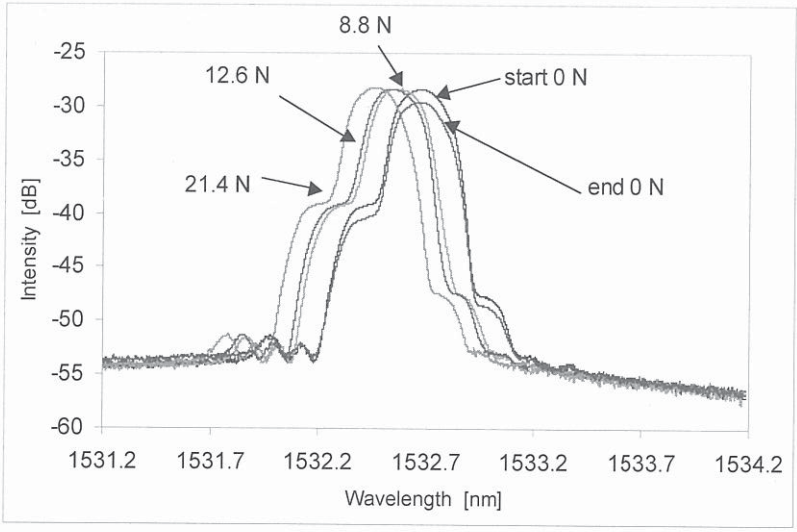

Figure 4.46: Reflection spectra of an FBG sensor (provided by J. Peupelmann) embedded into a composite plate under three-point flexure.

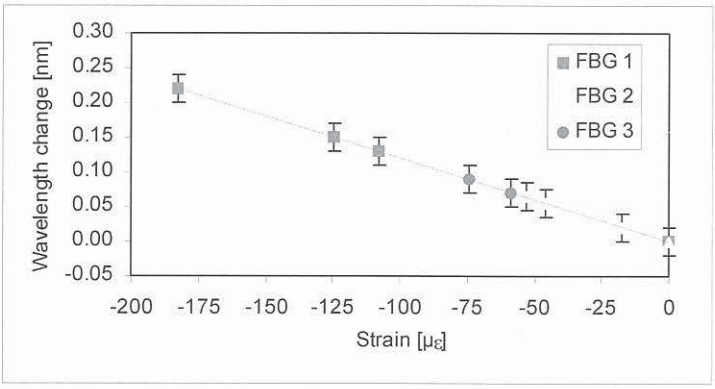

Figure 4.47: FBG sensors strain during bending of the plate.

No significant changes were observed in the bandwidth or intensity level of the reflected signal. A transverse load occurring at the flexure of the plate induced a sideband increase. The estimated transverse strains affecting the grating additionally at maximum flexure, were $\varepsilon_x = 211.7$ με and $\varepsilon_y = 61.04$ με. *Figure 4.47* shows the dependence of the sensor wavelengths on applied bending-induced strain. Sensor responses showed good linearity and reiteration.

4.4 Transverse stress influence

A load transverse to the grating axis is expected to cause some problems in signal demodulation, especially when FBG sensors are integrated into a sensor housing or are embedded. This problem is the subject of numerous investigations [Hoc79], [Sny81b], [Kum84], [Ber88], [Tsa92], [Nod86], [Marc91], [Ebe92], [Kim92], [Stee95], [Law95], [Wag96], [Mas97], [Gaf00], [Gue02]. Such investigations are mainly focused on the influence of uniform transverse load onto the long FBG. Typical changes in a FBG spectrum induced by transverse load are signal attenuation, wavelength shift, broadening of the spectrum, increase of sideband, and birefringence. Such changes to the signal can be explained by increased intra-grating stress, geometry changes, and appearance of mini-cracks, especially when it is embedded inside a non-homogeneous matrix. Nevertheless, such undesirable mechanical influences as transverse stress also affect transmitted or reflected signal of a usual short sensor grating. In the following subsections, transverse load influence on the grating behaviour is presented.

4.4.1 Transverse stress applied to free FBGs

Two standard FBGs designed for sensor applications were used for the investigation (1533.8 nm from Ingenieurbüro Jens Peupelmann and 1547.8 nm from AOS GmbH). Gratings were positioned on the surface of polished supporting-plate and covered with the 8 cm long plate (see *Figure 4.48*). Various calibrated weights of approximately 3 kg each were placed above one after another. In order to evaluate grating characteristics, a broadband source, a polarizer, an optical spectrum analyser and a polarisation controller were chosen (see *Figure 4.49*). It is possible to record an applied transverse force and the related polarisation states of transmission spectrum of the FBG sensor by using such an experimental set-up. Investigations were provided under climate room conditions to avoid other influences on the FBG signal.

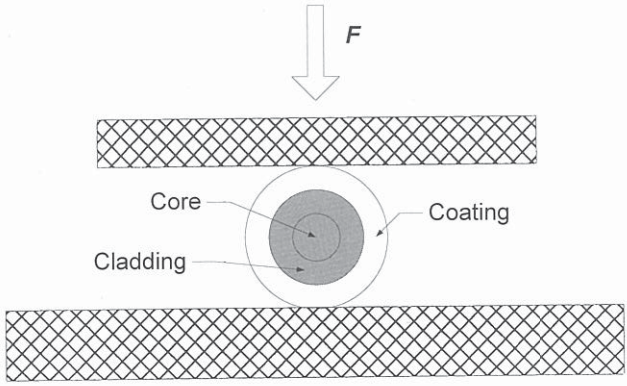

Figure 4.48: Schematic representation of experiment procedure.

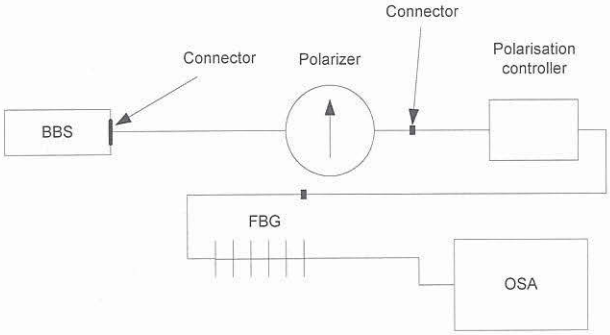

Figure 4.49: Schematic representation of measurement scheme to measure separation of two peaks at transverse loading.

Figure 4.50 shows spectra of an unstressed FBG and a FBG stressed with a transverse load. *Figure 4.50* shows two peaks ($\Delta\lambda_{diff}$ = 0.043 nm) measured at transverse loading of the FBG with transverse load of (12.9 ±0.004) N.

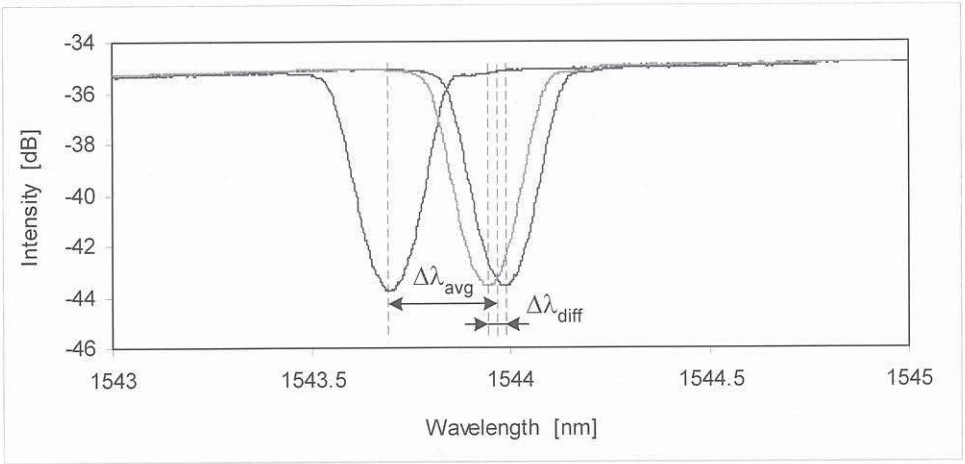

Figure 4.50: Transmission spectra of FBG investigated under transverse loading.

Several effects can be observed in the FBG spectrum shape after loading: a general central wavelength shift $\Delta\lambda_{avg}$ = 0.325 nm, a distance between two polarisation peaks $\Delta\lambda_{diff}$ = 0.043 nm, and attenuation by 0.36 dB of the grating reflection. If linear distribution of the load along the grating length is considered, transverse strains in the grating area can be estimated along the elasticity theory [Fro48] to be ε_x = 173.7 με and ε_y = 50.07 με.

Significant changes in FBG transmission spectrum were observed starting from the load values of 13 N for some gratings.

4.4.2 Point-wise transverse load onto FBG

Point-wise effects could also induce considerable influence or even damage the FGB sensor. During or after embedment of FBG sensors into some special-structured composites local point-wise indentation could cause tremendous changes in the sensor signal shape, which make the signal analysis impossible or complicated. The effect of small transverse load influence in the area of the long-period grating was already investigated by some authors [Mas97], [Tru01], [Nog02], [Tor02], [Gue02]. This sub-section focuses on this effect, taking into consideration the influence of point-wise transverse indentation applied to uniform short-period FBGs. The loading area is smaller than the FBG length.

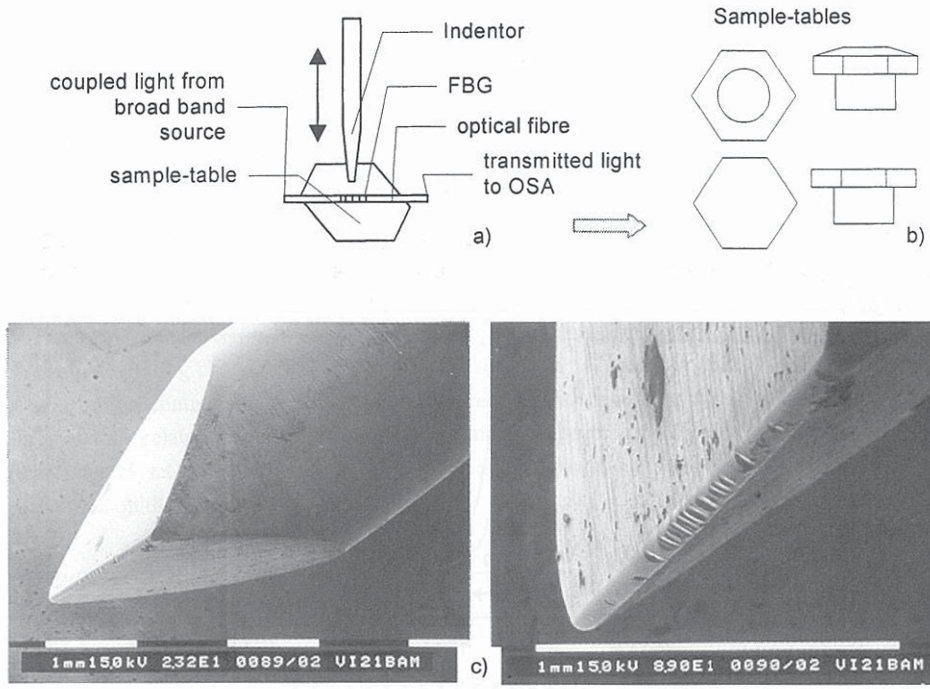

Figure 4.51: Schematic representation of indentation experiment: a) indentation procedure; b) design of the sample-table; c) design of the indenter.

A special micro-mechanical indentation-testing machine was chosen to investigate point-wise indentation influence on the FBG [Kali97]. *Figure 4.51* shows the investigation procedure. The optical fibre with FBG was fixed on the surface of the sample-table to avoid bending of the fibre during pressing with the indenter. Chosen requirement for fixing mechanism is ensuring the close contact of the fibre with the surface of the sample-table. The fibre was prestrained and glued with epoxy at two points outside the FBG area. Several fixing methods were chosen for different situations which could be met at fixing or embedment of the fibre, e.g. firmly or slightly fixed, or pre-strained fibre. Afterwards, the table was positioned under an indenter and the grating was pressed with an indenter in a step-wise mode (see *Figure 4.52*).

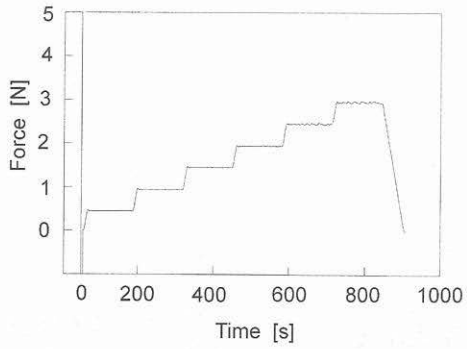

Figure 4.52: Example of the step-wise mode of the indentation till 3 N.

Standard short Bragg gratings manufactured for sensor application were used for investigations. Only approximately of 3 % of the grating length was subjected to the indentation. Investigations were provided with recoated and bare gratings to evaluate stress applied by the coating on the fibre. The acrylate-recoated FBG was fixed on the small sample-table (see *Figure 4.51b*) first with two flexible fixing points and then with two-component epoxy glue along its whole length. *Figure 4.53a* shows a digital photo of the recoated edge of the FBG made under the microscope. A damaged area remained after recoating, which makes this place weaker towards the stress than the rest of the fibre. Trutzel *et al.* have shown that embedded, acrylate-recoated FBG sensors show poor linearity during temperature-strain investigations.

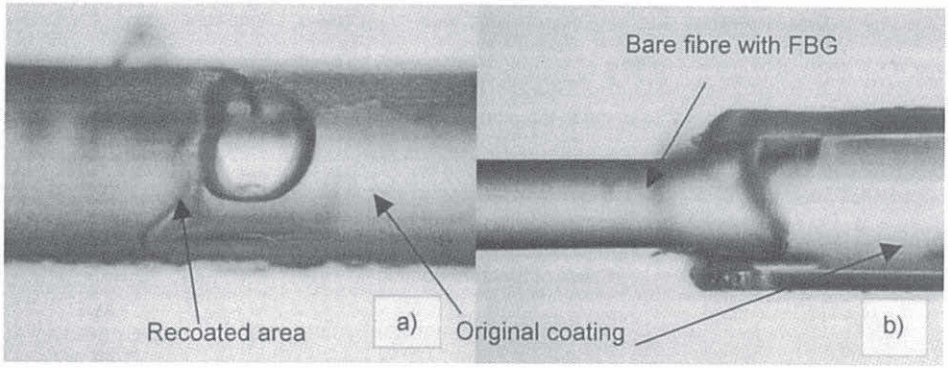

Figure 4.53: Photos of the optical fibre with FBG: a) interface of original fibre coating to the recoated area; b) bare grating.

Transverse stress in the middle of the slightly fixed recoated FBG

When FBG is slightly fixed on the sample-table with two flexible fixing points, there is microbending additionally to the point-wise indentation. Also, on pressing, the fibre slips under the indenter, which introduces errors in recorded data. To avoid this, the fibre was prestrained and then fixed. *Figure 4.54* shows reflected FBG spectra recorded before and after indentation. The FBG reflected signal attenuation of 33.82 dB and small wavelength shift of 0.2 nm were observed.

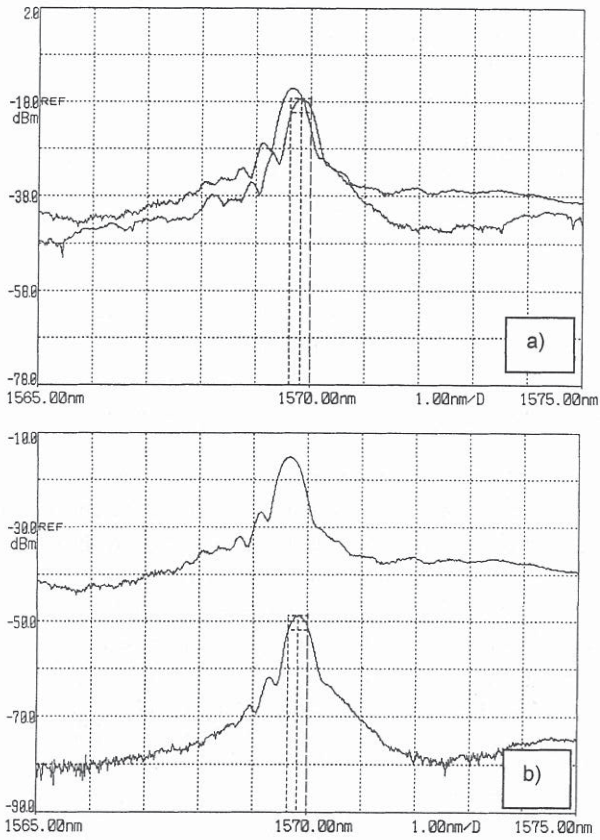

Figure 4.54: Reflection spectra of FBG sensors exposed to the point-wise local load: a) 4 N; b) 10 N.

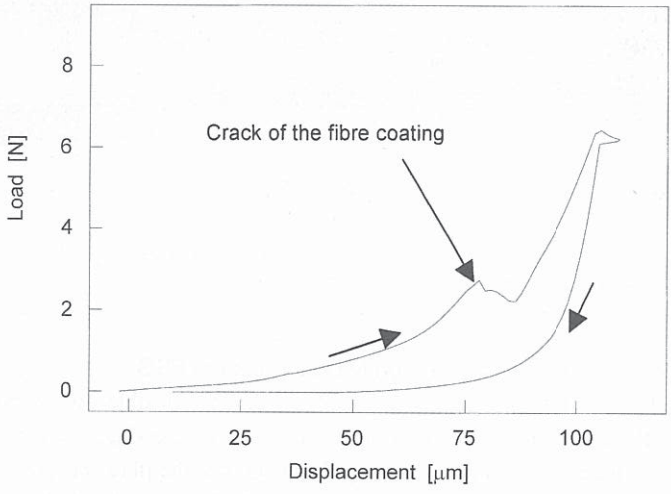

Figure 4.55: Dependence of applied transverse load on displacement of indenter.

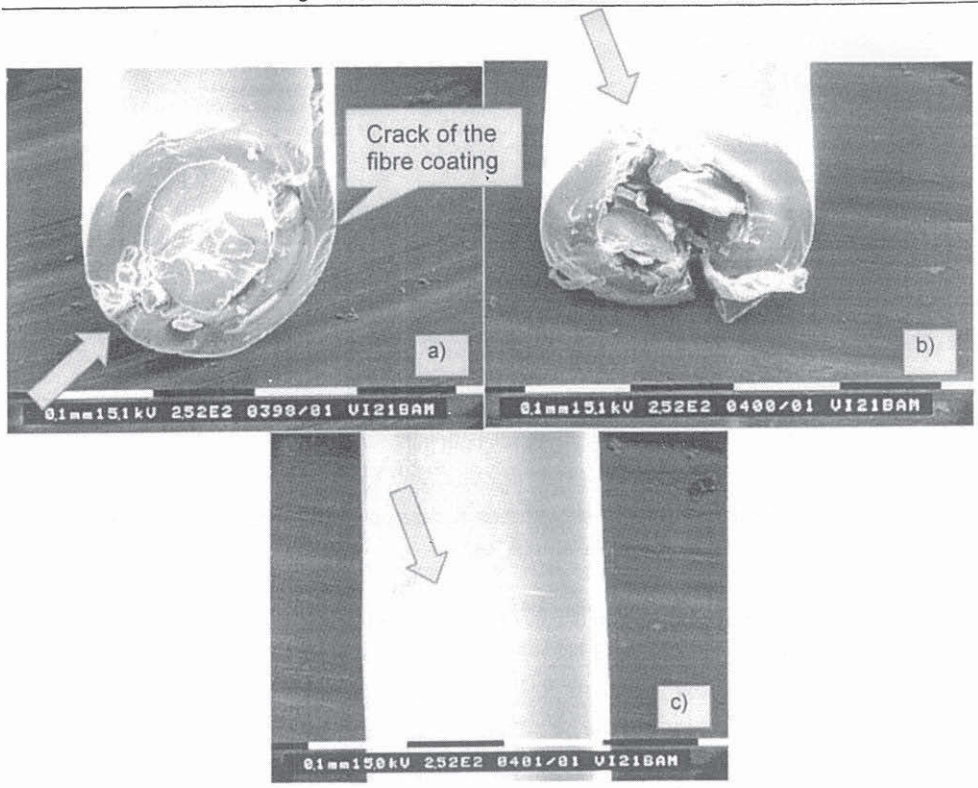

Figure 4.56: Photos of the crashed recoated FBG after point-wise loading: a) right edge of the fibre; b) left edge of the fibre; c) scratch on the fibre coating of prestrained fibre.

A small crack develops in the middle of the recoated area of FBG sensor after 9 N of applied transverse load. SEM-photographs of damaged area are shown in *Figure 4.56*. Direction of the transverse load application is marked with arrows. A longitudinal crack in fibre coating occurs on the bottom, where the fibre is in contact with the sample-table, along the fibre length. Some residual changes in the fibre geometry were noticed (see *Figure 4.56a*).

Transverse stress in the point nearby the centre of the slightly fixed prestrained recoated FBG

To avoid fibre slipping and bending under an indenter, the FBG was prestrained and then fixed at both ends. When the FBG is pressed with a load of 3 N at a point near the centre of the grating, the central wavelength shifts by 8 pm and the general attenuation of the signal occurs of 0.35 dB.

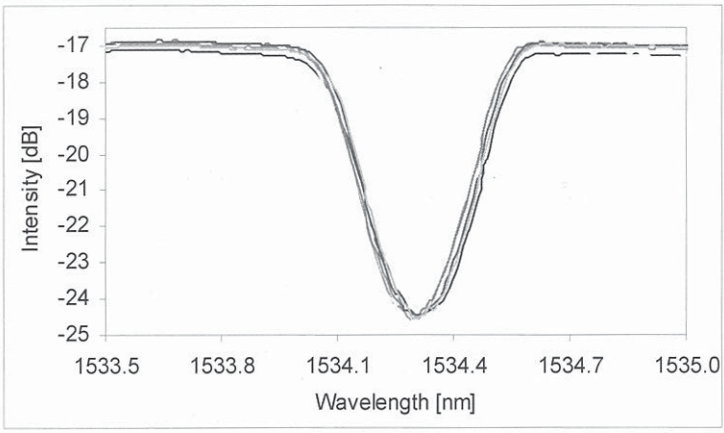

Figure 4.57: Transmission of the FBG sensor at transverse point-wise indentation near the FBG centre till 3 N.

No appreciable changes were observed in the shape of the FBG transmission spectrum at pressing of the prestrained FBG near its centre until 3 N.

Transverse stress of the firmly fixed bare FBG

A bare FBG was chosen for further investigations to provide a straighter position of the fibre on the sample-table and avoid microbending and slipping under the indenter. Also an improved design of the sample-table for better positioning of the fibre was chosen (see *Figure 4.51b above*). The grating was prestrained and fixed at two points with the two-component epoxy. After gluing of the bare FBG the central wavelength changes by 0.04 nm.

Figure 4.58 shows the transmission spectrum of the bare FBG at indentation in the middle of the grating and reflection spectrum at indentation near the centre of the FBG. An attenuation of 2.34 dB was observed at a transverse load of 9.3 N (see *Figure 4.58a*). Loading of the FBG near the centre with a transverse load of 7.9 N led to a sideband increase and bandwidth broadening. Investigations were repeated for a few standard FBG sensors fabricated for sensor applications. No significant changes in the fibre spectrum occurred.

The danger of crack development is high for investigation of the bare FBG. At point-wise transverse loading of a fibre, there are small local changes in fibre geometry, which usually lead to the change of polarisation of propagated light and result in signal attenuation and birefringence. No critical polarisation changes were observed for an applied load of 9 N.

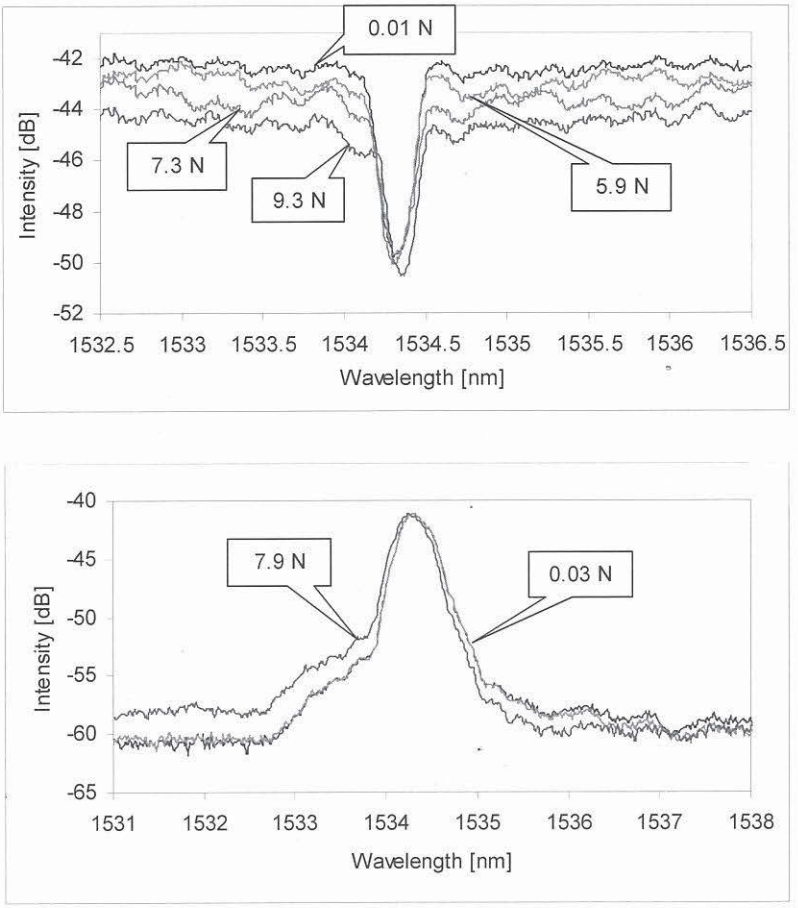

Figure 4.58: Spectra of the bare FBG: a) transmission spectrum at indentation in the middle of the FBG; b) reflection spectrum at indentation in the 1/2 nearby the middle of the FBG.

If FBG sensor is embedded into the structure it can experience larger stress influences than with a transverse load of 9 N. Contrary to the axial elongation of the fibre, small local transverse loads introduce very small perturbations compensated by other influences.

5 Summarised results

Theoretical and experimental investigations were conducted to investigate and study unwanted influences that occur during the application of Bragg gratings. The present study established when and under which conditions signal reading problems start to become critical for the defined applications. Investigations were carried out with uniform short fibre gratings both as free gratings and integrated into a sensor housing or into a material or a structure.

5.1 Overview of obtained theoretical results

In practice, combinations of influences affect the FBG signal. Sometimes, the experimental investigation of only one perturbing influence is complicated. For this reason, it is important to provide first the theoretical study of separate effects. There are many theoretical estimates for specific cases in literature [Hil97], [Erd97], [Bob97a], [Mag97], [Bob98a], [Lebi98], [Oth99], [Kas99], [Gaf00], [Bob00], [Gon01], [Lop02]. This thesis brings together all these theoretical evaluations of the FBG signal, considering only uniform short FBG written in the single mode fibre core.

It is possible to evaluate theoretically the reflection or transmission spectra of uniform and unperturbed FBGs. The FBG length, period, and coupling coefficient between propagating modes define reflectivity, slope, and bandwidth of the resulting grating spectrum. Low sideband of the FBG spectrum can also be achieved by definition of appropriate grating parameters: it can be essentially decreased by the selection of the defined FBG profile.

The temperature sensitivity of a uniform FBG not exposed to any other influences has been investigated by several authors and is given as 14 pm/K. The proposed scheme of the temperature sensor with the FBG presents linear response only for a temperature range of approximately 30 K (see *Figures 3.9 and 3.10*).

Theoretical evaluation of a transverse load influence on the FBG has to consider a polarisation change of the propagated light. A fibre geometry variation under transverse loading can be modelled by the perturbation theory, combined with the coupled modes theory for the calculation of the FBG transmission/reflection spectrum. Material parameters under such as refractive index modulation in the result of the transverse stress have to be considered in accordance with the photoelasticity theory for isotropic medium [Cok57]. The theoretical apparatus allows analysis of fibre deformation, transverse strains distribution in the fibre cross-section and FBG spectrum changes as the result of applied load. Along developed theoretical model, the FBG spectrum shows noticeable changes in the reflected light at an applied transverse load value of 15 N.

The modelling of a grating bending reveals a complexity of distortions introduced to the FBG spectrum by inclinations of the grating planes, stress in the fibre in the result of bending, and deformation of the modal distributions of the propagating and reflected modes. Uniform bending of the grating was chosen for the modelling, where the grating axis corresponds to the bending axis and grating planes deforms symmetrically. Noticeable changes in the grating spectrum are introduced starting at a bending radius of 2.5 mm.

Hence, theoretical results are difficult to compare with experimentally achieves ones, it will be proposed to improve model more near to the praxis.

5.2 Overview of experimental results

In the present work, acrylate-recoated gratings were chosen for investigation of their behaviour in the temperature range from –40 °C until 60 °C, for the static loading until 0.3 %, and for embedment into composite material. Theoretical data summarised in the previous subsection are used for evaluation of data from the experimental part of investigations.

5.2.1 Free FBGs

Investigations with free gratings were provided for study of separate perturbing influences during the FBG operation.

Corresponding to the calculated data, the strain sensitivity of a fibre Bragg grating (1550 nm) written in a commonly used telecom silica glass fibre is 1.2 pm/με. In the theoretical model of strain influence on the FBG it is assumed that light propagates in an ideal cylindrical medium, uniformly along the whole fibre length even if strain influence occurs. This approach can be accepted for bare gratings. Investigated by Rao bare grating had a strain sensitivity of 1.2 pm/με [Rao02]. In other cases, the fibre can be pre-stressed additionally by various recoating materials [Hab00], [Tru01]. Therefore, an acrylate-recoated grating (produced by IPHT Jena) was investigated for axial strain until 0.3 %. The evaluated deviation between measured and calculated FBG strain sensitivity was 2.12 %. Afterwards, the FBG was loaded during 6 months (see *Figure 4.6*). The deviation between FBG strain sensitivity measured on the beginning and after 6 months of loading was 3.2 %. Subsequently, critical failure of the grating occurred shortly after four tensile tests (until 0.3 %). The grating strain sensitivity changes could be caused by minicracks appearing on the recoating material surface. Time to failure usually depends on the stress history of the fibre. It is recommended that long-term investigations are repeated for acrylate-recoated gratings also from other producers to check stability of the grating sensitivity, because the changes in the strain sensitivity of a free grating after a long-term loading are not known in literature.

Bending investigations of gratings (produced by Ingenieurbüro Jens Peupelmann and AOS GmbH) have shown that there are noticeable changes in the grating spectrum, when the bending radius is 2.5 mm or less. Such small radiuses may occur locally at the sensor embedment into composite material (see *Figure 4.39*).

The applied transverse stress influence on the grating results in the birefringence effect. Critical changes in the transmission spectrum occur at the load value of 13 N. Usually, such critical changes appear at larger load values (approximately of 20 N).

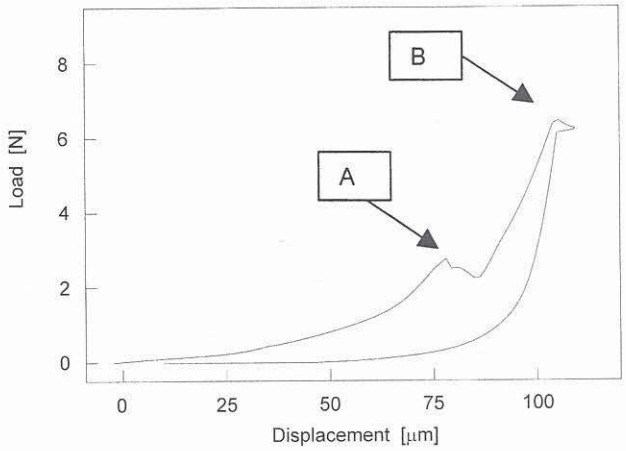

Figure 5.1: Dependence of the applied force of the indenter on the displacement of the indenter. Points on the diagram marked with: A - crack of the fibre coating; B - crack of the fibre.

A point-wise transverse loading of recoated gratings confirmed that the most important reason of the grating failure at point-wise influences is the coating material. An acrylate-recoated grating pressed by an indenter (57 μm) until 7 N was broken. A crack appeared first in the bottom of the coating (see *Figure 5.1* and *Figure 5.2*), and following this damage occurred to the fibre core. This has to be considered at embedment of the grating. Danger of the critical grating failure is higher in the case of sensor embedment into non-homogeneous composite materials.

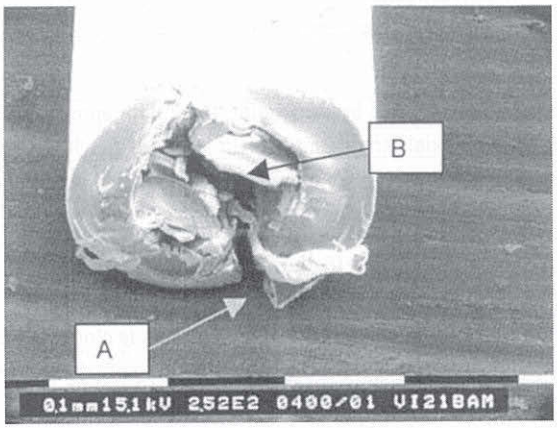

Figure 5.2: Crack development in the acrylate-recoated grating exposed to the point-wise transverse indentation. Points on the SEM photo: A - crack of the fibre coating; B - crack of the fibre.

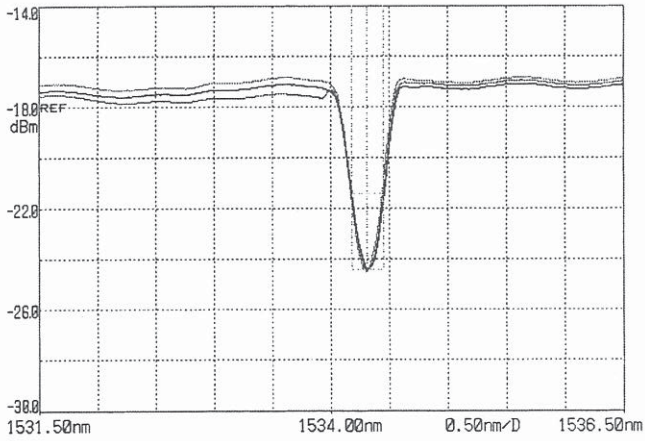

Figure 5.3: Transmission signal changes of the bare grating exposed to the point-wise indentation until 6 N.

Bare gratings exposed to point-wise load showed noticeable changes in the transmitted or reflected spectrum starting of approximately 6 N of applied load (see *Figure 5.3*). The sideband increase by 3.3 dB, the spectrum broadening by 18 pm and even small wavelength shift by 32 pm were noticed at a load of approximately 9 N (see *Figure 4.58*). Small scratches on the surface of the uncoated fibre appeared after the point-wise loading. Nevertheless, there was no fibre damage even if the tests were repeated three times.

5.2.2 FBG sensor rod

When gratings are integrated into a sensor housing, the strain sensitivity of a sensor rod was tested until 0.5 % of strain. Linearity in the measured signal and long-term stability of the signal were two questions of interest for this investigation. When the sensor is embedded into the concrete material on a bridge and cracks develop where the sensor rod is installed, a strain above 0.3 % can affect the steel rod.

The strain applied to sensor caps is read by the grating fixed with epoxy inside the sensor rod. The sensor response to the applied axial strain (until strain value of 0.3 %) was linear. The evaluated strain sensitivity of the sensor rod at the beginning of investigations was (1.14 ± 0.05) pm/με. This value differs from the FBG sensitivity by 5 %.

The sensor rod exposed for three weeks to the axial strain of 0.3 % proved stable. Tests after permanent straining showed a systematic difference from the former result. The measured strain sensitivity of the sensor afterwards was (1.22 ±0.04) pm/με. This is closer to the theoretical value for the bare FBG. Difference between the sensor sensitivities before and after permanent strain is 6.6 %. Afterwards, the FBG response, however, kept its linearity. Further axial straining of the sensor rod showed that non-linearity occurred at the strain value of 0.5 %. All trials have shown excellent

reiteration along two curves shown in *Figure 4.14*, so it can be concluded that some permanent changes were introduced to the sensor housing.

5.2.3 Attached FBGs

Attached grating were investigated only for comparison with the embedded ones. The FBG (1549.2 nm) fixed with X60 glue experienced at a strain of 0.3 % non-uniform stress obviously caused by fibre creeping and non-uniform local stress in the cured X60 epoxy glue. The grating (1549.8 nm) attached with R&G glue showed almost linear response to the applied load. The evaluated FBG strain sensitivity is (1.018 ± 0.003) pm/με . The elongation sensitivity of this grating is comparable with those of embedded gratings, which makes it relevant for some applications, where small strain ranges have to be measured and an embedment of gratings will not be possible.

5.2.4 Embedded FBGs

New composite material was characterised by using structure-integrated fibre Bragg grating sensors. Every investigated grating survived the embedment procedure. The fibre-reinforced composite material with embedded FBG sensors was tested under thermal and mechanical loading. Behaviour of embedded gratings during tests was investigated.

Thermal loading

Embedded gratings were exposed to three temperature cycles. Table 5.1 shows calculated thermal sensitivity coefficients of the embedded gratings for one of the temperature transitions from –40 °C till 60 °C.

Table 5.1: K_T of different FBGs at the temperature range from -40 °C to 60 °C.

No.	FBG wavelength [nm]	K_T [$\times 10^{-6}$ 1/K]
1.	1539.11	13.96 ± 0.13
2.	1530.73	12.79 ± 0.35
3.	1535.76	13.01 ± 0.40
4.	1539.72	13.80 ± 0.37
5.	1543.35	8.82 ± 0.24
6.	1548.32	12.90 ± 0.34
7.	1552.45	12.79 ± 0.33
8.	1556.7	12.88 ± 0.67
9.	1560.98	12.92 ± 0.47

It was noticed that the slope of thermal dependence for each grating differs for temperatures T < 0 °C and T > 0 °C (see *Figures 4.31*). The Bragg grating thermal sensitivity for the temperature range from –40 °C to 60 °C has shown a non-linear character. A non-linearity in the thermal response for temperatures from -40 °C until -20 °C was observed for free acrylate-recoated gratings, which was explained with dependence of the elasticity of the coating material on the temperature [Tru01]. The thermo-optic coefficient of commercially manufactured gratings also depends on the temperature [Rei98], which is why thermal sensitivity of recoated gratings can be more quadratic in character.

Only one of the gratings has shown a birefringence at temperatures below -20 °C (see *Figure 4.32*). The birefringence is weaker at higher negative temperatures (e.g. –20 °C). In this case of birefringence, two reflected peaks occurred in the FBG reflection spectrum and the definition of the grating sensitivity at low temperatures becomes complicated.

Results of thermal loading of embedded gratings allow to conclude that each FBG sensor have to be calibrated before embedment into the host material. This will allow to separate gating thermal responses from additional influences of a material and to analyse obtained results reliably.

Static strain

Every investigated grating reported the linear response to the axial strain. No changes in the strain sensitivity of single FBG sensors could be determined during the test cycles. The measured Young's modulus of the composite material was (31.0878 ± 0.0016) GPa. The mean sensor sensitivity was (1.1736± 0.0003) pm/με. Embedded sensors strain sensitivity differs from the calculated value for the free FBG by 4.6 %.

Only one grating showed significant spectrum broadening, chirp, and considerable attenuation at a strain of 0.2 %. Analysis of this grating spectrum during flexure of the specimen revealed that the side band increased at a deflection value of 40 mm (see *Figure 5.4*), which corresponds to the strain affecting this grating of 329.33 με. Even such small strain values produced significant sideband increase. The clear chirp of the FBG spectrum would occur when the grating is not straight inside the material. The bandwidth broadening or sideband increase are usually caused by transverse stress acting in the grating area or by other geometrical changes of the FBG. This could be caused by the embedding method used or it could also be a matter of the FBG quality.

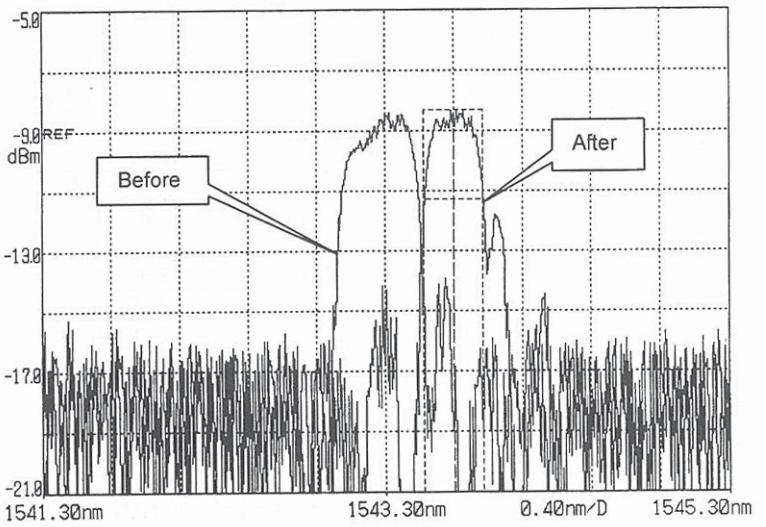

Figure 5.4: Spectrum of embedded FBG before and after flexure of the cantilever composite beam.

This was the only one of 16 gratings embedded into this type of composite material, to show mistakes during static load tests. For further investigations it is recommended to calibrate each grating before embedment to evaluate material influence on the grating after embedment and improve embedment procedure.

Flexure investigations

Flexure investigations with a cantilever beam and a three-point supported beam were provided to investigate the response of embedded and attached gratings to the bending-induced strain. Such tests help to reveal bonding quality of the grating inside the host material or attached grating. Responses of embedded gratings agree well with the calculated values. One of attached gratings experienced poor adhesion of the glue with a surface of material and showed larger strain than was calculated. In the case of cantilever beam, there is a chirp effect that have to be expected at smaller bending radius as investigated. At large bending radiuses, birefringence and chirp of the grating main peak can be neglected.

5.3 Conclusions

On the basis of the investigations carried out with free gratings and gratings integrated into the sensor housing, attached on or embedded into material to be investigated, strain sensitivity coefficients K_ε from the measured data were calculated (see Table 5.2). Each case was measured at stable room temperature conditions (24 °C). Therefore, it can be concluded that deviation in strain sensitivity coefficients for differently applied gratings appears from the application procedure: fixing or embedment.

Table 5.2: Strain sensitivity coefficients K_ε

Sensor	Bragg wavelength [nm]	K_ε [$\mu\varepsilon^{-1}$]
Free FBG	1569.82	0.7671 ± 0.0002
Strain sensor rod	1552.55	0.7650 ± 0.0041
Embedded FBG into textile-reinforced composite material	1532.70	0.7393 ± 0.0002
Attached FBG with X60	1549.06	0.2651 ± 0.0002
Attached FBG with R&G epoxy	1529.92	0.6656 ± 0.0002

A strain of 0.3 % is no problem for the free gratings or for the integrated gratings. Within these margins, reliable measurement with this type of fibre-optic sensors is possible. It will also be acceptable to use gratings attached with two-component epoxy glue in cases where embedment of FBGs is not possible. The acrylate-recoated gratings are acceptable for application even for embedment within investigated conditions, but non-linearity has to be expected for lower or higher temperatures as well as for higher static loads.

6 Conclusions and Recommendations

The main question of this work was: is it possible to separate unwanted and unavoidable influences on applied FBG sensors from the sensor signal and if not, is it still possible to interpret measured data in the right way? Free acrylate-recoated gratings show non-linear response in the temperature range from –62 °C to –20 °C (see *Figure 1.1a*). Embedment into mortar or concrete material revealed crack development or even damage of the coating (see *Figure 1.2*). Other coating materials were also damaged after concrete-embedment procedure (see *Figures 1.3 and 1.4*). In the present work only short acrylate-recoated fibre Bragg gratings were used. This type of coating was chosen because of the water-proof characteristics and small measurement ranges of the strain and temperature required. For these purposes, different FBG sensors were tested under different extrinsic influences and embedment into highly non-uniform composite.

The strain (0.3 %) applied to the acrylate-recoated grating revealed a linear grating response. However, after 6 months of tests, a small decrease in the grating strain sensitivity of 3.2 % was observed in contrast to other studies of long-term sensitivity met in the literature, which do not report changes. Therefore, the long-term response of gratings has to be investigated from various manufacturers and for larger strain values.

The grating bending revealed noticeable changes for the radius of 6 mm. A grating exposed to bending with a radius of 2.5 mm has shown significant spectral changes. In the case of unapplied gratings, or where bending-free fixing of the grating inside a sensor housing can be ensured, this influence can be avoided. If the grating is embedded into a non-uniform structure, the microbending-induced distortions to the recorded signal have to be avoided by an improved embedment technique. Where this influence cannot be avoided, sensors will not deliver reliable information.

A point-wise transverse load of 9 N (indentor width: 57 µm) affecting an unapplied recoated grating causes its critical failure. For an indentation with a load of 7 N, signal attenuation of 33.82 dB and wavelength shift by 0.2 nm were recorded. The point-wise indentation on the bare grating with 9 N revealed a sideband increase by 3.3 dB, a spectrum broadening by 18 pm and a small wavelength shift by 32 pm. There were some scratches on the surface of the grating after the indentation. This procedure was repeated three times, but no significant changes were observed in the spectrum of investigated gratings.

Local perturbing influences such as point-wise transverse load and microbending can lead to critical failure of the FBG sensor, but they can successfully be avoided by improvement of the embedment technique as was shown in the case of composite-integrated sensors. No significant changes in the grating signal can be observed when there are no microbending effects with the bend radius < 2.5 mm and point-wise local influences larger than 6 N (2 GPa). In general, transverse loads lead

to attenuation of the grating signal and if held in the range of < 20 N, no critical changes into the sensor signal will be introduced.

If the grating is applied into a sensor housing (e.g. the FBG sensor rod), the fixing technique of the grating inside the sensor rod as well as sensor rod stiffness are of key importance for the further reliable and stable operation of the sensor. In a situation where a strain influence larger than 0.3 % has to be expected, the investigated type of sensor cannot be applied.

In the case of embedded gratings, their reliable operation depends on the grating coating material and host material properties and embedment technique quality. Acrylate-recoated gratings can be successfully integrated even into the non-uniform composite material described in detail in subsection 4.1.3, where local influences as well as general transverse stress on the fibre inside the host material are expected. Linearity was reported at static loading until 0.6 % and thermal cycling from –40 °C to 60 °C. However, grating failure caused by the different dependencies of the host material elasticity and the coating material elasticity on temperature has to be expected. Temperature investigations revealed an apparently very small hysteresis, which is less than the uncertainty of the temperature controlling of the climate chamber (Figure 4.34). This small decrease in the characteristics should be traced back to the drift of the climate chamber. Only one grating showed birefringence for the temperature range from -40 °C to -20 °C. In this case, the host material and the coating material contraction considerably increase the thermally-induced non-linearity of the grating response at -40 °C. This occurs in the result of expected bonding defects (see Figure 4.17b). At the same time, this grating showed linear response to an axial strain up to 0.3 %. The average strain sensitivity coefficient K_ε of investigated gratings was defined as $(0.7393 \pm 0.0002)\ \mu\varepsilon^{-1}$. One of embedded gratings showed considerable attenuation and sideband increase even at an applied strain of only 0.2 % (see Figure 5.4). A non-appropriate position of the grating inside the host material occurred as a result of non-uniform epoxy ingress during curing of the composite (see Figure 4.16b).

The grating attached to the surface of the specimen with X60 epoxy glue showed the step-wise systematic error in the response due to the large difference in the material elasticity between the material surface, the acrylate-recoated grating and the X60 glue. Gratings attached with the two-component epoxy glue (R&G) showed a strain response, which tends to be linear up to 0.3 %. Only one grating fixed with this glue on the surface of the composite material showed poor bonding.

In the case of integrated gratings, operation limits could be recognised by carrying out flexure investigations. Requirements with regard to the embedment technique could be recognised as well.

A sensor system in which FBG sensors have to be installed, has to be analysed previously and evaluated under critical influences, which can affect the FBG measured signal. On the other hand, exact grating parameters, such as refractive index and refractive index modulation, thermo-optic coefficient, coefficient of expansion and photo-elastic coefficients, as well as grating geometry (architecture) and coating material properties have to be known. This makes it possible to avoid the unreliable operation of the sensor.

7 Outlook for further investigations

The investigations undertaken once more proved that for a reliable theoretical evaluation or for the analysis of obtained results it is important first to know material characteristics and grating parameters. It is also important to know the grating architecture and parameters, because this allows the timely rejection of gratings which might produce a failure in further applications. This failure diagnostics is valuable especially in the case of embedded gratings or sensor networks where the replacement of failed grating would be impossible or very costly.

It is also important to investigate the influence of thermal and stress gradients on the behaviour of the FBG. This situation is frequently encountered in the case of embedded gratings, where the position of the grating inside investigated material is difficult to define. Resulting changes introduced by such influences may cause a FBG spectrum chirp, which will then introduce large deviations in the obtained signal.

7.1 Estimation methods of gratings parameters

For successful integration of sensors, it is important to define parameters of each grating which have to be applied. This allows the theoretical evaluation of grating behaviour under different influences. At present, manufacturers supply only such grating data as central wavelength, reflectivity of the grating, average refractive index change along the grating length, and NA of the fibre. The grating selection procedure has to be developed and applied before installation of this element in the sensor architecture (whether local sensor or sensors network).

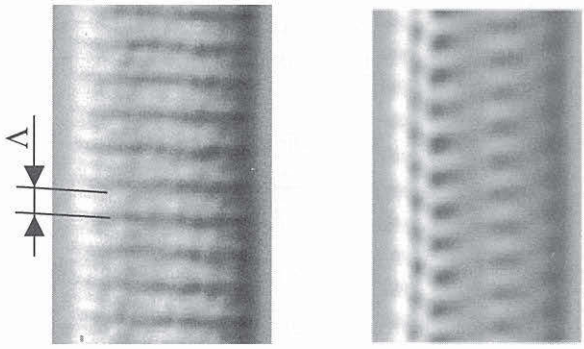

Fig. 7.1: Images of the FBG made using the DIC technique (After: [Dra02]).

One of the possible solutions can be non-destructive imaging of refractive index modulation along a grating. The proposed differential interference contrast (DIC) imaging technique looks very promising [Dra02]. Refractive index changes recorded with this technique are highly non-uniform. The period of the investigated grating was determined from the image with an uncertainty of ± 0.017 μm (see *Figure 7.1*). A next image taken after the grating and rotated by 90° shows that the refractive index modulation within the fibre core is not uniform as it was supposed, but quite complex. Therefore, it is recommended to provide preliminary tests before planning an application of the grating.

Another problem remaining in this field is the coating of the grating. Gratings used in these investigations were bare or recoated with an acrylate coating material, which is not desirable in some applications because of influences of an additional coating at high strains or extreme temperatures [Hab00], [Tru01]. Investigations have shown that acrylate coatings are acceptable for application within defined strain and temperature margins, because only 2 of 16 tested gratings shown a non-linear response, which can be also a result of an embedment failure. Application of gratings for embedment into some materials such as metal or cementitious composites requires well-defined selection of the coating. Especially for alumnia-composites, where a transverse load affects a grating after embedment or thermal stress, coating selection is of a vital importance for the resulting grating operation [San02]. Acrylate coating is not recommended in such cases. FBG with polyimide or ORMOCER® coating ensures the grating's linear response to even larger load values than 0.3 % and at extreme temperatures [Hab00], [Tru01]. On the other hand, they cannot be applied in cases where a contact with water or water solutions is anticipated [Hab00]. Other coating materials proposed on the market have not yet been sufficiently investigated.

7.2 Periodical structures on the fibre cladding for specific sensor applications

Here, investigations were conducted on FBG sensors used for measuring strain and temperature. Other measurands can be also recorded with this type of fibre optic sensor. Other types of fibre optic grating can be used for monitoring moisture, pH-value or water content or for other chemical applications where registration of a refractive index of the medium is very important. For such purposes, periodical structures created on the surface of the optical fibre can operate as probes and interfere with the measurand directly [Lebi99]. Periodical structure on the fibre cladding can be of following types:

a) refractive index of fibre cladding changes along the fibre axis as a periodical function $\Delta n = n_0\left(1 + m \cdot \cos\frac{2\pi}{\Lambda} z\right)$;

b) fibre cladding consists of two different materials with different refractive indices and the diameter of boundary between two materials is also described by a periodical function;

c) boundary between fibre cladding and the core is corrugated and the core diameter changes along the fibre axis as a periodical function $D = D_0\left(1 + m \cdot \cos\frac{2\pi}{\Lambda} z\right)$;

d) fibre cladding is corrugated and the external diameter changes as a periodical function $D = D_0\left(1 + m \cdot \cos\frac{2\pi}{\Lambda} z\right)$.

The cases *a)* and *b)* can be theoretically considered, as can cases *c)* and *d)*. The calculation mechanism of light propagation in fibre cladding structures is presented in detail in Attachment E.

In summary, the results show that fibre cladding gratings in which the refractive index changes along the fibre axis as a periodical function are not sufficiently sensitive to refractive index changes of measurand in contrast to corrugated cladding periodical structures.

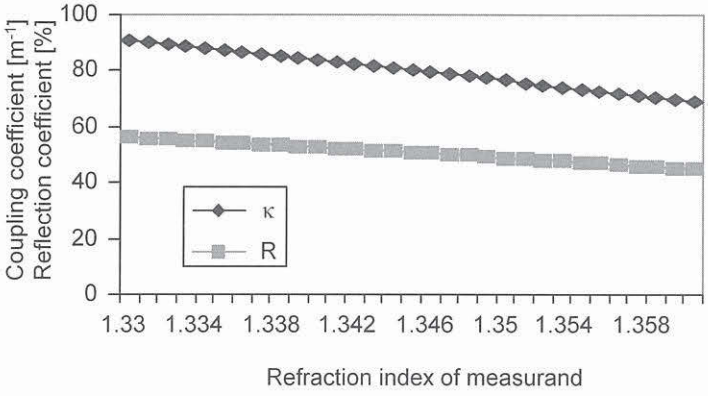

Figure 7.2: Dependence of the reflection coefficient R and the coupling coefficient κ on modulation of the measurand refractive index n_m.

In the case of corrugated structures, reflection and coupling coefficients between coupled modes at grating length of 7 mm depend on the refractive index modulation of the measurand as shown in *Figure 7.2*. Corrugated cladding gratings are sensitive enough to refractive index changes of measurand and can be used for various sensing purposes, especially for chemical sensor applications. Such structures also have a sufficiently high reflection coefficient and can be used for other applications too.

Attachment A Light propagation in an optical fibre with step-index profile

There are several methods for determining the fields in single mode fibres and the simplest of them is based on the perturbation theory [Sny81b].

It will be assumed that the fundamental mode LP of the optical fibre is a quasi-transverse electro-magnetic wave and in a simple case, this wave is polarised only in one direction. If polarisation direction is along the axis x, then the field in the fibre can be given by a system of scalar equations

$$\begin{aligned} E_x &= \psi(r)e^{-j\beta z} \\ H_y &= \sqrt{\frac{\varepsilon}{\mu}}E_x \end{aligned}, \tag{A.1}$$

where field components E_x, E_z, H_x, and H_z are not taken into consideration, μ and ε are a permeability tensor and a dielectric tensor or permittivity, and ψ is a scalar wave function. The refractive index of the fibre core is approximately equal to the fibre cladding refractive index $n_{co} \cong n_{cl}$ and the correlation for the propagation constant is given by

$$\beta \cong \frac{2\pi n_{eff}}{\lambda_{prop.}}, \tag{A.2}$$

where n_{eff} is an effective refraction index of the fibre core for weakly guided fibres. This is approximately like a case of the *plane* wave propagation constant in endless medium with the refractive index within the range of $n_{cl} \le n_{eff} \le n_{co}$. Polarisation properties of fibre structure have weak influence on field inside the fibre because the refractive indices are approximately equal $n_{co} \cong n_{cl}$. If the dielectric medium has close parameters, then reflection of the wave from the interface is not sensitive to the polarisation of an incident wave. Spatial modulation of the field $\psi(r)$ is not sensitive to polarisation effects either. The function $\psi(r)$ is the solution of a scalar wave equation

$$\left\{\frac{\partial^2}{\partial r^2} + \frac{1}{r}\frac{\partial}{\partial r} + k^2(r)\right\}\psi(r) = \beta^2\psi(r), \tag{A.3}$$

where $k(r)$ is defined by equation:

$$k(r) = \frac{2\pi n_{eff}(r)}{\lambda}. \tag{A.4}$$

This function corresponds to the largest value of the propagation constant β, and does not depend

on the polar angle ϕ. The scalar wave function $\psi(r)$ has maximum value when $r = 0$ and tends to zero as the radius r increases. Solutions of equation (A.3) for step-index and graded-index profiles of fibres have shown that $\psi(r)$ are of approximately Gaussian shape [Hon74], [Sny81b]. It is important to find satisfying approximation for the field $\psi(r)$ and the propagation constant β of the fundamental mode along the optical fibre with a step-index profile assuming that the field of modes is given by

$$\psi(r) \cong C \exp\left(-\frac{1}{2}\left(\frac{r}{r_0}\right)^2\right), \tag{A.5}$$

where r is a radius of cylindrical propagation medium, r_0 is a "spot size" defined by the variation method, C is a constant derived from the normalisation condition:

$$2\pi \int_0^\infty r\psi^2(r)dr = 1. \tag{A.6}$$

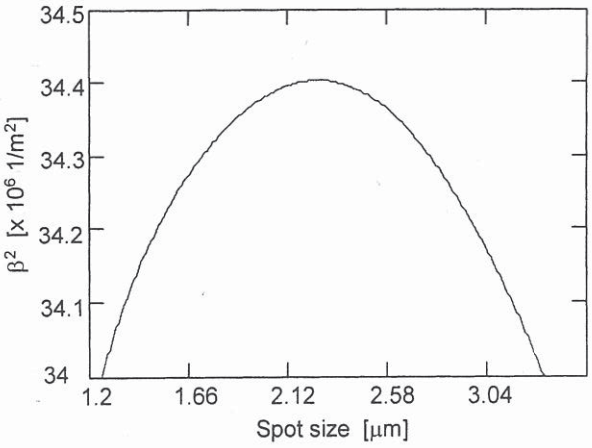

Figure A.1: Dependence of the square of the propagation constant on the spot size $\beta^2(r_0)$.

If equation (A.5) is a solution of equation (A.3), then it can be used as a trial function for the steady-state equation of the propagation constant β. The spot size r_0 from the condition of the maximal value of propagation constant is found [Sny79]. The propagating mode corresponds to the maximum value of the propagation constant β. A square of the propagation constant β is given by

$$\beta^2 = \frac{\int_0^\infty \left\{-\left(\frac{d\psi}{dr}\right)^2 + k^2(r)\psi^2\right\} r dr}{\int_0^\infty r\psi^2 dr}. \tag{A.7}$$

According to equation (A.7), the dependence $\beta^2 = f(r_0)$ is shown in Figure A.1. Obviously, the spot size r_0 changes in the range between $\rho - \delta\rho \le r_0 \le \rho + \delta\rho$. Moreover, the maximum value of $\delta\rho$ is

in the range which allows definition of the maximum value on the curve. In some cases it is possible to find β^2 and r_0 analytically by substitution of (A.5) into (A.7) and equal first r_0 derivative of (A.7) to the zero:

$$\frac{\partial \beta^2}{\partial r_0} = 0 . \tag{A.8}$$

Substitution of (A.5) into (A.7) will give

$$\beta^2 = \frac{-0.5 + \left(\frac{2\pi n_{co}}{\lambda}\right)^2 \int_0^{\rho} \exp\left[-\left(\frac{r}{r_0}\right)^2\right] r dr + \left(\frac{2\pi n_{cl}}{\lambda}\right)^2 \int_{\rho}^{\infty} \exp\left[-\left(\frac{r}{r_0}\right)^2\right] r dr}{\int_0^{\infty} \exp\left[-\left(\frac{r}{r_0}\right)^2\right] r dr}, \tag{A.9}$$

where ρ is a radius of the optical fibre. The spot size r_0 for the step-index profile of the optical fibre is given by

$$r_0^2 = \frac{\rho^2}{\ln V^2}, \tag{A.10}$$

where V is a fibre parameter and $V = \frac{2\pi\rho\Delta}{\lambda}$ [Sny81a], where $\Delta = \sqrt{{n_{co}}^2 - {n_{cl}}^2}$. The normalised frequency V is less than 2.4 for the single mode fibre. By substitution of r_0 into (A.9), equation for the propagation constant β will be found:

$$(\rho\beta)^2 = (\rho k_{co})^2 - \ln V^2 - 1 . \tag{A.11}$$

The radius ρ of the fibre core in which maximum light concentration occurs can be defined from the condition $V = \exp(0.5) \cong 1.65$, which corresponds to $r_0 = \rho = \frac{1.65\lambda}{2\pi\Delta}$.

Dependence of a square of the propagation constant on radius of the optical fibre $\beta^2(r_0)$ is shown in Figure A.1. The maximal value of $\beta^2(r_0) = 8.69649\times10^{-6}\ \mathrm{m}^{-1}$ corresponds to the spot size $r_0 = 3.16\ \mu\mathrm{m}$ for the 8 μm radius of the fibre core. If characteristics $\psi(r)$, r_0, β, m, $n(r)$ are known, it is possible to describe the field in the fibre.

Attachment B Coupled mode theory for the unperturbed and uniform FBG

A simple case of single mode fibre will be considered. Since the medium is uniform in direction z, the normal modes propagating in this direction will be

$$E_m(x,y)e^{j(\omega t-\beta_m z)},$$

where m is a mode subscript which is, for example, discrete for confined modes in a case of waveguide modes.

Electric vector $\vec{E}$ and magnetic vector $\vec{H}$ of an optical fibre with a circular symmetry of the cross-section are given by

$$\begin{aligned} E(r,\phi,z) &= e(r,\phi)\exp(-j\beta\cdot z), \\ H(r,\phi,z) &= h(r,\phi)\exp(-j\beta\cdot z) \end{aligned} \tag{B.1}$$

where $\exp(\omega t)$ is a non-obviously mentioned time dependence, β is a mode propagation constant, r and ϕ are polar coordinates, z is the longitudinal axis. If the difference between refractive indices of fibre core and cladding is less than 1 %, then vectors $\vec{E}$ and $\vec{H}$ could be approximated by scalar wave equation solutions (Attachment A). Two modes are propagating along the fibre with periodical structure:

$$\begin{aligned} &\text{incident wave } A_1(z)\psi(r)e^{-j\beta\cdot z}, \\ &\text{reflected wave } A_2(z)\psi(r)e^{j\beta\cdot z}. \end{aligned} \tag{B.2}$$

Substitution of (B.2) into (3.4) taking into account (3.5) and (3.8), gives:

$$\begin{aligned} &\left[-2j\beta A_1'(z)e^{-j\beta\cdot z}+2j\beta\cdot A_2'(z)e^{j\beta\cdot z}\right]\psi(r) \\ &+\left(k_0^2(r)m(r)e^{j\frac{2\pi}{\Lambda}z}+k_0^2(r)m(r)e^{-j\frac{2\pi}{\Lambda}z}\right) \\ &\times\left(A_1'(z)e^{-j\beta\cdot z}+A_2'(z)e^{j\beta\cdot z}\right)\psi(r)=0. \end{aligned} \tag{B.3}$$

In equation (B.3), part $\psi(r)e^{\pm j\beta\cdot z}$ is considered as the solution of equation (A.3). Parts with square of the modulation coefficient $m^2(r)$ and derivatives of second order on z $A_1''(z)$ and $A_2''(z)$ are neglected. In other terms, the system of equations for propagating and reflected modes are

$$\frac{d}{dz}A_1 = -j\kappa A_2 e^{j\Delta\beta\cdot z},$$
$$\frac{d}{dz}A_2 = j\kappa^* A_1 e^{-j\Delta\beta\cdot z}, \tag{B.4}$$

where $\Delta\beta = 2\beta - \frac{2\pi}{\Lambda}$, and $\kappa = \frac{\pi}{\beta}\int_0^\infty r\psi^2(r)k_0{}^2(r)m(r)dr$. Quick-varying parts along the axis z introduce approximately zero contribution to the change of amplitudes $A_1(z)$ and $A_2(z)$ at integration of system (B.4) and can therefore be neglected. The following assumptions are accepted: at $z=0$ the incident wave amplitude is given by $A_1(0)=A_1$ and at $z=-L$ the reflected wave amplitude is given by $A_2(-L)=A_2$, where L is the FBG length. It is accepted also that $A_2(L)=0$ and $A_1(0)=1$. The general solution for amplitudes of two modes is given by

$$A_1(z) = e^{j\frac{\Delta\beta}{2}z}\left\{\frac{s\cdot\cosh[s\cdot(L-z)]+j\frac{\Delta\beta}{2}\sinh(L-z)}{s\cdot\cosh(s\cdot L)+j\frac{\Delta\beta}{2}\sinh(s\cdot L)}A_1(0)\right.$$
$$\left.+\frac{-j\kappa e^{j\frac{\Delta\beta}{2}L}\sinh(s\cdot z)}{s\cdot\cosh(s\cdot L)+j\frac{\Delta\beta}{2}\sinh(s\cdot L)}A_2(L)\right\},$$
$$A_2(z) = e^{j\frac{\Delta\beta}{2}z}\left\{\frac{-j\kappa^*\sinh[s\cdot(L-z)]}{s\cdot\cosh(s\cdot L)+j\frac{\Delta\beta}{2}\sinh(s\cdot L)}A_1(0)\right. \tag{B.5}$$
$$\left.+e^{j\frac{\Delta\beta}{2}L}\frac{s\cdot\cosh(s\cdot z)+j\frac{\Delta\beta}{2}\sinh(s\cdot z)}{s\cdot\cosh(s\cdot L)+j\frac{\Delta\beta}{2}\sinh(s\cdot L)}A_2(L)\right\}.$$

Attachment C Approximation of the rectangular cross-section for the elliptical cross-section of optical fibres

In this model, birefringence of modes in the optical fibre is expressed as a sum of two components

$$B = B_G + B_S\,, \tag{C.1}$$

where B_G is a geometrical part concerned to an elliptical shape of the fibre core, and B_S is a stress part concerned to the residual stress in the optical fibre [Nod86].

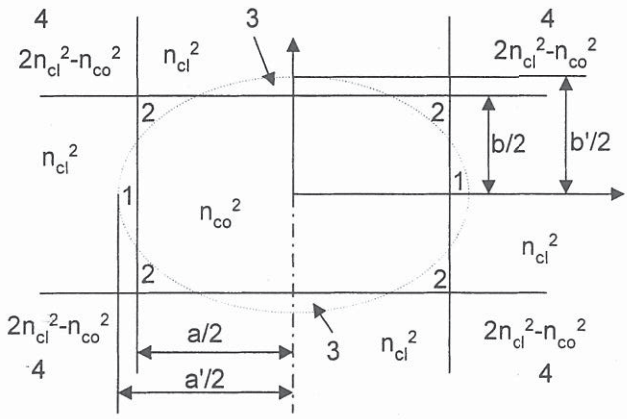

Figure C.1: Schematic representation of geometry modulation of the circular optical fibre in rectangular approximation [Mart99].

Propagation constants of the rectangular-core fibre

The scalar wave equation in the rectangular-core fibre is given by

$$\frac{\partial^2\psi(x,y)}{\partial x^2}+\frac{\partial^2\psi(x,y)}{\partial y^2}+\left[k_0{}^2n^2(x,y)-\beta^2\right]\psi(x,y)=0\,, \tag{C.2}$$

where k_0 is a wave number, $\psi(x,y)$ equals E_x for the quasi TE polarisation and E_y for the quasi-TM polarisation and for the x- and y- polarisation there are $\psi_x(x)$ and $\psi_y(y)$ respectively. In this model, the scalar wave equation solution for the planar structure is used to find $\psi_x(x)$ and $\psi_y(y)$ components and to define propagation constants for the x- and y- polarisation of the propagating mode [Mart99]. The results for a planar waveguide with rectangular cross-section are given by

$$\psi_x(x)=\begin{cases} A_1\cos(\mu_1 x+\alpha), & |x|<\dfrac{a}{2} \\ A_2\exp(-\mu_2|x|), & |x|>\dfrac{a}{2} \end{cases},$$

$$\psi_y(y)=\begin{cases} B_1\cos(\nu_1 y+\gamma), & |y|<\dfrac{b}{2} \\ B_2\exp(-\nu_2|y|), & |y|>\dfrac{b}{2} \end{cases}, \qquad (C.3)$$

where $\mu_1=\sqrt{\dfrac{k_0{}^2 n_{co}{}^2}{2}-\beta_1{}^2}$, $\mu_2=\dfrac{2}{a}\sqrt{\upsilon_1{}^2-\mu_1{}^2\dfrac{a^2}{4}}$, $\upsilon_1=k_0\dfrac{a}{2}\sqrt{n_{co}{}^2-n_{cl}{}^2}$, $\nu_1=\sqrt{\dfrac{k_0{}^2 n_{co}{}^2}{2}-\beta_2{}^2}$, $\nu_2=\dfrac{2}{b}\sqrt{\upsilon_2{}^2-\nu_1{}^2\dfrac{b^2}{4}}$, and $\upsilon_2=k_0\dfrac{b}{2}\sqrt{n_{co}{}^2-n_{cl}{}^2}$, α and γ are zero for symmetric modes and $-\dfrac{\pi}{2}$ for asymmetric modes respectively. Coefficients A_1, A_2, B_1, and B_2 are found for the beginning conditions that E_x and $\dfrac{\partial}{\partial y}E_x$ are continuous in points $y=\pm\dfrac{b}{2}$ and n^2E_x, $\dfrac{\partial}{\partial x}E_x$ are continuous in points $x=\pm\dfrac{a}{2}$. The same conditions were taken for the y-component of the field. Found solutions for the *x*- and *y*- components of the propagation constant can be used to find the parameter P^2 called normalised propagation constant, which is used for further calculations. For an elliptical fibre core this parameter is given by

$$P_i{}^2=\frac{\beta_i{}^2-k_0{}^2 n_{cl}{}^2}{k_0{}^2\left(n_{co}{}^2-n_{cl}{}^2\right)}, \qquad (C.4)$$

where $i=x,y$. Two corrections are considered to define normalised propagation constants of modes in an elliptical core fibre along x- and y-axes $P_x{}^2$ and $P_y{}^2$, using found values for rectangular core fibre. Geometrical corrections $P_x{}^{G2}$ and $P_y{}^{G2}$, which account for the difference in shape between rectangle and ellipse, have to be estimated first, and then stress corrections $P_x{}^{S2}$ and $P_y{}^{S2}$. The normalised propagation constant then is given by

$$P_i{}^2=P_i{}^{0^2}+P_i{}^{G2}+P_i{}^{S2}. \qquad (C.5)$$

Geometrical correction

The square of the refractive index of the rectangular-core fibre is given by

$$n^2(x,y)=n'^2(x)+n''^2(y), \qquad (C.6)$$

where

$$n(x)=\begin{cases}\dfrac{n_{co}^{\,2}}{2}, & |x|<\dfrac{a}{2}\\ n_{cl}^{\,2}-\dfrac{n_{co}^{\,2}}{2}, & |x|>\dfrac{a}{2}\end{cases} \text{ and } n(y)=\begin{cases}\dfrac{n_{co}^{\,2}}{2}, & |y|<\dfrac{b}{2}\\ n_{cl}^{\,2}-\dfrac{n_{co}^{\,2}}{2}, & |y|>\dfrac{b}{2}\end{cases} \tag{C.7}$$

and of the elliptical-core fibre is given by

$$n(x,y)=\begin{cases}n_{co}, & \dfrac{x^2}{a'^2}+\dfrac{y^2}{b'^2}<\dfrac{1}{4}\\ n_{cl}, & \dfrac{x^2}{a'^2}+\dfrac{y^2}{b'^2}>\dfrac{1}{4}\end{cases}. \tag{C.8}$$

The correction to the refractive index square δn^2 in areas signed by 1, 2, 3, and 4 (see Figure C.1) appears as

$$\delta n^2=\begin{cases}\left(n_{co}^{\,2}-n_{cl}^{\,2}\right), & 1,3,4\\ \left(n_{cl}^{\,2}-n_{co}^{\,2}\right), & 2\end{cases}. \tag{C.9}$$

From the calculation of perturbations it follows that geometrical corrections will appear as

$$P_x^{\,G2}=\frac{1}{n_{co}^{\,2}-n_{cl}^{\,2}}\frac{\iint\left|\psi_x(x,y)\right|^2\delta n^2\,dxdy}{\iint\left|\psi_x(x,y)\right|^2\,dxdy},$$
$$P_y^{\,G2}=\frac{1}{n_{co}^{\,2}-n_{cl}^{\,2}}\frac{\iint\left|\psi_y(x,y)\right|^2\delta n^2\,dxdy}{\iint\left|\psi_y(x,y)\right|^2\,dxdy}, \tag{C.10}$$

where $\psi_x(x,y)$ and $\psi_y(x,y)$ are analytic solutions of the scalar wave equation for the fibre with rectangular cross-section.

Stress correction

This second correction is connected with changes of the refractive index induced by the residual stress in the optical fibre. For three-dimensional stress distribution, the dependence between the refractive index and the main stress components is described by the Neumann-Maxwell expression

$$\begin{aligned}n_1&=n_0+p_{11}\sigma_x+p_{12}\left(\sigma_y+\sigma_z\right)\\ n_2&=n_0+p_{11}\sigma_y+p_{12}\left(\sigma_x+\sigma_z\right),\\ n_3&=n_0+p_{11}\sigma_z+p_{12}\left(\sigma_x+\sigma_y\right)\end{aligned} \tag{C.11}$$

where n_0 is a refractive index without stress, n_1, n_2, n_3 are components of the three-dimensional refractive index distribution. p_{11}, p_{12} are elasto-optic constants, σ_x, σ_y, and σ_z are main stress components in the material, where σ_x and σ_y are in the plane xy and σ_z is directed along the axis z. To make the expression simpler, the strain component σ_z can be neglected because it does

not induce birefringence. In addition, it could be assumed that the directions of main stresses coincide with normal stresses and formulations for refractive indices of the fibre will be

$$\begin{aligned} n_x &= n_0 + \Delta n_x \\ n_y &= n_0 + \Delta n_y \end{aligned}, \tag{C.12}$$

where

$$\begin{aligned} \Delta n_x &= p_{11}\sigma_x + p_{12}\sigma_y \\ \Delta n_y &= p_{11}\sigma_y + p_{12}\sigma_x \end{aligned}, \tag{C.13}$$

where Δn_x, Δn_y are changes of the refractive index induced by transverse stresses.

Corrections of the residual stress influence to the propagation constant will appear as

$$\begin{aligned} P_x^{S2} &= \frac{1}{{n_{co}}^2 - {n_{cl}}^2} \frac{\iint \left|\psi_y(x,y)\right|^2 \left\{2n_0\Delta n_x + {\Delta n_x}^2\right\} dxdy}{\iint \left|\psi_x(x,y)\right|^2 dxdy}, \\ P_y^{S2} &= \frac{1}{{n_{co}}^2 - {n_{cl}}^2} \frac{\iint \left|\psi_y(x,y)\right|^2 \left\{2n_0\Delta n_y + {\Delta n_y}^2\right\} dxdy}{\iint \left|\psi_y(x,y)\right|^2 dxdy}. \end{aligned} \tag{C.14}$$

To define Δn_x and Δn_y it is important to know distribution of transverse stresses σ_x and σ_y, which can be found using existing finite-elements method for stress-calculation at any point of the investigated structure.

Parameters of birefringent fibres

Knowing normalised propagation constants of modes it is possible to calculate the general birefringence of the fibre:

$$B = \sqrt{P_x^2\left({n_{co}}^2 - {n_{cl}}^2\right) + {n_{cl}}^2} - \sqrt{P_y^2\left({n_{co}}^2 - {n_{cl}}^2\right) + {n_{cl}}^2}. \tag{C.15}$$

The geometrical birefringence:

$$B_G = \sqrt{\left({P_x}^{0^2} + {P_x}^{G^2}\right)\left({n_{co}}^2 - {n_{cl}}^2\right) + {n_{cl}}^2} - \sqrt{\left({P_y}^{0^2} + {P_y}^{G^2}\right)\left({n_{co}}^2 - {n_{cl}}^2\right) + {n_{cl}}^2}. \tag{C.16}$$

When general and geometrical components of the birefringence are known, it is sufficient for calculation of the stress part of the birefringence:

$$B_S = B - B_G. \tag{C.17}$$

Attachment D FBGs used for research

Table D.1. FBGs used for research.

No.	Company	Sensor configuration	Peak-Wavelength, nm	Reflectivity, %	Transmission loss, dB
1.	AOS GmbH	simple	1543.743	88.70	9.500
2.	AOS GmbH	simple	1547.886	89.50	9.800
3.	AOS GmbH	simple	1551.986	88.70	9.500
4.	AOS GmbH	simple	1539.786	91.40	10.719
5.	AOS GmbH	simple	1555.929	90.23	10.100
6.	AOS GmbH	simple	1535.957	89.70	9.900
7.	AOS GmbH	simple	1559.829	88.70	9.900
8.	AOS GmbH	simple	1531.986	90.00	10.000
9.	AOS GmbH	simple	1563.971	91.50	10.896
10.	AOS GmbH	simple	1527.914	88.70	9.741
11.	Ingenieurbüro Jens Peupelmann	simple	1521.903	N/A	N/A
12.	Ingenieurbüro Jens Peupelmann	simple	1528.623	N/A	N/A
13.	Ingenieurbüro Jens Peupelmann	simple*	1530.865	N/A	N/A
14.	Ingenieurbüro Jens Peupelmann	simple	1532.787	N/A	N/A
15.	Ingenieurbüro Jens Peupelmann	simple	1534.280		
16.	Ingenieurbüro Jens Peupelmann	simple*	1534.316	N/A	N/A
17.	Ingenieurbüro Jens Peupelmann	simple	1536.895	N/A	N/A
18.	Ingenieurbüro Jens Peupelmann	simple	1541.278	N/A	N/A

* Originally supplied without coating

No.	Company	Sensor configuration	Peak-Wavelength, nm	Reflectivity, %	Transmission loss, dB
19.	Ingenieurbüro Jens Peupelmann	simple	1544.726	N/A	N/A
20.	Ingenieurbüro Jens Peupelmann	simple	1548.841	N/A	N/A
21.	Ingenieurbüro Jens Peupelmann	simple	1552.698	N/A	N/A
22.	Ingenieurbüro Jens Peupelmann	simple	1556.769	N/A	N/A
23.	Ingenieurbüro Jens Peupelmann	simple	1560.110	N/A	N/A
24.	IPHT Jena	simple	1569.900	N/A	N/A
25.	Ingenieurbüro Jens Peupelmann	simple/ embedded	1548.882	N/A	N/A
26.	Ingenieurbüro Jens Peupelmann	simple/ embedded	1533.798	N/A	N/A
27.	Ingenieurbüro Jens Peupelmann	simple/ embedded	1534.216	N/A	N/A
28.	Ingenieurbüro Jens Peupelmann	simple/ embedded	1530.865	N/A	N/A
29.	Ingenieurbüro Jens Peupelmann	simple/ embedded	1534.970	N/A	N/A
30.	Ingenieurbüro Jens Peupelmann	simple/ embedded	1532.770	N/A	N/A
31.	Ingenieurbüro Jens Peupelmann	simple/ embedded	1539.680	N/A	N/A
32.	Ingenieurbüro Jens Peupelmann	simple/ embedded	1534.600	N/A	N/A
33.	Ingenieurbüro Jens Peupelmann	simple/ embedded	1532.854	N/A	N/A
34.	Ingenieurbüro Jens Peupelmann	3-FBG array/ embedded	1546.560 1552.700 1556.840	N/A	N/A
35.	Ingenieurbüro Jens Peupelmann	8-FBG array/ embedded	1530.730 1535.760 1539.700 1543.380 1548.340 1552.480 1556.740 1561.100	N/A	N/A

No.	Company	Sensor configuration	Peak-Wavelength, nm	Reflectivity, %	Transmission loss, dB
36.	Ingenieurbüro Jens Peupelmann	8-FBG array	1531.501 1535.518 1539.198 1544.150 1548.166 1551.570 1556.986 1561.039	N/A	N/A
37.	Telegärtner GmbH	FBG Sensor Rod	1552.595	N/A	N/A

Attachment E Fibre cladding periodical structures

The equation for the propagation constant β of the fundamental mode propagating in the cylindrical medium with the r is given by

$$\beta^2 = \frac{\int_0^{\infty} \left\{ -\left(\frac{d\psi}{dr} \right)^2 + k^2(r)\psi^2 \right\} r dr}{\int_0^{\infty} r\psi^2 dr}. \qquad \text{(E.1)}$$

According to equation (E.1), the dependence $\beta^2 = f(r_0)$ appears as it shown in *Figure A.1*. The spot-size r_0 changes in the range of $\rho - \delta\rho \le r_0 \le \rho + \delta\rho$. The maximal value of r_0 corresponds to the maximal value of β^2. In some cases, it is possible to find β^2 and r_0 analytically. This can be done by assuming that first r_0 derivative is equal zero:

$$\frac{\partial \beta^2}{\partial r_0} = 0. \qquad \text{(E.2)}$$

The maximal value ${\beta^2}_{\max} = 36.03\ \mu m^{-2}$ corresponds to the spot size of 4.5 μm. Taking into consideration that core and cladding refractive indices are constant and equal n_{co} and n_{cl} respectively, the parameters r_0 and β of the single-mode fibre can be calculated after Snyder *et al.*

If values $\psi(r)$, r_0, β, m, $n(r)$ characterising the field in optical fibre are known, then it is possible to calculate a coupling coefficient. In a single-mode optical fibre with periodical structure in the fibre core, the calculation of a coupling coefficient between two propagating modes is provided using the formulation [Bob97b]:

$$\kappa = \frac{\pi}{\beta} \int_0^{\rho} r\psi^2(r) {k_0}^2(r) m(r) dr. \qquad \text{(E.3)}$$

From (E.3) follows that the coupling coefficient is proportional to the modulation coefficient $m(r)$. Therefore, it will be sufficient to calculate κ for the constant value of the modulation coefficient $m(r) = 0.001$. The coupling coefficient $\kappa = 1851\ m^{-1}$ is found for a single-mode fibre with a spot size of 4.5 μm.

According to (E.3), the coupling coefficient κ for a periodical grating on the fibre cladding can be modified to:

$$\kappa = \frac{\pi}{\beta}\int_{\rho}^{\infty} r\psi^2(r)k_0{}^2(r)m(r)dr. \qquad \text{(E.3b)}$$

The coupling coefficient κ for such a case is of 1073 m^{-1} at the modulation coefficient of $m(r) = 0.001$ [Lebi99]. Coupling coefficients for a fibre core and cladding gratings are comparable at the similar modulation coefficient $m(r)$.

Thin grating formed on a fibre cladding

Optical fibres with corrugated cladding can be effectively used for various applications, for example in a case of chemical sensors, which have a contact with the measurand. Optical characteristics of measurand such as refractive index and coefficient of absorption have a direct influence on a reflection coefficient of fibre cladding gratings.

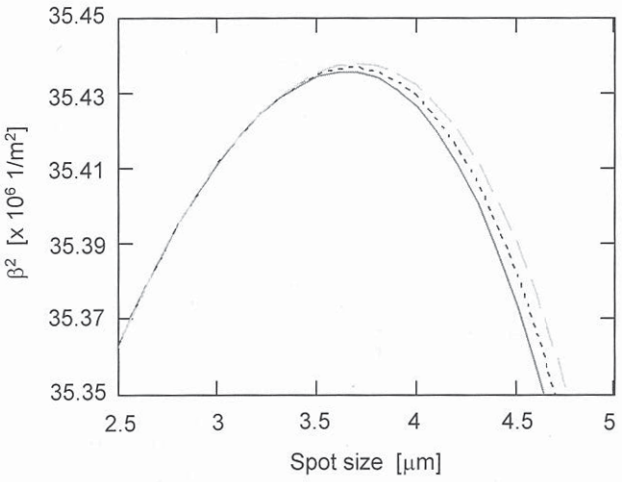

Figure E.1: Dependence of the square of the propagation constant β^2 on the fibre radius r for different types of measurand.

Obtained magnitudes of the coupling coefficient in thin cladding periodical structure are: $\kappa_1 = 10740\ m^{-1}$ for the refractive index of the measurand $n_{m1} = 1.33$, $\kappa_2 = 10692\ m^{-1}$ for $n_{m2} = 1.34$; and $\kappa_3 = 10689\ m^{-1}$ for $n_{m3} = 1.35$.

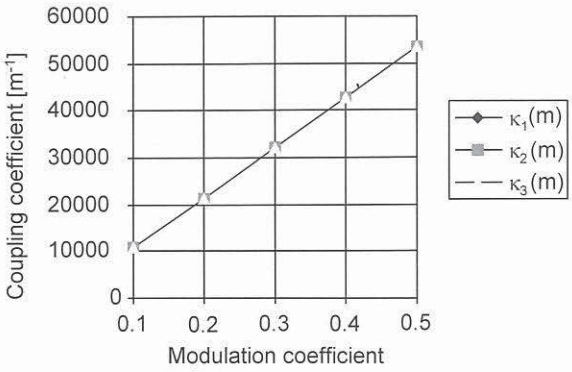

Figure E.2: Dependence of the coupling coefficient $\kappa(r)$ on the modulation coefficient $m(r)$ at a corrugated boundary between a fibre core and cladding for different refractive indices: $\kappa_1(m)$ at n_{m1} = 1.33, $\kappa_2(m)$ at n_{m2} = 1.34; $\kappa_3(m)$ at n_{m3} = 1.35.

As could be seen in *Figure E.2*, the coupling coefficient does not change with a change of external refractive index considerably. That is why the structure will not be sufficiently sensitive to a measurand to be used in a sensor based on the principle of the refractive index change, but the application of such structures can give good results in fibre optic sensors of pressure, strain or temperature.

Corrugated boundary between a core and a cladding

Optical fibre with corrugated boundary between fibre core and cladding is shown schematically in *Figure E.3*.

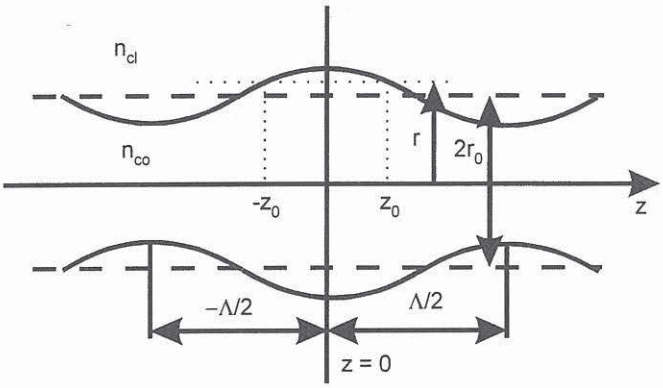

Figure E.3: Optical fibre with corrugated boundary between fibre core and cladding.

Figure E.3 shows corrugated boundary between fibre core and cladding, where n_{co} is a refractive index of a fibre core, n_{cl} is a refractive index of a fibre cladding, $-\frac{\Lambda}{2}$ and $\frac{\Lambda}{2}$ are half periods of the corrugated grating, r_0 is a radius of a fibre core, r is a variable along a fibre axis (a radius of the core-cladding boarder); $-z_0$, z_0 are values of the radius r on the axis z. Mathematically, this boundary could be described as follows

$$r(z)=\rho\left[1+m\cos\left(\frac{2\pi}{\Lambda}z\right)\right], \tag{E.4}$$

where Λ is a period of corrugated grating. The refractive index as a function of the fibre radius r is given by

$$n(r)=\begin{cases} n_{cl}, \text{ when } r>r_0\left[1+m\cos\left(\frac{2\pi}{\Lambda}z\right)\right], \\ n_{co}, \text{ when } r<r_0\left[1+m\cos\left(\frac{2\pi}{\Lambda}z\right)\right] \end{cases} \tag{E.5}$$

In this case, the following correlation will apply:

$$\cos\left(\frac{2\pi}{\Lambda}z\right)=\frac{r-\rho}{m\rho}. \tag{E.6}$$

The last equation can be solved for a $z_{1,2}$, when a boundary radius between a cladding and a core equals r:

$$z_{1,2}=\pm\frac{\Lambda}{2\pi}\arccos\left(\frac{r-\rho}{m\rho}\right)=\pm z_0 \tag{E.7}$$

It is then possible to find coefficients of a Fourier complex array showing periodical change of refractive index of the fibre along the axis z with respect to equations (E.6) and (E.7).

$$C_k(r)=\frac{1}{\Lambda}\int_{-\Lambda/2}^{\Lambda/2} n(r)\exp\left(-j\frac{2\pi}{\Lambda}kz\right)dz= \tag{E.8}$$

$$=\frac{1}{\Lambda}\int_{-\Lambda/2}^{-z_0} n_{cl}\exp\left(-j\frac{2\pi}{\Lambda}kz\right)+\frac{1}{\Lambda}\int_{-z_0}^{z_0} n_{co}\exp\left(-j\frac{2\pi}{\Lambda}kz\right)+\frac{1}{\Lambda}\int_{z_0}^{\Lambda/2} n_{co}\exp\left(-j\frac{2\pi}{\Lambda}kz\right).$$

From equation (E.8) can be found in the general case of a complex coefficient of the Fourier transform:

$$C_k(r)=\frac{n_{co}-n_{cl}}{\pi k}\sin\left[k\arccos\left(\frac{r-r_0}{mr_0}\right)\right]. \tag{E.9}$$

$C_1(r)$ is the most interesting component and according to (E.9):

$$C_1(r)=\begin{cases}\dfrac{n_{co}-n_{cl}}{\pi}\sqrt{1-\left(\dfrac{r-r_0}{mr_0}\right)^2}, & r_0-mr_0\le r\le r_0+mr_0;\\ 0, r<r_0-mr_0, & r>r_0+mr_0.\end{cases} \tag{E.10}$$

The coefficient $C_0(r)$, by substitution $k=0$ into (E.8), equals:

$$C_0(r)=\begin{cases}\dfrac{n_{co}-n_{cl}}{\pi}\arccos\left(\dfrac{r-r_0}{mr_0}\right)+n_{cl}, & r_0-mr_0\le r\le r_0+mr_0;\\ n_{co}, & r<r_0-mr_0;\\ n_{cl}, & r>r_0-mr_0.\end{cases} \tag{E.11}$$

In general, case dependence of refractive index on r given by

$$\begin{aligned}n(r)&=C_0(r)+2C_1(r)\cos\left(\frac{2\pi}{\Lambda}z\right)+\ldots+2C_k(r)\cos\left(\frac{2\pi}{\Lambda}kz\right)+\ldots=\\&=C_0(r)\left[1+2\frac{C_1(r)}{C_0(r)}\cos\left(\frac{2\pi}{\Lambda}z\right)+\ldots\right]=C_0(r)\left[1+m(r)\cos\left(\frac{2\pi}{\Lambda}z\right)+\ldots\right].\end{aligned} \tag{E.12}$$

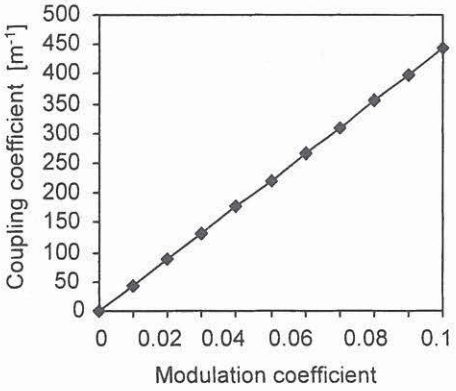

Figure E.4: Dependence of the coupling coefficient κ for corrugated grating core-cladding on coefficient $m(r)$.

So, $m(r)=2\dfrac{C_1(r)}{C_0(r)}$. By substitution of the present value $m(r)$ into (E.3):

$$\kappa = \frac{(2\pi)^3}{\beta\lambda^2} \int_{r_0 - mr_0}^{r_0 + mr_0} r\psi^2(r) C_0(r) C_1(r) dr \,. \tag{E.13}$$

According to (E.15) the coupling coefficient $\kappa(m)$ for a corrugated boundary between fibre core and cladding at $m(r) = 0.001$ is 4.436 m^{-1}. In *Figure E.3*, the Dependence of the coupling coefficient $\kappa(m)$ at the change of $m(r)$ in the range of from 0.001 till 0.1 is shown for refractive indices $n_{co} = 1.453$ and $n_{cl} = 1.45$.

Corrugated boundary between fibre cladding and measurand

The coupling coefficient between modes at corrugated boundary between fibre cladding and measurand appears as follows:

$$\kappa = \left(\frac{2\pi}{\beta\lambda}\right)^3 \int_{\eta - m\eta}^{\eta + m\eta} r\psi^2(r) C_0(r) C_1(r) dr \,. \tag{E.14}$$

where $C_0(r)$, $C_1(r)$ are found from [Lebi99] at the variable displacement of r_0 into r_1, n_{co} into n_{cl} and n_{cl} into n_m; r_1 is an average radius of a corrugated boundary. It is necessary to take into account an average radius of a corrugated boundary r_1 and calculate r_0 for different values of refractive indices of external medium and the constant of propagation β. Values r_0 and β. Estimation for the conditions $r_1 = 6$ µm, $n_m = 1.33$ and $n_m = 1.35$ is provided and values $r_0 = 3.15$ µm $\beta = 5.879$. *Figure E.4* shows dependence of coupling coefficients $\kappa_1(m)$ and $\kappa_2(m)$ at the modulation coefficient $m(r)$ for a corrugated surface and two values of refractive indices $n_{m1} = 1.33$, $n_{m2} = 1.35$. A coupling coefficient can be of larger value for a corrugated cladding at modulation of an external cladding diameter in the range between 0.02 and 0.06 as shown in *Figure E.5*. The coupling coefficient of such a fibre is very sensitive to the refractive index change of measurand.

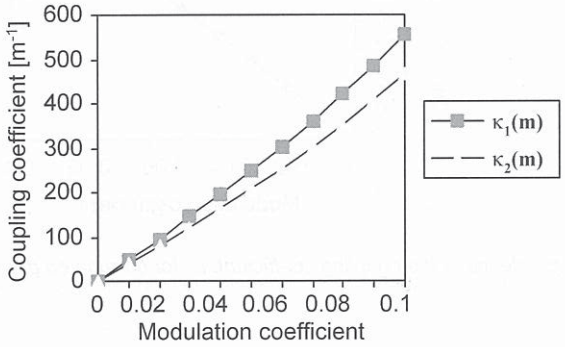

Figure E.5: Dependence of coupling coefficient between modes on the coefficient $m(r)$: $\kappa_1(m)$ at $n_{m1} = 1.33$ and $\kappa_2(m)$ at $n_{m2} = 1.35$.

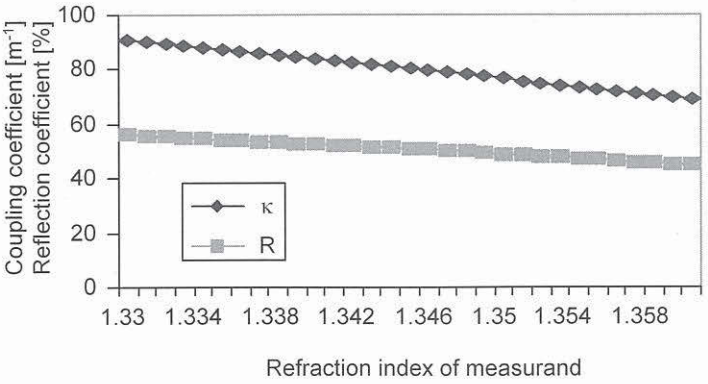

Figure E.6: Dependence of the reflection coefficient R and the coupling coefficient κ on modulation of the measurand refractive index n_m.

Reflection and coupling coefficients between coupled modes at grating length of 7 mm depend on a refractive index modulation of measurand as shown in *Figure E.6*. The sensitivity of the element with corrugated boundary between fibre cladding and measurand can be determined for $m = 0.001$ accordingly by $S = \frac{1}{m}\frac{\Delta\kappa}{\Delta n_S} = \frac{1}{0.001}\frac{\kappa_{1.35} - \kappa_{1.33}}{1.35 - 1.33} = 81.03$, where Δn_m is a change of measurand refractive indices; $\Delta\kappa$ is a change of the coupling coefficient. The coupling coefficient between two propagating modes can be larger using sinusoidal corrugated fibre cladding.

Bibliography

To Chapter 1

[Ala97] F. Alavie, State-of-the-art in the applications of fiber-optic sensors to cementitious composites, Cement and Concrete Composites, Vol. 19, 3-19, 1997.

[Aoy01] H. Aoyama, K. Tanaka, H. Watanabe, N. Takeda, Health-monitoring technologies for alumina-fiber-reinforced plastics, Composite Structures, Vol. 52, 523-531, 2001.

[Bosi02] F. Bosia, J. Botsis, M. Facchini, Ph. Giaccari, Deformation characteristics of composite laminates; part I speckle interferometry and embedded Bragg grating sensor measurements, Composite Science Technology, Vol. 62, 41-54, 2002.

[Boss99] T. Bosselmann, Faseroptische Sensoren für den Einsatz in der Energietechnik, Jena Workshop „Faseroptische Sensortechnik", Oktober 1999.

[Bug00] M. Bugaud, P. Ferdinand, S. Rougeault, V. Dewynter-Marty, P. Parneix, D. Lucas, Health monitoring of composite plastic waterworks lock gates using in-fibre Bragg grating sensors, Smart Materials and Structures, Vol. 9, 322-327, 2000.

[Dak88] J. Dakin and B. Culshaw, Editors, Optical Fibre Sensors: Principles and Components, Artech House, 1988.

[Ferr02] P. Ferreira, G. De Natale, On the possible use of optical fiber Bragg gratings as strain sensors for geodynamical monitoring, Optics and Lasers in Engineering, Vol. 37, 115–130, 2002.

[Fuh98] P. L. Fuhr, D. R. Huston, B. MacCraith, Embedded fiber optic sensors for bridge deck chloride penetration measurement, Optical Engineering, Vol. 37, 4, 1221-1228, 1998.

[Gau99] G. Gauglitz, Faseroptische Chemo- und Biosensoren für Biotechnologie, Umwelt- und Medizintechnik, Jena Workshop „Faseroptische Sensortechnik", Oktober 1999.

[Gra95] K. T. V. Grattan and B. T. Meggitt, Editors, Optical Fibre Sensor Technology, Chapman & Hall, 1995.

[Gra00] K. T. V. Grattan, Dr. T. Sun, Fiber optic sensor technology: an overview, Sensors and Actuators, Vol. 82, 40-61, 2000.

[Hab00] W. R. Habel, Faseroptische Sensoren für hochaufgelöste Verformungsmessungen in der Zementsteinmatrix, Dissertation am FB 9 der TU Berlin, 2000.

[Ham00] Hampton University Professor Develops Touch With Fiber Optics, Fiber Optic Sensors & Systems, Vol. 14, 1, 2, 2000.

[Jĭn97] X. D. Jin, J. S. Sirkis, Simultaneous Measurement of Two Strain Components in Composite structures Using Embedded Fibre Sensors, OSA Technical Digest Series, Vol. 16, 1997.

[Kas99] R. Kashiap, Fibre Bragg Gratings, Academic Press, 1999.

[Lat01] I. Latka, W. Ecke, R. Willsch, A. Reutlinger, Optical fiber grating sensor network for health monitoring in space applications, MAT 2001 Proceedings, A4.2, 87-92, 2001.

[Lau99] K. Lau, L. Zhou, L. Ye, Strain evaluation of Strengthened concrete structures using FBG sensors, Non-destructive Characterisation of Materials IX, AIP, 303-308, 1999.

[Lau01a] K. Lau, L. Yuan, L. Zhou, J. Wu, Ch. Woo, Strain monitoring in FRP laminates and concrete beams using FBG sensors, Composite structures, Vol. 51, 9-20, 2001.

[Leu01] C. K. Y. Leung, Fiber optic sensors in concrete: the future?, NDT&E International, Vol. 34, 85-94, 2001.

[Lop02] J. M. Lopez-Higuera, Handbook of Optical Fibre Sensing Technology, John Wiley & Sons, 2002.

[Maa97] R. Maaskant, T. Alavie, R. M. Measures, G. Tadros, S. H. Rizkalla, A. Guha-Thakurta, Fiber-optic Bragg grating sensors for bridge monitoring, Cement and Concrete Composites, Vol. 19, 21-33, 1997.

[Mas97] S. Mastro, Fabry-Pérot, Bragg grating, and Optical MEMS Sensors for Naval Shipboard Use, Laser Diode and LED Application III, SPIE – The International Society for Optical Engineering, San Diego, 1997.

[McK00] I. McKenzie, R. Jones, I. H. Marshall, S. Galea, Optical fibre sensors for health monitoring of bonded repair systems, www.elsevier.com/locate/compstruct, Composite Structures, Vol. 50, 405-416, 2000.

[Moe01] W. Moerman, W. De. Waele, C. Coppens, L. Taerwe, J. Degrieck, R. Baets, M. Callens, Monitoring of a prestressed concrete girder bridge with fiber optical Bragg grating sensors, Strain, Vol. 37, 4, 151-153, 2001.

[Mou01] A. P. Mouritz, E. Gellert, P. Burchill, K. Challis, Review of advanced composite structures for naval ships and submarines, Composite Structures, Vol. 53, 21-41, 2001.

[Nel00] P. M. Nellen, U. Sennhauser, Characterization and aging of optical fiber Bragg gratings, MicroMat 2000, Berlin, 2000.

[Oka00] Y. Okabe, S. Yashiro, T. Kosaka, N. Takeda, Detection of transverse cracks in CFRP composites using embedded fiber Bragg grating sensors, Smart Materials and Structures, Vol. 9, 832-838, 2000.

[Oka02] Y. Okabe, T. Mizutani, Sh. Yashiro, N. Takeda, The detection of microscopic damages in composite laminates with embedded small-diameter fiber Bragg grating sensors, Composites Science and Technology, in press, 2002.

[OLE02] Fibre Bragg gratings sense vehicle movement on Norwegian road bridge, OLE, Vol. 3, 11, http://optics.org, 2002.

[Oth99] A. Othonos, K. Kalli, Fiber Bragg gratings: Fundamentals and Applications in Telecommunications and Sensing, Artech House, 1999.

[Pet02] K. Peters, M. Studer, J. Botsis, Embedded optical fiber Bragg grating sensors for the measurement of crack bridging forces in composites, Smart Structures Proceedings, 2002.

[Rao97] Y.-J. Rao, In-fibre Bragg grating sensors, Measurement Science and Technology, Vol. 8, 355-375, 1997.

[Schu98] W. L. Schulz, E. Udd, J. M. Seim, G. E. McGill, Advanced fiber grating strain sensor systems for bridges, structures, and highways, www.bluerr.com, 1998.

[Ten01] R. C. Tennyson, A. A. Mufti, S. Rizkalla, G. Tadros, B. Benomorkane, Structural health monitoring of innovative bridges in Canada with fiber optic sensors, Smart Materials and Structures, Vol. 10, 3, 560-573, 2001.

[Tru99b] M. Trutzel, O. Krumpholz, Ch. Boller, Anwendungspotential faseroptischer Sensoren in Luft & Raumfahrt und Fahrzeugbau, Jena Workshop „Faseroptische Sensortechnik", Oktober 1999.

[Tru01] M. N. Trutzel, Dehnungsermittlung mit faseroptischen Bragg-Gitter-Sensoren: Grundlagen, Eigenschaften und Anwendungen, Doktorarbeit, Berlin, 2001.

[Udd96] E. Udd, D. Nelson, C. Lawrence, B. Ferguson, Three axis strain and temperature fiber optic grating sensor, Proceedings of SPIE, Vol. 2718, 104-108, 1996.

[Voh98] S. T. Vohra, B. Althouse, G. Johnson, S. Vurpillot, D. Inaudi, Quasi-static strain monitoring during the 'Push' phase of a Box-Girder Bridge using fiber Bragg grating sensors, European workshop on FOS, Scotland, 1998.

[Wan99] X. D. Wang, S. A. Meguid, Micromechanical modeling of FRCs containing matrix cracks and partially debonded fibers, Journal of Engineering materials and technology, Vol. 121, 445-452, 1999.

[Wie00] S. Wiese, J. Wiechein, W. Kowalsky, Fiber optical sensors in concrete, Proceedings of IMEKO 2000.

[Woo00] K. Wood, T. Brown, R. Rogowski, B. Jensen, Fiber optic sensors for health monitoring of morphing airframes: I. Bragg grating strain and temperature sensor, Smart Materials and Structures, Vol. 9, 163-169, 2000.

To Chapter 2

[Ala93] A. T. Alavie, S. E. Karr, A. Othonos, R. M. Measures, A multiplexed Bragg grating fiber laser sensor system, IEEE Photonnics Technology Letters, Vol. 5, 9, 1112-1114, 1993.

[And94] D. Z. Anderson, T. Erdogan, V. Mizrahi, Method for forming a Bragg grating in an optical medium, United States Patent # 5,327,515, July 5, 1994.

[AOS] Fiber Bragg-Grating Sensors, www.aos-fiber.com.

[Atk97] R. M. Atkins and R. P. Espindola, Photosensitivity and Grating Writing in Hydrogen Loaded Germanosilicate Core Optical Fibers at 325 and 351 nm, Applied Physics Letters, Vol. 70, 9, 1997.

[Baa02] C. Baack, Researchers forge ahead with component advances, Fibre Systems, Vol. 4, 5-8, 2002.

[Bal94] G. A. Ball, W. W. Morey, P. K. Cheo, Fiber laser source/analyser for Bragg grating sensor array interrogation, IEEE Journal of Lightwave Technology, Vol. 12, 700-703, 1994.

[Bar01] H. Bartelt, W. Ecke, S. Grimm, V. Hagemann, M. Rothhardt, Von der photoempfindlichen Faser zum Fasergitter-Sensorsystem, Verbundprojekt 1998-2001 Abschlussbericht, Band 75, 2001.

[Ber00] J. W. Berthold, Measurement of Axial and Bending Strain in Pipelines Using Bragg Grating Sensors, Presented at the SPIE Environmental and Industrial Sensing Conference MTI 00-13, Boston, Massachusetts, October 9, 2000.

[Bet01] D. Betz, M. N. Trutzel, L. Staudigel, O. Krumpholz, Struktur-integrierbares Fasergitter-Sensornetzwerk zur Detektion von Bauteil-Verformungen, Verbundprojekt 1998-2001 Abschlussbericht, Band 75, 2001.

[Bha97] V. Bhatia, D. K. Campbell, D. Sherr, T. G. D'Alberto, N. A. Zabaronick, G. A. Ten Eyck, K. A. Murphy, R. O. Claus, Temperature-insensitive and strain-insensitive long-period grating sensors for smart structures, Optical Engineering, Vol. 36, 7, 1872-1876, 1997.

[Bil96] F. C. Bilodeau, B. Y. Malo, J. A. Hull, D. C. Johnson, K. O. Hill, United States Patent # 5,495,548, February 27, 1996.

[Bob97a] Ya. V. Bobitski, V. M. Fitio, S. Y. Zakalyk, Model of light propagation in fibreoptic Bragg grating, 4th Internernational Conference L'viv, Vol. 2, 19-21, 1997.

[Boss01] T. Bosselmann, H. Hertsch, J. Kaiser, P. Krämmer, N. Theune, M. Willsch, Entwicklung und Erprobung von Fasergitter-Sensoren für Energieversorgungsanlagen am Beispiel eines Kraftwerksgenerators, Verbundprojekt 1998-2001 Abschlussbericht, Band 75, 2001.

[Bre99] J. F. Brebban, D. LaBrake, G. A. Beauchesne, R. P. Pepin, United States Patent # 5,912,999, June 15, 1999.

[Byr96] K. Ch. Byron, United States Patent # 5,694,502, June 20, 1996.

[Byr98] K. Ch. Byron, United States Patent # 5,730,888, March 24, 1998.

[Cha99] C. C. Chan, W. Jin, M. S. Demokan, Enhancement of measurement accuracy in fiber Bragg grating sensors by using digital signal processing, Optics & Laser Technology, Vol. 31, 299-307, 1999.

[Cha00] C. C. Chan, J. M. Gong, W. Jin, M. S. Demokan, Investigation of unwanted interferometric signals in a fiber Bragg grating sensor using a tunable laser and a first derivative interrogation technique, Optics Communications, Vol. 173, 203–210, 2000.

[Cha01] C. C. Chan, Y. J. Gao, K. T. Lau, H. L. Ho, L. M. Zhou, W. Jin, Characterization of crosstalk of a TDM FBG sensor array using a laser source, Optics & Laser Technology, Vol. 33, 299–304, 2001.

[Chan99] P. K. C. Chan, W. Jin, M. S. Demokan, Multiplexing of fiber Bragg grating sensors using subcarrier intensity modulation, Optics & Laser Technology, Vol. 31, 345-350, 1999.

[Cul00] B. Culshaw, Measuring strain using optical fibres, Strain, Vol. 36, 3, 105-113, 2000.

[Dak88] J. Dakin and B. Culshaw, Editors, Optical Fibre Sensors: Principles and Components, Artech House, 1988.

[Dak97] J. P. Dakin, *et al.*, New multiplexing scheme for monitoring fiber optic Bragg grating sensors in the coherence domain, Proceedings of the OFS Conference, OFS-12, Williamsburg, VA, USA, 31-34, 1997.

[Dav95] M. Davis, A. D. Kersey, Matched-filter interrogation technique for fibre Bragg grating arrays, Electronic Letters, Vol. 31, 822-823, 1995.

[Dav96] M. A. Davis, A. D. Kersey, Separating the temperature and strain effects on fiber Bragg grating sensors using stimulated Brillouin scattering, Proceedings of SPIE, Vol. 2718, 270-278, 1996.

[Dav96b] M. A. Davis, D. G. Bellemore, T. A. Berkoff, A. D. Kersey, M. A. Putnam, R. L. Idriss, M. Kodinduma, Fiber optic sensor system for bridge monitoring with both static load and dynamic modal sensing capabilities, Proceedings of SPIE, Vol. 2946, 219-232, 1996.

[Dew98] V. Dewynter-Marty, P. Ferdinand, E. Bocherens, R. Carbone, H. Beranger, S. Bourasseau, M. Dupont, D. Balageas, Embedded Fiber Bragg Grating Sensors for Industrial Composite Cure Monitoring, Journal of Intelligent Material Systems and Structures, Vol. 9, 785-787, 1998.

[Dye99] Sh. D. Dyer, K. B. Rochford, A. H. Rose, Fast and accurate low-coherence interferometric measurements of fiber Bragg grating dispersion and reflectance, OPTICS EXPRESS 5, 11, 262-266, 1999.

[El-89] M. El-Sherif, United States Patent # 4,842,405, June 27, 1989.

[Epw97] Epworth *et al.*, United States Patent # 5,619,603, April 1997.

[Erd94] T. Erdogan, V. Mizrahi, Fiber phase gratings reflect advances in lightwave technology, Laser Focus World, Vol. 2, 73-80, 1994.

[Erd97] T. Erdogan, Fiber grating spectra, Journal of Lightwave Technology, Vol. 15, 8, 1277-1294, 1997.

[Ezb96] A. Ezbiri, R. P. Tatam, Interrogation of low finesse optical fibre Fabry-Pérot interferometers using a four wavelength technique, Measurement Science and Technology, Vol. 7, 2, 117-120, 1996.

[Ezb97] A. Ezbiri, R. P. Tatam, Five wavelength interrogation technique for miniature fibre optic Fabry-Pérot sensors, Optical Communications, Vol. 133, 62-66, 1997.

[Ezb98] A. Ezbiri, S. E. Kanellopoulos, V. A. Handerek, High resolution instrumentation system for fibre-Bragg grating aerospace sensors, Optical Communications, Vol. 150, 43–48, 1998.

[Fer99] L. A. Ferreira, E. V. Diatzikis, J. L. Santos, F. Farahi, Demodulation of fiber Bragg grating sensors based on dynamic tuning of a multimode laser diode, Applied Optics, Vol. 38, 22, 4751-4759, 1999.

[Fla99] D. A. Flavin, R. McBride, J. D. C. Jones, Short-scan interferometric interrogation and multiplexing of fibre Bragg grating sensors, Optics Communications, Vol. 170, 347–353, 1999.

[Fuh98] P. L. Fuhr, D. R. Huston, B. MacCraith, Embedded fiber optic sensors for bridge deck chloride penetration measurement, Optical Engineering, Vol. 37, 4, 1221-1228, 1998.

[Fuh00] P. L. Fuhr, S. J. Spammer, Y. Zhu, A novel signal demodulation technique for chirped Bragg grating strain sensors, Smart Materials and Structures, Vol. 9, 85-94, 2000.

[Gei99] U. Geisler, I. Baumann, Ausgewählte Anwendungen für Faser-Bragg-Gitter-Sensoren, Jena Workshop „"Faseroptische Sensortechnik, Oktober 1999.

[Gen98] Generic requirements for fiber optic branching components, GR-1209-CORE, Issue 2, Telcordia, Feb. 1998.

[Gle89] W. H. Glenn, G. Meltz, E. Snitzer, United States Patent # 4,807,950, February 28, 1989.

[Glö99] Glötzl Europe Sensors N.V., Strain sensors, Jena Workshop, October 1999.

[Gra95] K. T. V. Grattan and B. T. Meggitt, Editors, Optical Fibre Sensor Technology, Chapman & Hall, 1995.

[Gra00] K. T. V. Grattan, Dr. T. Sun, Fiber optic sensor technology: an overview, Sensors and Actuators, Vol. 82, 40-61, 2000.

[Gue02] J. A. Guemes, J. M. Menendez, Response of Bragg grating fiber-optic sensors when embedded in composite laminates, Composites Science and Technology, Vol. 62, 959-966, 2002.

[Hab98] W. R. Habel, B. Hillemeier, A. Bismarck, J. Springer, How to achieve the desired strain transfer for fiber-optic microdeformation measurements in cementitious building materials at early ages?, European Workshop on FOS, 1998.

[Hab01] W. R. Habel, Faseroptische Sensorik für Bauwerksüberwachung, Workshop, Faseroptische Sensortechnik, Erlangen 20 September 2001.

[Hag00] V. Hagemann, M. N. Trutzel, L. Staudigel, M. Rothhard, H. R. Müller, O. Krumpholz, New evidence for the excellent fibre strength of single-pulse draw-tower Bragg gratings, 2000.

[Har98] F. M. Haran, J. K. Rew, P. D. Foote, A strain-isolated fibre Bragg grating sensor for temperature compensation of fibre Bragg grating strain sensors, Measurement Science and Technology, Vol. 9, 1163-1166, 1998.

[Hen] S. Hendow, Gratings, amplifiers and sources for high spectral efficiency systems, Southampton Photonics, Inc.

[Hil78] K. O. Hill, Y. Fujii, D. C. Johnson, and B. S. Kawasaki, Photosensitivity in Optical Fiber Waveguides: Application to Reflection Filter Fabrication, Applied Physics Letters, Vol. 32, 647, 1978.

[Hil84] K. O. Hill, B. S. Kawasaki, D. C. Johnson, Y. Fujii, United States Patent # 4,474,427, October 2, 1984.

[Hil91] K. O. Hill, B. Malo, F. Bilodeau, D. C. Johnson, United States Patent # 5,104,209, February 19, 1991.

[Hil94] K. O. Hill, B. Y. Malo, F. C. Bilodeau, D. C. Johnson, United States Patent # 5,367,588, November 22, 1994.

[Hil96] K. O. Hill, Fiber Bragg Gratings: Properties and sensing Applications, Eleventh International Conference on Optical Fiber Sensors, Advanced Sensing Photonics, Japan Society of Applied Physics, 1996.

[Hil97] K. O. Hill, G. Meltz, Fiber Bragg grating technology fundamentals and overview, Journal of Lightwave Technology, Vol. 15, 8, 1263-1276, 1997.

[Hoc79] G. B. Hocker, Fiber-optic sensing of pressure and temperature, Applied Optics, Vol. 18, 9, 1979.

[Hua94] S. Huang, M. M. Ohn, M. LeBlanc, R. Lee, R. M. Measures, Fiber optic intra-grating distributed strain sensor, Proceedings of SPIE, Vol. 2294, 81-92, 1994.

[Hua95a] S. Huang, M. LeBlanc, M. M. Ohn, R. M. Measures, Bragg intragrating structural sensing, Applied Optics, Vol. 34, 22, 5003-5009, 1995.

[Hua95b] S. Huang, M. M. Ohn, R. M. Measures, A novel Bragg grating distributed-strain sensor based on phase measurements, Proceedings of SPIE, Vol. 2444, 158-169, 1995.

[Hua96] S. Huang, M. M. Ohn, R. M. Measures, Phase-based Bragg intragrating distributed strain sensor, Applied Optics, Vol. 35, 7, 1135-1142, 1996.

[Hua98] S. L. Huang, W. M. Chen, K. D. Bennett, Optical sensors for smart civil infrastructures, Proceedings of SPIE, Vol. 3555, 266-271, 1998.

[Jen00] A. E. Jensen, G. B. Havsgard, K. Pran, G. Wang, S. T. Vohra, M. A. Davis, A. Dandridge, Wet deck slamming experiments with a FRP sandwich panel using a network of 16 fibre optic Bragg grating strain sensors, Composites: Part B, Vol. 31, 187–198, 2000.

[Jin97] X. D. Jin, J. S. Sirkis, Simultaneous Measurement of Two Strain Components in Composite structures Using Embedded Fibre Sensors, OSA Technical Digest Series, Vol. 16, 1997.

[Joh00] D. Johlen, Bragg Gitter und optische Wellenleiter in UV Schreibtechnik, Fortschritt-Berichte VDI, Vol. 620, 2000.

[Jun93] E. D. Jungbluth, Phase-mask photolithography makes Bragg gratings in fiber, Laser Focus World, Vol. 5, 33-35, 1993.

[Kal195] K. Kalli, *et al.*, Wavelength division and spatial multiplexing using tandem interferometers for Bragg grating sensor networks, Optical Letters, Vol. 20, 2544-2546, 1995.

[Kas99] R. Kashiap, Fibre Bragg Gratings, Academic Press, 1999.

[Ker92] A. D. Kersey, Multiplexed fiber optic sensors, Proceedings of SPIE, Vol. 1797, 161, 1992.

[Kim92] K. S. Kim, A model of embedded fiber optic Fabry-Pérot temperature and strain sensors, Ph. D. Dissertation, Stanford University, 1992.

[Kli96] T. Klink, K. Gaber, Verbesserung der Wirksamkeit von Fasern im Beton und in Sanierung durch deren Vorspannung, Internationales Zeitschrift für Bauinstandsetzen Vol. 2, 3, 1996.

[Kro91] D. M. Krol, R. M. Atkins, P. J. Lemaire, Photoinduced second-harmonic generation and luminescence of defects in Ge-doped silica fibers, Proceedings of SPIE, Vol. 1516, 38-46, 1991.

[Lat01] I. Latka, W. Ecke, R. Willsch, A. Reutlinger, Optical fiber grating sensor network for health monitoring in space applications, MAT 2001 Proceedings, A4.2, 87-92, 2001.

[Lau01] K. Lau, L. Yuan, L. Zhou, J. Wu, Ch. Woo, Strain monitoring in FRP laminates and concrete beams using FBG sensors, Composite structures, Vol. 51, 9-20, 2001.

[Law95] C. M. Lawrence, D. V. Nelson, E. Udd, Measurement of transverse strains with fiber Bragg gratings, Proceedings of SPIE, Vol. 2444, p. 136-147, 1995.

[Lebb92] M. S. Lebby, M. P. Norman, United States Patent # 5,116,461, May 26, 1992.

[Lebi02] S. Lebid, T. Gutmann, W. Habel, J. Peupelmann, Ch. Schäffer, Influence of Perturbing Effects on Composite-embedded Fibre Bragg Grating Signals, Mittweida, IWKM 15, 41-46, 2002.

[LeBl96] M. LeBlanc, S. Y. Huang, M. Ohn, R. M. Measures, A. Guemes, A. Othonos, Distributed strain measurement based on a fiber Bragg grating and its reflection spectrum analysis, Optoelectronics Letters, Vol. 21, 17, 1405-1407, 1996.

[LeBl00] M. LeBlanc, A. D. Kersey, Distributed, intra grating sensing by Fabry-Pérot wavelength tuned low-coherence interferometry, OTuC5-1, 52-55, 2000.

[Lew97] K. Lewotsky, Doping eliminates hydrogen loading, Laser Focus World, Vol. 4, 1997.

[Li01] X. Ch. Li, F. Prinz, J. Seim, Thermal behavior of metal embedded fiber Bragg grating sensor, Smart Materials and Structures, Vol. 10, 575-579, 2001.

[Lin98] G. Lin, L. Wang, C. C. Yang, M. C. Shih, T. J. Chuang, Thermal performance of metal-clad fiber Bragg grating sensors, IEEE Photonics Technology Letter, Vol. 10, 3, 406, 1998.

[Lo97] Y.-L. Lo, J. S. Sirkis, Simple method to measure temperature and Axial Strain Simultaneously Using One In-Fiber Bragg Grating Sensor, The International Society for Optical Engineering, Vol. 3042, 1997.

[Lop02] J. M. Lopez-Higuera, Handbook of Optical Fibre Sensing Technology, John Wiley & Sons, 2002.

[Mae99] M. Maeda, A. Takada, Tunable wavelength light source miniaturisation and wavelength control technology, ANDO Technical Bulletin, Vol. 9, 46-53, 1999.

[Mag97] S. Magne *et al.*, State-of-strain evaluation with fiber Bragg grating rosettes: application to discrimination between strain and temperature effects in fiber sensors, Applied Optics, Vol. 36, 36, 1997.

[Mah78] H. F. Mahlein, Filter für Lichtleitfasern, Deutsches Patent, Offenlegungs-Schrift 26 32 861, 21. Juli 1978.

[Mal93] B. Malo, *et al.*, Point-by-point fabrication of micro-Bragg gratings in photosensitive fiber using single eximer pulse refractive index modification technique, Electronic Letters, 29, 1668-1669, 1993.

[Mar92] M. J. Marrone, A. D. Kersey, A. D. Dandridge, Polarization-independent array configurations based on Michelson interferometer networks, Proceedings of SPIE, Vol. 1797, 196, 1992.

[Mart99] T. Martynkien, W. Urbanczyk, W. Bock, T. Smolnicki, Modelowanie spektralnych wlasciwosci swiatlowodow z eliptycznym rdzeniem, Proceedings of VII Conference "Optical Fibres and their Application", Krasnobrod, Poland, 1999.

[Mas97] S. Mastro, Fąbry-Pérot, Bragg grating, and Optical MEMS Sensors for Naval Shipboard Use, Laser Diode and LED Application III, SPIE – The International Society for Optical Engineering, San Diego, 1997.

[McK00] I. McKenzie, R. Jones, I. H. Marshall, S. Galea, Optical fibre sensors for health monitoring of bonded repair systems, www.elsevier.com/locate/compstruct, Composite Structures, Vol. 50, 405-416, 2000.

[Mea92] R. M. Measures, S. Melle, K. Liu, Wavelength demodulated Bragg grating fiber optic sensing systems for addressing smart structure critical issues, Smart Materials and Structures, Vol. 1, 36-44, 1992.

[Mea98] R. M. Measures, M. M. Ohn, S. Y. Huang, J. Bigue, N. Y. Fan, Tunable laser demodulation of various fiber Bragg grating sensing modalities, Smart Materials and Structures, Vol. 7, 2, 237-247, 1998.

[Mec97] S. E. Mechels, J. B. Schlager, D. L. Franzen, Accurate measurements of the zero-dispersion wavelength in optical fibers, Journal of Research of the National Institute of Standards and Technology, Vol. 102, 3, 333-347, 1997.

[Mer96] C. I. Merzbacher, A. D. Kersey, E. J. Friebele, Fiber optic sensors in concrete structures: a review, Smart Materials and Structures, Vol. 5, 196-208, 1996.

[Mel89] G. Meltz, W. W. Morey, W. H. Glenn, Formation of Bragg Gratings in Optical Fibers by a Transverse Holographic Method, Optoelectronic Letters, Vol. 14, 15, 1989.

[Mil00] C. M. Miller, United States Patent # 6,044,189 March 28, 2000.

[Miz93] V. Mizrahi, P. J. Lemaire, T. Erdogan, W. A. Reed, D. J. DiGiovanni, R. M. Atkins, Ultraviolet laser fabrication of ultrastrong optical fiber gratings and of germania-doped channel waveguides, Applied Physics Letters, Vol. 63, 13, 1727-1729, 27, 1993.

[MOI] Fiber Bragg grating swept laser interrogator, www.micronoptics.com.

[More89] W. W. Morey, G. Meltz, W. H. Glenn, Bragg Grating Temperature and Strain Sensors, Sixth International Conference on Optical Fiber Sensors, Heidelberg, Germany, 1989.

[Mori99] T. Mori, T. Kaneko, T. Iwasaki, Development of a high-resolution optical spectrum analyser, ANDO Technical Bulletin, Vol. 9, 46-53, 1999.

[Nel01] Ph. M. Nellen, Frühwarnung dank zuverlässiger faseroptischer Sensoren, Workshop, Faseroptische Sensortechnik, Erlangen 20 September 2001.

[Ngu97] T. A. Nguty, R. J. Potton, Photochemical changes in hydrogen-loaded optical fibres with application to Bragg grating formation, Measurement Science and Technology, Vol. 8, 1055-1058, 1997.

[Ohn97] M. M. Ohn, S. Y. Huang, R. M. Measures, J. Chwang, Arbitrary strain profile measurement within fibre gratings using interferometric Fourier transform technique, Electronic Letters, Vol. 33, 14, 1242-1243, 1997.

[Oth99] A. Othonos, K. Kalli, Fiber Bragg gratings: Fundamentals and Applications in Telecommunications and Sensing, Artech House, 1999.

[Rao96] Y. J. Rao, A. B. Lobo Ribeiro, D. A. Jackson, L. Zhang, I. Bennion, Simultaneous spatial, time and wavelength division multiplied in-fibre grating sensing network, Optical Communications, Vol. 125, 53-58, 1996.

[Rao97] Y.-J. Rao, In-fibre Bragg grating sensors, Measurement Science and Technology, Vol. 8, 355-375, 1997.

[Rei98] M. Reid, *et al.* Temperature dependence of fiber optic Bragg gratings at low temperature, Optical Engineering, Vol. 37, 1, 237, 1998.

[Ros00] A. H. Rose, C.-M. Wang, S. D. Dyer, Round Robin for Optical Fiber Bragg Gratings Metrology, Journal of Research of the National Institute of Standards and Technology, Vol. 105, 6, 839-866, 2000.

[Rus93] P. J. Russel, J. Archambault, L. Reekie, Fibre gratings, Physics World, Vol. 6, 41, 1993.

[Schi01] H. Schillinger, A. Görtler, Pulsschlag aus Licht: Industrie-Eximerlaser für die Produktion von Faser-Bragg-Gittern, Lasertechnik, Carl Hanser Verlag, München, Vol. 109, 66-69, 2001.

[Schl99] E. Schlattner, T. Klink, V. Slowik, Faser-Bragg-Sensoren in Bauwerken, Forschungsbericht 1999.

[Sir98] J. S. Sirkis, Using Bragg grating sensor system in construction materials and bridges: perspectives and challenges, Proceedings of the International Workshop on "Fiber Optic Sensors for Construction Materials and Bridges", 44-61, 1998.

[Slo98] V. Slowik, E. Schlattner, T. Klink, Fibre Bragg grating sensors in concrete technology, Laser, Vol. 3, 109-119, 1998.

[Slo01] V. Slowik, T. Klink, R. Krumbach, Sensoren für die langenzeitige Bauwerksüberwachung, VDI-Berichte 1599, 2001.

[Sny81b] A. W. Snyder, J. D. Love, Optical Wave theory, Chapmann and Hall, London, 1981.

[Spi01] V. V. Spirin, M. G. Shlyagin, S. V. Miridonov, I. Marquez, Temperature-insensitive strain measurement using differential double Bragg grating technique, Optics & Laser Technology, Vol. 33, 43-46, 2001.

[Stee95] R. J. Van Steekiste, Theory of Fiber optic Strain and temperature sensors, Ph.D. Dissertation, Stanford University, 1995.

[Stef94] K. Steffens, Experimentell gestützte Untersuchung des Trag- und Verformungsverhaltens der Brücke über die Stepnitz, Bautechnik, 71, 782-791, 1994.

[Stu00] K. Stump, T.-K. Plant, Y. Sun, Variable wavelength fibre Bragg gratings written with diffractive optical element, Electronic Letters, Vol. 36, 6, 567-569, 2000.

[Sva86] A. S. Svahin, V. A. Sytchugov, T. V. Tulajkova, Dispersion element on the polished surface of the singlemode fiber waveguide, Quantovaja Eliektronika, Vol. 13, 2, 440-442, 1986.

[Sva89] A. S. Svahin, V. A. Sytchugov, A. E. Tihomirov, Focusing grating on the fiber and method of it fabrication, Pisjma v ZTF, Vol. 15, 12, 13-16, 1989.

[Syt94] V. A. Sytchugov, A. S. Svahin, A. E. Tihomirov, Holographic focusing gratings on the surface of optical waveguides, Quantovaja Eliektronika, Vol. 21, 5, 481-482, 1994.

[Tan96] S. Tanaka, K. Yoshida, Y. Ohtsuka, A new type of birefringent fiber fabricated for sensor use, 11th International Conference on Optical Fiber Sensors, Advanced Sensing Photonics, Japan Society of Applied Physics, 1996.

[Tel] Fibre optic sensor technology offers new opportunities for the monitoring of structures, (equipment manufacturer), Telegärtner Gerätebau GmbH, www.geraetebau.telegaertner.com/news/index.html.

[Ten00] R. C. Tennyson, T. Coroy, G. Duck, G. Manuelpillai, P. Mulvihill, D. J. F. Cooper, P. W. E. Smith, A. A. Mufti, S. J. Jalali, Fibre optic sensors in civil engineering structures, Canadian Journal of Civil Engineering, Vol. 27, 880-889, 2000.

[Teu00] J. Teunissen, Ch. Helmig, D. Peier, Möglichkeit des Einsatzes faseroptischer Bragg-Gitter zur On-Line-Temperaturmessung, VDI Berichte 1530, 2000.

[Tod01] M. D. Todd, G. A. Johnson, B. L. Althouse, A novel Bragg grating sensor interrogation system utilizing a scanning filter, a Mach-Zehnder interferometer and a 3×3 coupler, Measurement Science and Technology, Vol. 12, 7, 771-777, 2001.

[Tru01] M. N. Trutzel, Dehnungsermittlung mit faseroptischen Bragg-Gitter-Sensoren: Grundlagen, Eigenschaften und Anwendungen, Doktorarbeit, Berlin, 2001.

[Var96] M. Varasi, M. Signorazzi, A. Vannucci, J. Dunphy, A high-resolution integrated optical spectrometer with applications to fibre sensor signal processing, Measurement Science and Technology, Vol. 7, 173–178, 1996.

[Voe99] M. R.-H. Voet, E. Schoubs, S. Fischer, Innovative Anwendungen von Glasfasersensorik in der Geo- und Bauwerktechnik, Jena Workshop "Faseroptische Sensortechnik", Oktober 1999.

[Voh98] S. T. Vohra, B. Althouse, G. Johnson, S. Vurpillot, D. Inaudi, Quasi-static strain monitoring during the 'Push' phase of a Box-Girder Bridge using fiber Bragg grating sensors, European workshop on FOS, Scotland, 1998.

[Vol96] M. Volanthen, H. Geiger, M. J. Cole, R. I. Laming, J. P. Dakin, Low coherence technique to characterize reflectivity and time delay as a function of wavelength within a long fibre grating, Electronic Letters, Vol. 32, 8, 757-758, 1996.

[Vri98] M. de Vries, V. Bhatia, T. D'Alberto, V. Arya, R.O. Claus, Photoinduced grating-based optical fiber sensors for structural analysis and control, Engineering Structures, Vol. 20, 3, 205-210, 1998.

[Wag96] R. B. Wagreich, W. A. Atia, H. Singh, J. S. Sirkis, Effects of diametric load on fiber Bragg gratings fabricated in low birefringent fiber, Electronic Letters, Vol. 26, 6, 1223-1224, 1996.

[Wei00] C. Y. Wei, S. W. James, C. C. Ye, R. P. Tatam, P. E. Irving, Application issues using fibre Bragg gratings as strain sensors in fibre composites, Strain, Vol. 36, 143-150, 2000.

[Weis94] R. S. Weis, A. D. Kersey, T. A. Berkoff, A four-element fiber grating sensor array with phase-sensitive detection, IEEE Photonics Technology Letters, Vol. 6, 1469-1472, 1994.

[Weis01] R. S. Weis, B. L. Bachim, Scource-noice-induced resolution limits of interferometric fibre Bragg grating sensor demodulation systems, Measurement Science and Technology, Vol. 12, 7, 771-777, 2001.

[Will00] R. Willsch, Technical Trends, Potential Applications and Market Development in Optical Fibre Sensor Technology, www.fos-en.net, 2000.

[Wils01] A. Wilson, S. W. James, R. P. Tatam, Time-division-multiplexed interrogation of fibre Bragg grating sensors using laser diodes, Measurement Science and Technology, Vol. 12, 181-1877, 2001.

[Xie02] F. Xie, S. Zhang, Y. Li, S. B. Lee, Multiple in-fiber Bragg gratings sensor with a grating scale, Measurement, Vol. 31, 139–142, 2002.

[Yab99] E. Yablonovitch, R. B. Vrijen, Optical projection lithography at half the Raleigh resolution limit by two-photon exposure, Optical Engineering, Vol. 38, 2, 334-338, 1999.

[Zha02] M. Zhang, C. C. Chan, D. N. Wang, J. M. Gong, W. Jin, M. S. Demokan, Time division multiplexed strain system by the use of dual-wavelength fiber Bragg gratings, Sensors and Actuators A, Vol. 3346, 1-5, 2002.

To Chapter 3

[Bob97b] Y. Bobitski, W. Fitio, S. Lebid, T. Wanchytski, Reflection spectrum calculation in optical fiber periodical structures (PS), Proc. 3rd International Conf. MECHATRONIKA'97, Warszawa (Poland), 775-781, 1997.

[Col73] R. Collier, H. Burkhart, L. Lyn, Optical Holography, Myr, 686, 1973.

[Corn74] G. Corn, T. Corn, Mathematical manual, Nauka, 832, 1974.

[Erd97] T. Erdogan, Fiber grating spectra, Journal of Lightwave Technology, Vol. 15, 8, 1277-1294, 1997.

[Gaf97] R. Gafsi, A. Malki, F. Ahdad, P. Lecoy, J. Bures, Static stress optical-fiber sensor, Sensors and Actuators A, Vol. 62, 501-505, 1997.

[Gaf00] R. Gafsi, M. A. El-Schrif, Analysis of induced-birefringence effects on fiber Bragg gratings, Opt. Fib. Tech., Vol. 6, 299-323, 2000.

[Gia81] P. D. Gianino, B. Bendow, Calculations of stress-induced changes in the transverse refractive-index profile of optical fibers, Applied Optics, Vol. 20, 3, 430-434, 1981.

[Gon01] D. A. Gonzales, J. L. Arce-Diego, A. Cobo, J. M. Lopez-Higuera, Spectral modelling of curved long-period fibre gratings, Measurement Science and Technology, Vol. 12, 786-792, 2001.

[Hab98] W. R. Habel, B. Hillemeier, A. Bismarck, J. Springer, How to achieve the desired strain transfer for fiber-optic microdeformation measurements in cementitious building materials at early ages?, European Workshop on FOS, 1998.

[Hil97] K. O. Hill, G. Meltz, Fiber Bragg grating technology fundamentals and overview, Journal of Lightwave Technology, Vol. 15, 8, 1263-1276, 1997.

[Kas99] R. Kashiap, Fibre Bragg Gratings, Academic Press, 1999.

[Kay90] G. Kayno, Acoustic waves. Devices, visualization and analogue processing of signals, Myr, 652, 1990.

[Kum84] A. Kumar, R. K. Varshney, Propagation characteristics of highly elliptical core optical waveguides: a perturbation approach, Opt. Quant. El., Vol. 16, 1984.

[Lebi98] S. Yu. Lebid, Y. W. Bobitski, W. M. Fitio, Fibre-optic temperature sensor, Patent on invention of Ukraine, No. 25555, 30.10.1998.

[Lov84] J. D. Love, A. W. Snyder, Optical Waveguide Theory, Kluwer Academic Publishers, 1984.

[Mär95] R. März, Integrated Optics, Artech Hause, Boston, 1995.

[Mart99] T. Martynkien, W. Urbanczyk, W. Bock, T. Smolnicki, Modelowanie spektralnych wlasciwosci swiatlowodow z eliptycznym rdzeniem, Proceedings of VII Conference "Optical Fibres and their Application", Krasnobrod, Poland, 1999.

[Nod86] J. Noda, K. Okamoto, Y. Sasaki, Polarization-maintaining fibers and their applications, Journal of Lightwave Technology, LT-4, 8, 1071-1088, 1986.

[Oth99] A. Othonos, K. Kalli, Fiber Bragg gratings: Fundamentals and Applications in Telecommunications and Sensing, Artech House, 1999.

[Pra02] M. Prabhugoud, K. Peters, Measurement of local bending moment using optical fiber Bragg grating sensors, Conference of Smart Structures, San Diego, 2002.

[Sny79] A. W. Snyder, R. A. Sammut, Fundamental (HE) modes of graded optical fibers, Journal of Optical Society of America, Vol. 69, 1663-1671, 1979.

[Sny81a] A. W. Snyder, Understanding monomode optical fibers, Proceedings of IEEE, Vol. 69, 1, 6-13, 1981.

[Sny81b] A. W. Snyder, J. D. Love, Optical Wave theory, Chapmann and Hall, London, 1981.

[Tru99a] M. Trutzel, D. Betz, M. Holz, L. Staudigel, O. Krumpholz, H.-F. Siegling, R. Sangkohl, W. Martin, H.-C. Muehlmann, T. Müllert, H. Ahrendt, Strukturdiagnostik mit faseroptischen Bragg-Gitter-Sensoren, VDI Berichte 1463, 463-468, 1999.

[Tru00a] M. N. Trutzel, T. Kibler, D. Betz, K. Wauer, L. Staudigel, O. Krunpholz, H.-F. Siegling, R. Sangkohl, W. Martin, Sensorverhalten werkstoffintegrierter Bragg-Gitter-Sensoren, VDI Berichte 1530, 483-494, 2000.

[Ung80] H. Unger, Planar and fiber optical waveguides, Myr, 656, 1980.

[Yar84] A. Yariv, P. Yeh, Optical waves in crystals, John Wiley&Sons, New York, 1984.

[Yar89] A. Yariv, Quantum electronics, Wiley, New York, 1989.

To Chapter 4

[Ala93] A. T. Alavie, S. E. Karr, A. Othonos, R. M. Measures, A multiplexed Bragg grating fiber laser sensor system, IEEE Photonnics Technology Letters, Vol. 5, 9, 1112-1114, 1993.

[Ber88] A. Bertholds, R. Dandhiker, Determination of the strain-optic coefficients in single mode optical fibers, Journal of Lightwave Technology, Vol. 6, 1, 17-20, 1988.

[Ber00] J. W. Berthold, Measurement of Axial and Bending Strain in Pipelines Using Bragg Grating Sensors, Presented at the SPIE Environmental and Industrial Sensing Conference MTI 00-13, Boston, Massachusetts, October 9, 2000.

[Bra97] G. P. Brady, K. Kalli, D. J. Webb, D. A. Jackson, L. Reekie, J. L. Archambault, Simultaneous measurement of strain and temperature using the first- and second-order

diffraction wavelengths of Bragg gratings, IEE Proceedings-Optoelectronics, Vol. 144, 3, 156-161 1997.

[Bur00] J. G. Burnett, P. M. Blanchard, A. H. Greenway, Optical fibre-based vectoral shape sensor, Strain, Vol. 36, 3, 127-131, 2000.

[Corni02] Corning® SMF-28e™ Optical fibre, Product information, www.corning.com/opticalfiber, PI1344, Corning Inc., April 2002.

[Dav96] M. A. Davis, A. D. Kersey, Separating the temperature and strain effects on fiber Bragg grating sensors using stimulated Brillouin scattering, Proceedings of SPIE, Vol. 2718, 270-278, 1996.

[Dav97] M. A. Davis, A. D. Kersey, Simultaneous measurement of temperature and strain using fibre Bragg gratings and Brillouin scattering, IEE Proceedings-Optoelectronics, Vol. 144, 3, 151-155, 1997.

[Ebe92] K. J. Ebeling, Integrierte Optoelektronik, Springer Verlag, Berlin/Heidelberg/New York, 1992.

[Fal97] R. W. Fallon, L. Zhang, A. Gloag, I. Bennion, Identical broadband chirped grating interrogation technique for temperature and strain sensing, Electronic Letters, Vol. 33, 8, 705-707, 1997.

[Fer99] L. A. Ferreira, E. V. Diatzikis, J. L. Santos, F. Farahi, Demodulation of fiber Bragg grating sensors based on dynamic tuning of a multimode laser diode, Applied Optics, Vol. 38, 22, 4751-4759, 1999.

[Fer00] L. A. Ferreira, F. M. Araujo, J. L. Santos, F. Farahi, Simultaneous measurement of strain and temperature using interferometrically interrogated fiber Bragg grating sensors, Optical Engineering, 39, 8, 2226-2234, 2000.

[Fro48] M. Frocht, Photoelasticity, Vol. 2, Wiley, New York, 125-129, 1948.

[Gaf00] R. Gafsi, M. A. El-Schrif, Analysis of induced-birefringence effects on fiber Bragg gratings, Opt. Fib. Tech., Vol. 6, 299-323, 2000.

[Gon01] D. A. Gonzales, J. L. Arce-Diego, A. Cobo, J. M. Lopez-Higuera, Spectral modelling of curved long-period fibre gratings, Measurement Science and Technology, Vol. 12, 786-792, 2001.

[Gue02] J. A. Guemes, J. M. Menendez, Response of Bragg grating fiber-optic sensors when embedded in composite laminates, Composites Science and Technology, Vol. 62, 959-966, 2002.

[Hab00] W. R. Habel, Faseroptische Sensoren für hochaufgelöste Verformungsmessungen in der Zementsteinmatrix, Dissertation am FB 9 der TU Berlin, 2000.

[Han00] Y. Han, Ch. Kim, U. Paek, Performance enhancement of long period fiber gratings for strain and temperature sensing, IEICE Trans. Electron., E83-C 3, 282-286, 2000.

[Heg01] J. Hegger, M. Molter, D. Hofmann, F. Basedau, T. Gutmann, W. Habel, "Verbunduntersuchungen an textilbewehrten Betonkörpern mittels faseroptischer Mikrodehnungssensoren", VDI-Berichte, 1599, 165-170, 2001.

[Hoc79] G. B. Hocker, Fiber-optic sensing of pressure and temperature, Applied Optics, Vol. 18, 9, 1979.

[Hol89] H. Holbach, Faseroptische Temperaturmessung, Sensor Report 5, 1989.

[Kali97] G. Kalinka, A. Leistner, A. Hampe, Characterisation of the fibre/matrix interface in reinforced polymers by the push-in technique, Composites Science and Technology, Vol. 57, 845-851, 1997.

[Ker99] A. D. Kersey, H. J. Patrick, United States Patent # 5,945,666, August 31, 1999.

[Kim92] K. S. Kim, A model of embedded fiber optic Fabry-Pérot temperature and strain sensors, Ph. D. Dissertation, Stanford University, 1992.

[Kum84] A. Kumar, R. K. Varshney, Propagation characteristics of highly elliptical core optical waveguides: a perturbation approach, Opt. Quant. El., Vol. 16, 1984.

[Law95] C. M. Lawrence, D. V. Nelson, E. Udd, Measurement of transverse strains with fiber Bragg gratings, Proceedings of SPIE, Vol. 2444, p. 136-147, 1995.

[Lee00] B. H. Lee, Y. Chung, W.-T.-Han, U.-Ch. Paek, Temperature sensor based on self-interference of a single long-period fiber grating, IEICE Trans. Electron., E83-C, 287-292, 2000.

[Li01] X. Ch. Li, F. Prinz, J. Seim, Thermal behavior of metal embedded fiber Bragg grating sensor, Smart Materials and Structures, Vol. 10, 575-579, 2001.

[Liu00a] Y. Liu, Z. Guo, Y. Zhang, K. S. Chang, X. Dong, Simultaneous pressure and temperature measurement with polymer-coated fibre Bragg grating, Electronic Letters, Vol. 36, 6, 564-566, 2000.

[Lop02] J. M. Lopez-Higuera, Handbook of Optical Fibre Sensing Technology, John Wiley & Sons, 2002.

[Mac99] W. N. MacPherson, J. M. Kilpatrick, J. S. Barton, J. D. C. Jones, Heat-flux measurement using fibre-Bragg-grating Fabry-Perot sensors, Measurement Science and Technology, Vol. 10, 1300-1304, 1999.

[Marc91] D. Marcuse, Theory of dielectric optical waveguides, Academic press, New York, 1991.

[Mas97] S. Mastro, Fabry-Pérot, Bragg grating, and Optical MEMS Sensors for Naval Shipboard Use, Laser Diode and LED Application III, SPIE – The International Society for Optical Engineering, San Diego, 1997.

[Mizu01] T. Mizunami, H. Tatehata, H. Kawashima, High-sensitivity cryogenic fibre-Bragg-grating temperature sensors using Teflon substrates, Measurement Science and Technology, Vol. 12, 7, 914-917, 2001.

[Mors00] T. F. Morse, Y. He, F. Luo, An optical fiber sensor for the measurement of elevated temperatures, IEICE Trans. Electron., E83-C, 298-302, 2000.

[Nod86] J. Noda, K. Okamoto, Y. Sasaki, Polarization-maintaining fibers and their applications, Journal of Lightwave Technology, LT-4, 8, 1071-1088, 1986.

[Nog02] R. Nogueira, I. Abe, H. J. Kalinowski, J. F. da Rocha, J. L. Pinto, Precise Characterisation of fibre Bragg gratings for Photonic Communications systems, Proceedings of Photonics Prague '02, 101, 2002.

[Pra02] M. Prabhugoud, K. Peters, Measurement of local bending moment using optical fiber Bragg grating sensors, Conference of Smart Structures, San Diego, 2002.

[Peu99] J. Peupelmann, J. Meißner, Fibre Bragg Grating Sensors, Proceedings II of Conference on Sensors Transducers & Systems 99, P1.21, 357-362, 1999.

[Rao02] Y. J. Rao, S. F. Yuan, X. K. Zeng, D. K. Lian, Y. Zhu, Y. P. Wang, S. L. Huang, T. Y. Liu, G. F. Fernando, L. Zhang, I. Bennion, Simultaneous strain and temperature measurement of advanced 3-D braided composite materials using an improved EFPI/FBG system, Optics and Lasers in Engineering, in press, 2002.

[Rei98] M. Reid, *et al.* Temperature dependence of fiber optic Bragg gratings at low temperature, Optical Engineering, Vol. 37, 1, 237, 1998.

[San01] S. Sandlin, T. Kinnunen, J. Rämö, Metal embedding of optical fibres for condition monitoring, Baltica V Conference, June 2001.

[San02] S. Sandlin, L. Heikinheimo, Evaluation of a new method for metal embedding of optical fibres for high temperature sensing purposes, Seminar of the Academy of Finland, Tampere University of Technology, 03.01.2002.

[Sny81b] A. W. Snyder, J. D. Love, Optical Wave theory, Chapmann and Hall, London, 1981.

[Stee95] R. J. Van Steekiste, Theory of Fiber optic Strain and temperature sensors, Ph.D. Dissertation, Stanford University, 1995.

[Sun99] T. Sun, Z. Y. Zhang, K. T. V. Grattan, A. W. Palmer, Intrinsic doped fibre fluorescence-lifetime based high temperature alarm sensor, Sensors and Actuators, Vol. 76, 67-71, 1999.

[Teu00] J. Teunissen, Ch. Helmig, D. Peier, Möglichkeit des Einsatzes faseroptischer Bragg-Gitter zur On-Line-Temperaturmessung, VDI Berichte 1530, 2000.

[Tor02] P. Torres, L. C. G. Valente, Spectral response of pressed fiber Bragg grating, Optical Communications, in press, 2002.

[Tru98] M. Trutzel, H.-F. Siegling, D. Betz, R. Sangkohl, M. Holz, L. Staudigel, W. Martin, O. Krumpholz, Neue Sensorkonzepte für den Adaptiven Flügel, Deutscher Luft- und Raumfahrt Kongress; Bremen; 6.-8. Oktober 1998.

[Tru99a] M. Trutzel, D. Betz, M. Holz, L. Staudigel, O. Krumpholz, H.-F. Siegling, R. Sangkohl, W. Martin, H.-C. Muehlmann, T. Müllert, H. Ahrendt, Strukturdiagnostik mit faseroptischen Bragg-Gitter-Sensoren, VDI Berichte 1463, 463-468, 1999.

[Tru99b] M. Trutzel, O. Krumpholz, Ch. Boller, Anwendungspotential faseroptischer Sensoren in Luft & Raumfahrt und Fahrzeugbau, Jena Workshop „Faseroptische Sensortechnik", Oktober 1999.

[Tru00b] M. Trutzel, D. Betz, M. Holz, L. Staudigel, O. Krumpholz, H.-F. Siegling, R. Sangkohl, W. Martin, H.-C. Mühlmann, T. Müllert, H. Ahrendt, Investigation of fiberoptic Bragg grating sensors for applications in the aviation industry, F2-6, OFS-13, 624-627, 2000.

[Tru01] M. N. Trutzel, Dehnungsermittlung mit faseroptischen Bragg-Gitter-Sensoren: Grundlagen, Eigenschaften und Anwendungen, Doktorarbeit, Berlin, 2001.

[Tsa92] C. Tsao, Optical fibre waveguide analyse, Oxford, New York, 1992.

[Wad01] S. A. Wade, D. I. Forsyth, K. T. V. Grattan, Q. Guofu, Fiber optic sensor for dual measurement of temperature and strain using a combined fluorescence lifetime decay and fiber Bragg grating technique, Review of scientific instruments, Vol. 72, 8, 3186-3190, 2001.

[Wag96] R. B. Wagreich, W. A. Atia, H. Singh, J. S. Sirkis, Effects of diametric load on fiber Bragg gratings fabricated in low birefringent fiber, Electronic Letters, Vol. 26, 6, 1223-1224, 1996.

[Wilk99] V. Wilkend, C. Wiemann, Ch. Koch, H.-J. Foth, Fiber-optic dielectric multilayer temperature sensor: in situ measurement in vitreous during Er:YAG laserr irradiation, Optics&Laser Technology, Vol. 31, 593-599, 1999.

[Wu00] J. Wu, Sh. Tsao, United States Patent # 6,024,488, February 15, 2000.

To Chapter 5

[Bob97a] Ya. V. Bobitski, V. M. Fitio, S. Y. Zakalyk, Model of light propagation in fibreoptic Bragg grating, 4th Internernational Conference L'viv, Vol. 2, 19-21, 1997.

[Bob98a] Y. Bobitski, W. Fitio, S. Lebid, T. V. Fityo, Propagation of optical waves in quasiperiodical medium, International Conference "Modern Problems of Telecommunications, Computer Science and Engineers Training" (TCSET'98), L'viv, 163-165, 1998.

[Bob00] Y. V. Bobitski, V. M. Fitio, S. Y. Lebid, T. V. Fityo, Reflection spectrum of quasiperiodical dielectric structure, Journal of Applied Spectroscopy, Vol. 67, 5, 650-653, 2000.

[Cok57] E. G. Coker, L. N. G. Filon, H. T. Jessop, A treatise of Photo-elasticity, The University Press Cambridge, 1957.

[Erd97] T. Erdogan, Fiber grating spectra, Journal of Lightwave Technology, Vol. 15, 8, 1277-1294, 1997.

[Gaf00] R. Gafsi, M. A. El-Schrif, Analysis of induced-birefringence effects on fiber Bragg gratings, Opt. Fib. Tech., Vol. 6, 299-323, 2000.

[Gon01] D. A. Gonzales, J. L. Arce-Diego, A. Cobo, J. M. Lopez-Higuera, Spectral modelling of curved long-period fibre gratings, Measurement Science and Technology, Vol. 12, 786-792, 2001.

[Hab00] W. R. Habel, Faseroptische Sensoren für hochaufgelöste Verformungsmessungen in der Zementsteinmatrix, Dissertation am FB 9 der TU Berlin, 2000.

[Hil97] K. O. Hill, G. Meltz, Fiber Bragg grating technology fundamentals and overview, Journal of Lightwave Technology, Vol. 15, 8, 1263-1276, 1997.

[Kas99] R. Kashiap, Fibre Bragg Gratings, Academic Press, 1999.

[Lebi98] S. Y. Lebid, Y. W. Bobitski, W. M. Fitio, T. W. Fityo, Spectrum of Bragg grating reflection coefficient (RC) in optical fiber, Symposium Photonics West, OPTOELECTRONICS 1998.

[Lop02] J. M. Lopez-Higuera, Handbook of Optical Fibre Sensing Technology, John Wiley & Sons, 2002.

[Mag97] S. Magne *et al.*, State-of-strain evaluation with fiber Bragg grating rosettes: application to discrimination between strain and temperature effects in fiber sensors, Applied Optics, Vol. 36, 36, 1997.

[Oth99] A. Othonos, K. Kalli, Fiber Bragg gratings: Fundamentals and Applications in Telecommunications and Sensing, Artech House, 1999.

[Rao02] Y. J. Rao, S. F. Yuan, X. K. Zeng, D. K. Lian, Y. Zhu, Y. P. Wang, S. L. Huang, T. Y. Liu, G. F. Fernando, L. Zhang, I. Bennion, Simultaneous strain and temperature measurement of advanced 3-D braided composite materials using an improved EFPI/FBG system, Optics and Lasers in Engineering, in press, 2002.

[Rei98] M. Reid, *et al.* Temperature dependence of fiber optic Bragg gratings at low temperature, Optical Engineering, Vol. 37, 1, 237, 1998.

[Tru01] M. N. Trutzel, Dehnungsermittlung mit faseroptischen Bragg-Gitter-Sensoren: Grundlagen, Eigenschaften und Anwendungen, Doktorarbeit, Berlin, 2001.

To Chapter 7

[Dra02] N. M. Dragomir, D. Garchev, G. W. Baxter, P. M. Farrel, A. Roberts, Non-destructive imaging and characterisation of optical fiber Bragg gratings, Proceedings of Photonics Prague '02, 35, 2002.

[Hab00] W. R. Habel, Faseroptische Sensoren für hochaufgelöste Verformungsmessungen in der Zementsteinmatrix, Dissertation am FB 9 der TU Berlin, 2000.

[Lebi99] S. Lebid, W. Fitio, Ya. Bobitski, Analysis of light propagation in fiber cladding gratings, Proceedings of SPIE, vol. 3801, 147-155, 1999.

[San02] S. Sandlin, L. Heikinheimo, Evaluation of a new method for metal embedding of optical fibres for high temperature sensing purposes, Seminar of the Academy of Finland, Tampere University of Technology, 03.01.2002.

[Tru01] M. N. Trutzel, Dehnungsermittlung mit faseroptischen Bragg-Gitter-Sensoren: Grundlagen, Eigenschaften und Anwendungen, Doktorarbeit, Berlin, 2001.

To Attachment A

[Hon74] A. Hondros, P. Debye, Electromagnetic waves in dielectric wires, Ann. Phys., Vol. 32, 465-476, 1974.

[Sny79] A. W. Snyder, R. A. Sammut, Fundamental (HE) modes of graded optical fibers, Journal of Optical Society of America, Vol. 69, 1663-1671, 1979.

[Sny81b] A. W. Snyder, J. D. Love, Optical Wave theory, Chapmann and Hall, London, 1981.

To Attachment B

[Yar84] A. Yariv, P. Yeh, Optical waves in crystals, John Wiley&Sons, New York, 1984.

To Attachment C

[Mart99] T. Martynkien, W. Urbanczyk, W. Bock, T. Smolnicki, Modelowanie spektralnych wlasciwosci swiatlowodow z eliptycznym rdzeniem, Proceedings of VII Conference "Optical Fibres and their Application", Krasnobrod, Poland, 1999.

[Nod86] J. Noda, K. Okamoto, Y. Sasaki, Polarization-maintaining fibers and their applications, Journal of Lightwave Technology, LT-4, 8, 1071-1088, 1986.

To Attachment E

[Bob97b] Y. Bobitski, W. Fitio, S. Lebid, T. Wanchytski, Reflection spectrum calculation in optical fiber periodical structures (PS), Proc. 3rd International Conf. MECHATRONIKA'97, Warszawa (Poland), 775-781, 1997.